A **Searches**

by

James Beacham

A dissertation submitted in partial fulfillment
of the requirements for the degree of
Doctor of Philosophy
Department of Physics
New York University
May 2014

Professor Kyle Cranmer

Dedication

To my mom.

Acknowledgements

Thanks are due to the entirety of the New York University Physics Department, particularly the Experimental Particle Physics group (faculty, post-doctoral researchers, and students) for their support. Moreover, constant assistance and unyieldingly stimulating conversation and instruction has been provided by the researchers in the NYU Center for Cosmology and Particle Physics, without whom this work would not have been possible. Additionally, this research draws upon the wisdom, expertise, skill, talent, and hard work of hundreds (and in some cases thousands) of members of the ATLAS, APEX and ALEPH experiments, as well as the technical and engineering staff at the LHC, Jefferson Lab and LEP, whose efforts are gratefully acknowledged. In particular, this work has benefited from the cooperation, help, and advice of the smaller number of ATLAS, APEX, and ALEPH members with whom personal collaboration has been performed. Finally, I thank my advisor, Kyle Cranmer, for consistently placing difficult challenges in my path.

Abstract

The Standard Model of particle physics encompasses three of the four known fundamental forces of nature, and has remarkably withstood all of the experimental tests of its predictions, a fact solidified by the discovery, in 2012, of the Higgs boson. However, it cannot be the complete picture. Many measurements have been made that hint at physics beyond the Standard Model, and the main task of the high-energy experimental physics community is to conduct searches for new physics in as many different places and regimes as possible. I present three searches for new phenomena in three different high-energy collider experiments, namely, a search for events with at least three photons in the final state, which is sensitive to an exotic decay of a Higgs boson into four photons via intermediate pseudoscalar particles, a, with ATLAS, at the Large Hadron Collider; a search for a dark photon, also known as an A', with APEX, at Thomas Jefferson National Accelerator Facility; and a search for a Higgs decaying into four tau leptons via pseudoscalar a particles, with ALEPH, at the Large Electron-Positron collider.

Contents

List of Figures

List of Tables

Introduction

The Standard Model (SM) of particle physics [1, 2, 3] is one of the most successful intellectual achievements of humankind. Starting from basic mathematical frameworks, namely a combination of quantum field theory and group theory, one can make definite and clear predictions as to what one should see in a wide range of high energy collider experiments. Throughout the 20th century, over the course of the development of the SM, the interplay between theory and experiment resulted in predictions being made and experiments being carried out, and the results validated the theory to an impressive degree. At the energy scales accessible to the past and current collider community, the ideas that nature at the fundamental particle level is described by a gauge field theory involving the gauge group $SU(3)_C \times SU(2)_L \times U(1)_Y$ and that the rates at which particles will be produced in collider experiments (and their properties) can be determined via the mathematical tools provided by quantum field theory, is now established to a high degree of certainty. The theory of the strong force, quantum chromodynamics, including the physical reality of quarks, gluons, and their interactions, was predicted and verified experimentally. The massive W boson was discovered and soon identified as a key component of the electroweak theory, and the discovery of the Z boson, and its role in the theory, was made soon thereafter. And a scalar boson that very much resembles the final remaining piece of the SM puzzle, the Higgs boson, the particle manifestation of the scalar field responsible for electroweak symmetry breaking, was discovered in 2012 by the ATLAS and CMS collaborations [4, 5]. The validity of the SM is well established.

However, the SM cannot be the complete picture of nature at all fundamental scales. One reason is that it does not include gravity, which is known to exist.

Furthermore, it cannot explain the strong CP problem, i.e., the fact that, although there are terms in the QCD Lagrangian that naturally violate CP, this violation is not observed in experiments that probe the QCD sector. Yet another reason is that the measured value of the magnetic moment of the muon differs significantly (corresponding to a deviation of more than 3σ) from the SM prediction. And yet another is the existence of dark matter, which is established by astrophysical observations. Many experiments are currently being performed to try and uncover the sources of these discrepancies, and a good explanation of them would either require a clever augmentation of the SM, or a wholly different theory.

In the SM, the gauge groups correspond to different fundamental forces of nature, each of which is manifest at the particle level as a gauge boson, or force-carrying particle (or class of particles). For the strong force, the gauge bosons are gluons. For the weak force, the gauge bosons are the $W^{\pm}$ and Z bosons. And for electromagnetism, the gauge boson is the photon. One way that the SM could be augmented to accommodate the discrepancies mentioned above is if the $SU(3)_C \times SU(2)_L \times U(1)_Y$ gauge group mentioned above were only part of the story, i.e., if there were other gauge groups that, when combined with the SM gauge group, formed a larger gauge group that is broken down to the SM, leading to the particle content we observe. An experimental consequence of this is that the positing of gauge field extensions implies more gauge bosons to be discovered at collider experiments. Two plausible SM extensions that could result in new gauge bosons within the grasp of current experiments are highlighted hereafter.

In the SM, the process by which the electroweak force is broken into electromagnetism and the weak force, giving rise to the massive and massless physical gauge bosons we observe, is called electroweak symmetry breaking. It is accomplished via the Brout-Englert-Higgs mechanism [6, 7, 8, 9, 10, 11], which results in the physical mass states of the massless photon (the gauge boson of electromagnetism) and the massive $W^{\pm}$ and Z bosons (the gauge bosons of the weak force), in addition to one massive scalar, the Higgs boson. This particular combination of massive weak gauge and Higgs bosons, and the massless photon, is a consequence of the way the gauge fields combine with the scalar Higgs doublet. Before electroweak symmetry breaking, the electroweak part of the SM gauge group is made up of a single complex $SU(2)_L$ scalar doublet, with four degrees of freedom, an $SU(2)_L$ gauge field with three gauge bosons, each with two degrees of freedom, and the $U(1)_Y$ weak hypercharge gauge field, with two degrees of freedom. After electroweak symmetry breaking, there are three massive vector gauge bosons for the weak force, the $W^{\pm}$ and Z bosons, each with three degrees of freedom, a massless photon, with two degrees of freedom, leaving one degree of freedom left, for the massive scalar Higgs boson. Thus, the Higgs sector contains four degrees of freedom, three of which are used to give masses to the physical $W^{\pm}$ and Z bosons, and the fourth of which results in the massive Higgs boson, h.

The simplest extension to the SM is the addition of a singlet field that results in an extra pseudoscalar particle, a, that couples to the Higgs. Such an addition is well motivated and well studied in many models involving simple singlet fields (e.g., Ref. [12]) or singlet fields as a part of supersymmetric theories (e.g., [13, 14, 15]). Supersymmetric models such as the minimal supersymmetric SM (MSSM) also often add one doublet, which is the next simplest extension of the Higgs sector, and which would leave five extra degrees of freedom and, hence, five scalar particles, rather than the one of the SM. Of these five, one would be the SM Higgs (h), two are charged under electromagnetism ($H^{\pm}$), one is an additional CP-even scalar

(H) with higher or lower mass than the $m_h = 125$ GeV/c^2 of the SM Higgs, and the last would be a CP-odd scalar, i.e., a pseudoscalar (A). Moreover, the next-to-MSSM (NMSSM) contains an additional singlet field, which gives rise to another, typically low-mass, pseudoscalar (a). This is the basic idea behind two Higgs doublet models, which are well studied (e.g., [16]). Both of these extensions have, as a consequence, new scalar or pseudoscalar particles that can either be produced directly in existing collider experiments (or those of the recent past) or can couple to other scalars, including the scalar boson that resembles the SM Higgs particle that has been discovered at the LHC. This coupling (or mixing with other scalars or pseudoscalars) can result in Higgs-related final states that could be discovered at ATLAS and CMS. In the context of the newly discovered scalar that resembles the SM Higgs, the observation of an excess in a two-object final state that is part of a cascade decay of the SM Higgs into four SM particles via an intermediate pseudoscalar (i.e., a decay of the form $h \to aa \to 2X2Y$, where a is the pseudoscalar, and X and Y are final state particles) would be the first hint at fundamental physics beyond the SM at collider experiments. And, as mentioned above, the identification of a new gauge boson could mean the discovery of another fundamental force of nature previously undetected. Such an identification involves searching for novel signatures at ATLAS and CMS that are uncovered by current or previous analyses.

Another way that a new force of nature could have gone undetected is if the force-carrying particle (gauge boson) were a vector (i.e., with spin = 1), with a mass below ~ 1 GeV/c^2, and were very weakly coupled to the SM photon via kinetic mixing, through quantum loops of SM particles. Such a new vector gauge boson is well motivated and studied (e.g., [17, 18, 19]), and is often referred to as a U-boson, hidden photon, dark photon, or A'. The existence of such an A', with $m_{A'} < 1$ GeV/c^2 and with fractional electromagnetic charge of $\epsilon < 10^{-2}$, could possibly explain observed dark matter anomalies, as well as the observed, discrepant value of the magnetic moment of of the muon. (See Ref. [20] for a complete discussion.) But more generally, it would represent the first detection of a new fundamental force of nature beyond those of the SM and gravity, and would radically alter the theoretical and experimental landscape for generations to come.

The most intriguing aspect of such a low-mass vector gauge boson is that it can be searched for at existing medium-energy ($1 < E_{beam} < 12$ GeV) fixed-target electron beam facilities — such as the Thomas Jefferson National Accelerator Facility (JLab), in Virginia, and the Mainz Microtron, in Mainz, Germany — that have been designed primarily for hadronic spectroscopy and for precision measurements of strong force dynamics. Such searches require high mass resolution and large datasets, both of which can be readily achieved at current facilities.

This document is organized as follows. Chapter 1 presents a search for new phenomena in events with at least three photons in the final state using data collected by the ATLAS detector in 2012 at a center-of-mass energy of $\sqrt{s} = 8$ TeV. Such a search could possibly discover a new pseudoscalar, a, similar to the one described above, that would result from the decay of the SM Higgs boson, h, and that would subsequently decay into four photons. Chapter 2 describes APEX, the A Prime EXperiment, which is a fixed target experiment at JLab that searches for an A', as mentioned above, and for which a test run was held in 2010. Finally, Chapter 3 details an analysis of data collected by the ALEPH detector at the Large Electron-Positron (LEP) collider which would be sensitive to the decay of a SM Higgs into four tau leptons via intermediate pseudoscalars, a.

Chapter 1

A search for new phenomena with at least three photons in the final state, with ATLAS

1.1 Introduction and Motivation

Many extensions of the Standard Model (SM) include phenomena that can result in final states consisting of three (or more) photons ("multi-photon final states") in proton-proton collisions. Extensions of the Higgs sector [21, 12, 16], for example, often include CP-odd particles (a) with couplings to the Higgs and branching ratios into photons that would be visible at the LHC. Other models [22] feature additional vector gauge bosons that can decay to a photon + a, with the subsequent decay of the a into a pair of photons, resulting in a three photon final state. Moreover, non-minimal extensions of the SM gauge group [23] can include stable dark matter candidates that are charged under a hidden SU(N) symmetry, resulting in couplings of dark matter to an exotic scalar, S. These scalars can have couplings to SM Z bosons and photons, and can be produced in pairs in Z boson and off-shell photon decays. The resulting "S-hadrons" can decay into photon pairs, resulting in four photon final states.

Moreover, in the SM, the Z boson can decay to three photons via a loop of $\mathrm{W}^{+/-}$ bosons or fermions. The decay is heavily suppressed and the branching ratio is predicted to be $\sim 5 \times 10^{-10}$ [24]. The current strongest bounds on this process come from the L3 Collaboration, which placed a limit of $BR(Z \rightarrow 3\gamma) < 10^{-5}$ [25]. The ATLAS detector has collected $\sim 10^9$ Z events, and thus has the possibility of either observing this decay or placing the strongest current bounds on this process. An enhancement of this decay rate could be evidence of phenomena not predicted by the SM.

Feynman diagrams for some of these beyond-the-Standard Model (BSM) and rare SM scenarios are shown in Figure 1.1.

To ensure sensitivity to these and other possible rare SM and BSM scenarios, an inclusive three-photon search is performed using 20.3 fb^{-1} of LHC proton-proton collisions collected by the ATLAS detector in 2012 at a centre-of-mass energy of 8 TeV.

The dominant irreducible backgrounds arise 1) from the prompt production of two photons where a third photon arises from the underlying event and 2) when a quark exchanged in the hard process radiates three or four prompt, energetic photons. The dominant reducible backgrounds come from processes involving real photons + QCD jets, where the jets are misidentified as photons, and Z bosons decaying to electrons which are misidentified as photons. A small contribution comes from W boson decays to lepton+neutrino in association with a hard-process

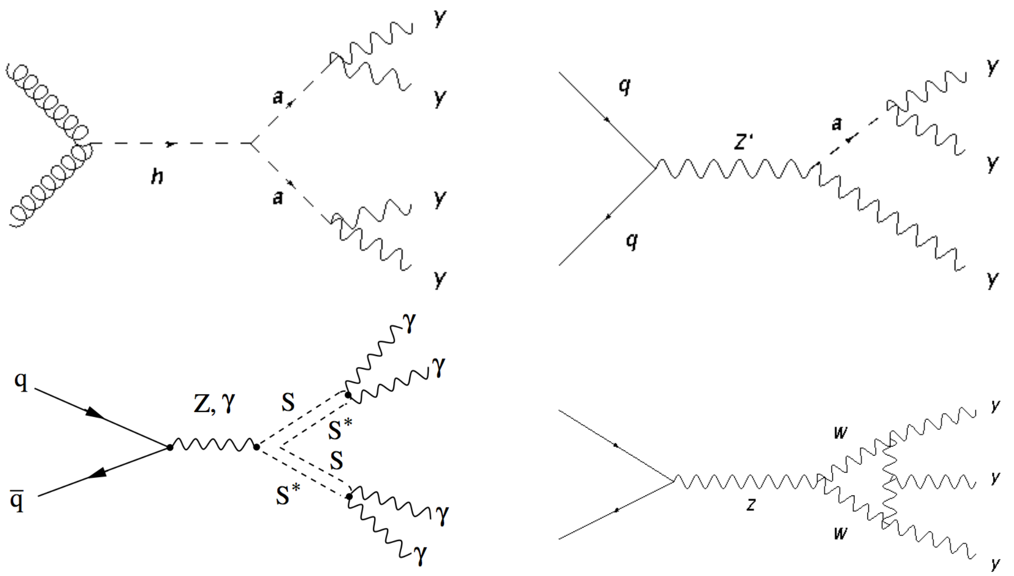

Figure 1.1: Feynman diagrams for possible beyond-the-Standard Model and rare Standard Model scenarios that result in multi-photon final states.

photon and jets.

In this analysis the expected yields from irreducible SM photon processes and the electron backgrounds are estimated with Monte Carlo (MC) simulations. The possible mis-measurement of the rate of electrons faking photons in simulated samples is addressed by selecting events in data and MC that have a high probability of arising from Z boson decays and comparing the distributions. The electron MC is then scaled to match data.

The contributions from jet backgrounds are estimated using a method that employs photon isolation efficiencies and jet fake rates calculated from collision data. Evidence of new phenomena would appear as an excess in the signal region, defined as the set of events with three tightly identified photon candidates which pass a criterion on the amount of transverse energy in a cone around the center of the energy deposit in the electromagnetic calorimeter ("isolated") and with transverse momenta (p_T) above a threshold, and that appear in the fiducial detector volume. Control regions are then defined as sets of events where at least one of the photon candidates fails either isolation or tight ID, or both. A full description of the object and event selection appears in Section 1.4.

A key component of the analysis is the data-driven estimate of the jet backgrounds, in which the standard tight (T) and loose (L) photon identification categories are augmented with a loose-prime (L′) definition intermediate between T and L, that relaxes some requirements on some discriminating variables based upon energy deposits in the electromagnetic calorimeter and, when combined with the requirement that the photon candidate also fail T, provides a sample of photon candidates that is primarily composed of jets faking photons. Photon isolation efficiencies and jet fake rates are calculated for three regions in the $p_T - \eta$ plane, and these values are used as an input to a likelihood matrix method. The output of the method is the expected contributions from final states consisting of jets plus photons or solely jets in signal and control regions. The method, and its validations on MC samples, is described in Section 1.5.3.2.

1.2 The ATLAS Detector

ATLAS (A Toroidal LHC ApparatuS) is one of the two general purpose detectors at the Large Hadron Collider (LHC) that have been built for analyzing proton-proton or heavy ion collisions. It has been designed to ensure sensitivity to a wide variety of signatures of possible new physics accessible at the high energies and luminosities achievable at the LHC, which are the highest ever used by mankind in an accelerator experiment. These high energies and luminosities result in interaction rates, radiation levels, and particle multiplicities not encountered

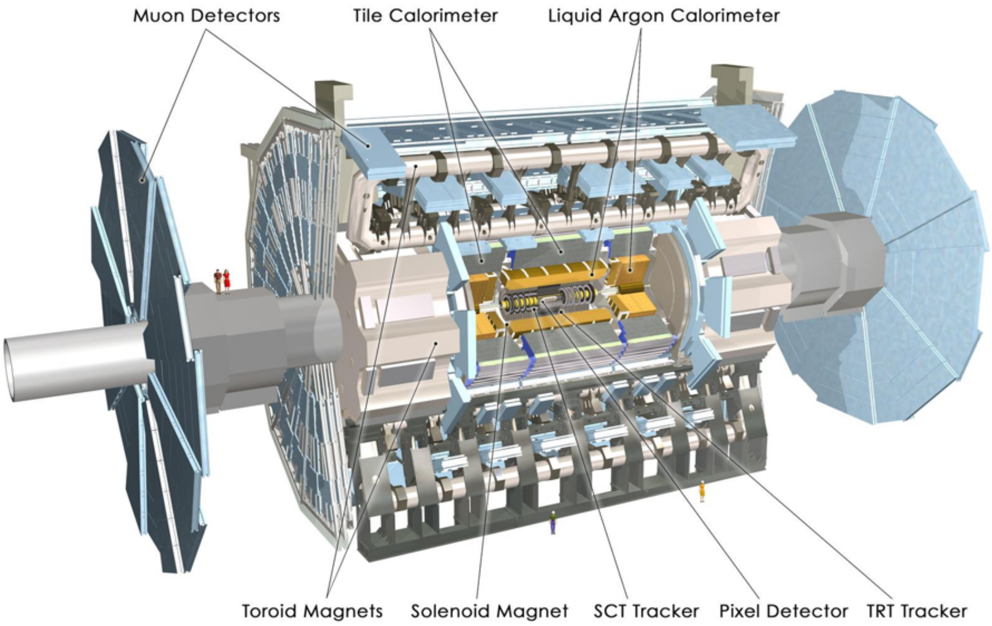

Figure 1.2: The ATLAS Detector and its subsystems.

at previous experiments, and the levels of precision needed to be sensitive to new phenomena under such difficult conditions has led to the construction of one of the most technologically advanced experimental devices ever built. The detector is the result of the work of thousands of physicists, engineers and technicians conducted over a period of fifteen to twenty years, and is described in detail elsewhere [26]. Given here is an overview of the detector, followed by a brief discussion of the electromagnetic calorimeter, which is the most important ATLAS sub-system for the multi-photon analysis.

1.2.1 Overview

The ATLAS detector [26](shown in Fig. 1.2) consists of an inner detector immersed in a 2T solenoidal magnetic field, as well as electromagnetic and hadronic calorimeters and a muon spectrometer that uses toroidal magnets. The inner detector measures tracks of charged particles over the full azimuthal angle ϕ and in a pseudorapidity range of $|\eta| < 2.5$ [1] using silicon pixel, silicon microstrip, and transition-radiation straw-tube detectors. The transition-radition detectors also distinguish electrons from more massive charged particles in the range $|\eta| < 2.0$. Liquid-argon (LAr) electromagnetic sampling calorimeters provide coverage in the range $|\eta| < 3.2$ with high granularity (see the next section). For hadronic calorimetry, steel and scintillator tiles provide coverage for $|\eta| < 1.7$, and in the endcaps ($|\eta| > 1.5$), LAr is also used to provide for hadronic calorimetry, matching the outer $|\eta|$ limit of the endcap electromagnetic calorimeters. The LAr forward calorimeters extend both electromagnetic and hadronic calorimetry coverage to $|\eta| < 4.9$. The region between the barrel and endcap EM calorimeters, $1.37 < |\eta < 1.52$, due to the presence of cables and other matter in front of measurement instruments, is expected to have poorer performance, and electromagnetic objects in this region are often excluded from analyses. The calorimeters are surrounded by the muon spectrometer, which covers $|\eta| < 2.7$. Excellent muon momentum resolution is achieved with three layers of high precision tracking chambers. Triggering is provided by a three-level system and is used to quickly select and record potentially interesting events to be analyzed offline.

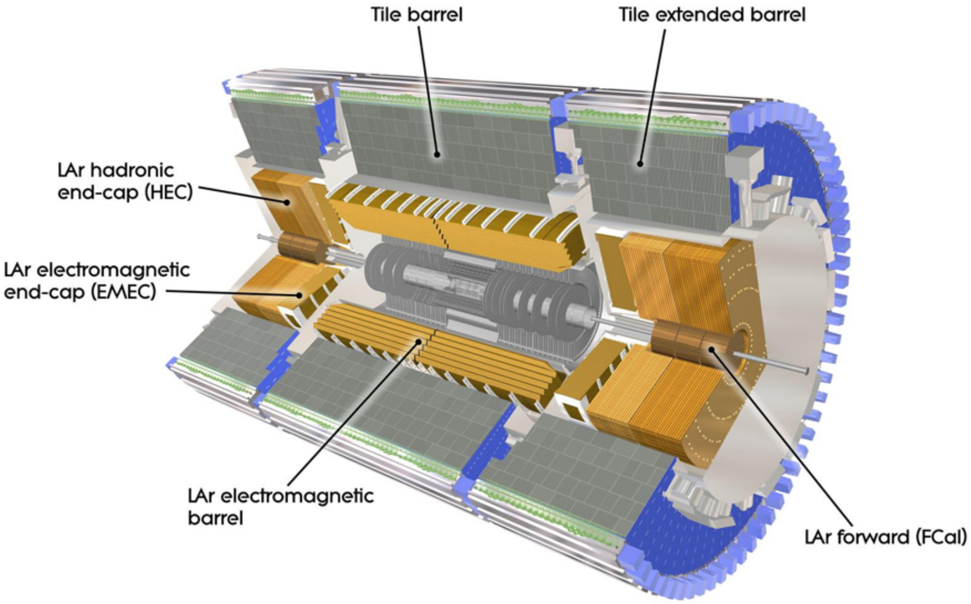

Figure 1.3: The ATLAS calorimetry system.

1.2.2 Electromagnetic calorimeter

The ATLAS electromagnetic calorimeter (EMC, shown in Fig. 1.3) has been designed to provide high levels of discrimination between electrons and photons, between pion decays and photons, and between unconverted photons and photons that have decayed into an electron-positron pair. To accomplish this, a unique accordian-like geometry has been utilized, and three-layer calorimeter system employed, with very high-granularity in the first layer. Photons are identified and reconstructed as isolated energy deposits in the EMC, with little energy deposi-

---

[1] ATLAS uses a right-handed coordinate system with the z-axis defined along the beam pipe entering the detector from either side, and with an origin defined at the nominal interaction point in the center of the detector. The x-axis points from the detector center to the center of the LHC ring, and the y-axis points upward, away from the center of the earth. A cylindrical coordinate system is defined using radial and azimuthal angle (around the beam pipe) directions, (r, ϕ), in the plane transverse to the z-axis. The polar angle θ defines the pseudorapidity as $\eta = -\ln\tan(\theta/2)$.

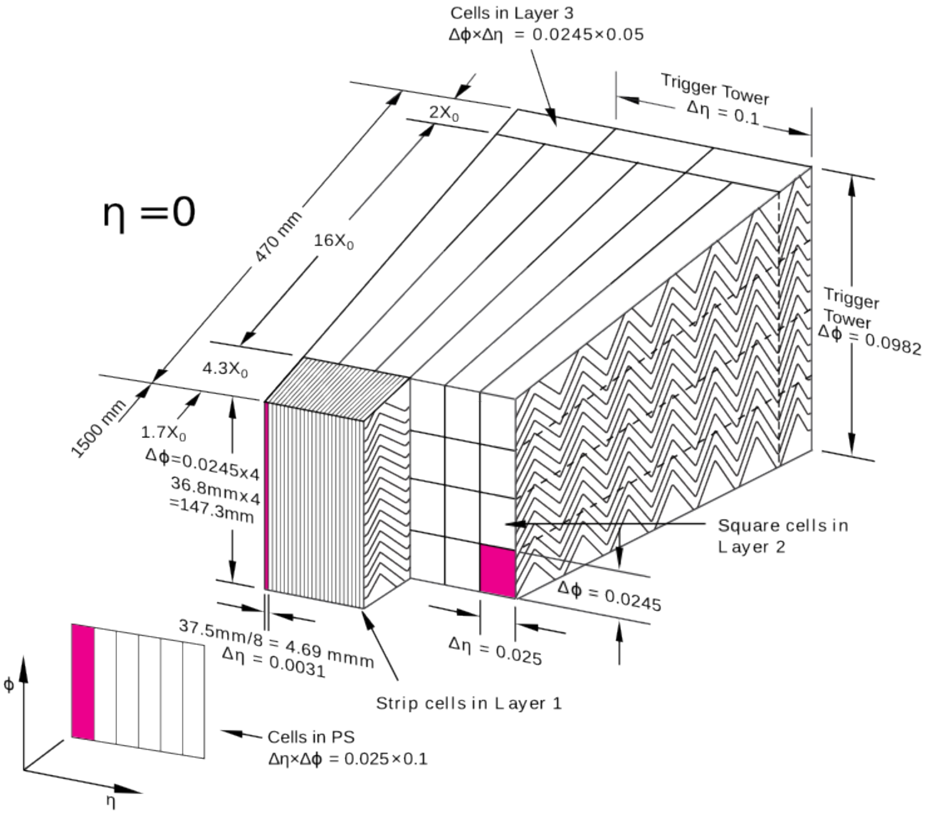

Figure 1.4: Diagram displaying the granularity in η and ϕ in the layers in the electromagnetic calorimeter.

tion in the hadronic calorimeter, which surrounds the EMC. The reconstruction procedure and the method of ambiguity resolution between converted photons and electrons are described in Ref [27]. Sampling is provided by layers of lead/stainless steel and liquid argon. The unique accordion geometry allows for fast, accurate charge collection and readout and minimizes dead space in the detector active volume; see Fig. 1.4. The EMC is composed of a barrel section, covering the pseudorapidity region $|\eta| < 1.475$, and two end-cap sections, covering the region $1.375 < |\eta| < 3.2$. It consists of three layers, described here moving outward from the nominal interaction point:

- The first layer, with a thickness between 3 and 5 radiation lengths, is segmented into high granularity strips in the η direction (width between 0.003 and 0.006 depending on η, with the exception of the regions $1.4 < |\eta| < 1.5$ and $|\eta| > 2.4$). As mentioned, the ability to distinguish between prompt photons and a pair of highly collimated photons arising from the decay of a π^0 is crucial. This is accomplished by the high granularity of the first layer: Photons from π^0 decays often produce a cluster in the EMC that contains two cells with two energy maxima, and the fine granularity of the first layer provides the ability to identify and distinguish between the two objects.

- The second layer has a thickness of around 16 radiation lengths and a granularity of 0.025×0.025 in $\eta \times \phi$ (corresponding to one cell). The second layer collects most of the energy deposited by the photon candidate, and also provides the ability to measure the pseudorapidity values, η, of photons by using the energy-weighted barycenter of the cluster therein.

- A third layer, with thickness varying between 4 and 15 radiation lengths, collects the tail of the electromagnetic shower and is used to correct shower leakage beyond the calorimeter for deposits of high energy.

The dominant background to the multi-photon search is the production of jets which fake photons in the electromagnetic calorimeter. Using combinations of different shower shape variables that exploit the high granularity and segmentation of the electromagnetic calorimeter, looser or tighter photon identification criteria are defined which allow one to design a method to estimate the rate of jets faking photons that relies on collision data. These methods are described in detail below.

1.3 Event samples

This section details the data and MC samples used for the analysis. All samples used are either preexisting official ATLAS simulated samples, or have been studied with MC generators privately before being requested to be produced and fully simulated through the ATLAS detector by central MC production.

1.3.1 Data and luminosity

This search utilizes LHC pp collisions collected by the ATLAS detector during 2012 at a center-of-mass energy of 8 TeV, corresponding to an integrated luminosity of 20.3 fb^{-1}. The total luminosity delivered by the LHC and collected by ATLAS in 2012 is shown in Figure 1.5. The analysis is restricted to those events passing an event-level three-photon trigger, hereafter referred to as `EF_3g15vh_loose`.

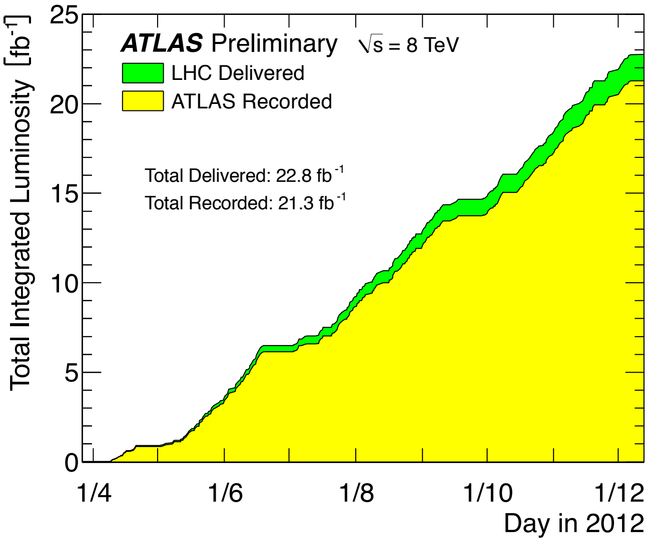

Figure 1.5: Total luminosity delivered by the LHC and collected by ATLAS during data-taking periods in 2012.

1.3.2 Monte Carlo samples

The backgrounds from events with three or four hard process photons and electrons from Z decays are estimated with MC samples. The ATLAS detector is simulated using GEANT 4 [28], and simulated events are reconstructed using the same software as that used for collision data.

The irreducible SM three or four photon backgrounds are modeled with MADGRAPH 5.1.4.4 [29] and PYTHIA 8.163 [30], and two-photon processes are modeled with PYTHIA 8. Processes where a Z boson decays to an e^+e^- pair, accompanied by a photon not from the matrix element, are modeled with POWHEG-BOX 1.0 [31]+PYTHIA 8, and Z+γ production is modeled with SHERPA 1.4.1 [32]. Processes where a W boson decays to a lepton plus a neutrino in association with a hard-process photon and from 0 up to 2 jets are simulated with ALPGEN [33]+HERWIG [34, 35].

Process	Generator	PDF set
2γ	Pythia 8	CTEQ6L1
3γ	MadGraph 5	CTEQ6L1
4γ	MadGraph 5	CTEQ6L1
Zee	Powheg+Pythia 8	CTEQ6M
Z+γ	Sherpa	CT10
W+γ+Np0	Alpgen+Herwig	CTEQ6L1
W+γ+Np1	Alpgen+Herwig	CTEQ6L1
W+γ+Np2	Alpgen+Herwig	CTEQ6L1

Table 1.1: Monte Carlo background samples used and parameters, one of two.

Process	σ [pb]	Filter eff.	N_{gen}	K-factor
2γ	1.3809×10^{-1}	6.4801×10^{-4}	999898	1.0
3γ	7.1164×10^{-8}	1.0	100000	1.0
4γ	1.2509×10^{-10}	1.0	100000	1.0
Zee	1.1099×10^{-3}	1.0	9894581	1.0
Z+γ	3.2298×10^{-5}	1.0	3189892	1.0
W+γ+Np0	2.2988×10^{-4}	0.31372	14296258	1.15
W+γ+Np1	5.9519×10^{-5}	0.44871	5389484	1.15
W+γ+Np2	2.139×10^{-5}	0.54461	2899389	1.15

Table 1.2: Monte Carlo background samples used and parameters, two of two.

Process	Generator	PDF set	σ [pb]	N_{gen}
$h \to aa \to 4\gamma$				
m_a (GeV/c^2)				
$(gg \to h)$	Powheg+Pythia 8	CTEQ6M	13.533	30000
$Z \to 3\gamma$	MadGraph 5	CTEQ6L1	3.566×10^{-6}	30000

Table 1.3: Monte Carlo signal samples used. The cross section for the BSM Higgs scenario is for the gluon-gluon production of the Higgs only, assuming a branching ratio of $h \to aa$ of 100%.

As an example of a BSM process to which this search is sensitive, simulated samples of a Higgs boson decaying into four photons via two intermediate pseudoscalar (a) particles are produced. Powheg-Box is used for the production of a Higgs via gluon-gluon fusion and Pythia for the decay of the Higgs into four photons, for an m_a range from 1 to 62 GeV/c^2.

The rare process of a SM Z boson decaying into three photons is simulated with MadGraph, using a custom model produced with FeynRules [36, 37].

The parton distribution functions for the MadGraph, Pythia and Alpgen + Herwig samples are taken from CTEQ6L1 [38]; for the Powheg-Box samples from CTEQ6M [38]; and for the Sherpa samples from CT10 [39].

Tables 1.1 and 1.2 list the MC background samples used while Table 1.3 lists the MC signal samples used, along with the associated generator, PDF set, cross section, number of events generated, filter efficiency, and k-factor (the ratio of the next-to-leading order cross section contribution to the leading order cross section contribution), when appropriate.

Additionally, minimum bias pp interactions (pileup) in the same or nearby bunch crossings are modeled with Pythia. All simulated events are re-weighted to reproduce the distribution of average number of interactions per bunch crossing

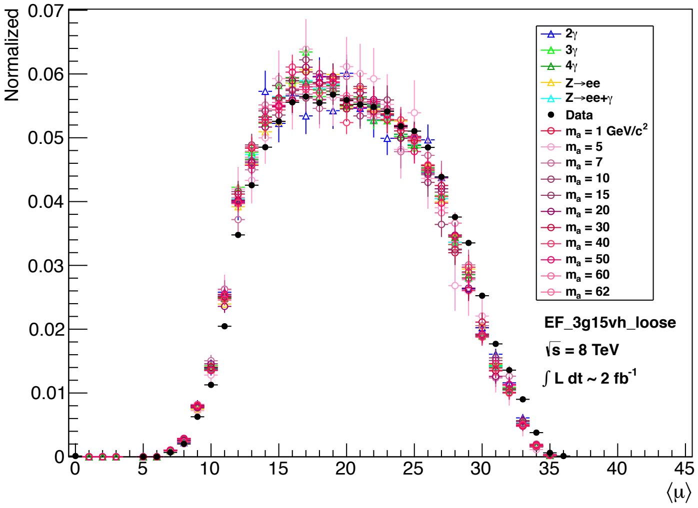

Figure 1.6: Average number of interactions per bunch crossing, $\langle\mu\rangle$, for the 2012 dataset and MC samples used in this analysis. The MC is weighted to the distribution seen in data. The open circles are for MC samples of the BSM process of $h \to aa \to 4\gamma$, for eleven different m_a points.

($\langle\mu\rangle$) observed in data over the course of the 2012 LHC run. The distributions of $\langle\mu\rangle$ for the data and MC considered in this analysis, after re-weighting, are shown in Figure 1.6.

1.4 Object and event selection

This analysis is an inclusive search for events with at least three tight, isolated photons.

1.4.1 Event preselection

The preselection of events corresponds to the following requirements:

- Trigger: This search utilizes a three-photon trigger, `EF_3g15vh_loose`, that

Data	N_{events}
GRL	361945
Trigger, `EF_3g15vh_loose`	361945
No LAr/Tile error	361078
PV ≥ 1	361078

Table 1.4: Events passing preselection criteria, for 10% of 2012 data, at $\sqrt{s} = 8$ TeV.

places a minimum p_T cut of 15 GeV/c on three L1 clusters in the electromagnetic (EM) calorimeter and requires that each cluster satisfy a trigger-level loose photon identification. The trigger requirement is applied as the first preselection requirement on data.

- Good Runs List: Events must correspond to run numbers and lumiblock numbers as determined by a ATLAS central repository, known as a Good Runs List (GRL).
- LAr and Tile errors: Events are rejected if they are found to have liquid argon or tile calorimeter errors.
- Primary vertices: Events are required to contain at least one primary vertex.

The cut flow for event preselection is shown in Table 1.4.

1.4.2 Object selection

After event preselection, selected reconstructed photons then must satisfy the following requirements:

- Pseudorapidity range: Either $|\eta| < 1.37$ or > 1.52, and also $|\eta| < 2.37$, to ensure that photons appear in good regions of the detector.

Data	N$_{photons}$
Event preselection	1436802
Failed pseudorapidity cuts	90891
Failed AR bit	0
Failed object quality/cleaning	11354
Failed loose ID	634796
Failed ΔR cut	592
Passed all	686145

Table 1.5: Number of photon candidates that fail any of the good photon object selection criteria, starting with the total number of photons after event preselection, as well as the resulting total number of good photons that pass all criteria, for 10% of 2012 data, at $\sqrt{s} = 8$ TeV. The events have been preselected from all 2012 data to match the trigger requirement. Hence, the inclusion of the second line, here, is simply a validation of this preselection.

- Ambiguity resolver: Inner tracker information is used to reduce the contribution of electrons faking photons. This is done by applying a bitmask such that reconstructed photon objects that satisfy specific criteria are rejected.
- Object quality/cleaning: Photon candidates are rejected if they resemble sporadic noise bursts or their energy clusters fail object quality criteria corresponding to improperly functioning electronics in the LAr calorimeter.
- Loose ID: In addition to the trigger-level loose ID, photons must satisfy a standard offline loose (L) identification [40].

Table 1.5 shows the number of photons that fail any of the good photon object selection criteria, starting with the total number of photons after event preselection, as well as the resulting total number of good photons that pass all criteria.

1.4.3 Isolation energy correction

The analysis uses a photon isolation definition that calculates isolation based on topological clusters in the electromagnetic calorimeter. This variable, for an isolation cone of size $\Delta R = 0.4$, and with an isolation cut of $E_T^{topo\ iso} < 4$ GeV, is the ATLAS recommended photon isolation scheme for analyses using 2012 data.

To improve sensitivity to new phenomena which result in more collimated photon pairs, a correction is applied to the transverse isolation energy $E_T^{topo\ iso}$ values of a photon candidate (the "target" photon) for which another energetic photon candidate is within a cone of size $\Delta R = 0.4$. The $E_T^{topo\ iso}$ value of each photon is calculated in a standard way, by summing all energy deposits in EM and hadronic calorimeter cells within a cone of $\Delta R = \sqrt{(\Delta\eta)^2 + (\Delta\phi)^2} = 0.4$ around the centre of the cluster, excluding the energy of the photon itself [41]. To further correct for these isolation-overlapping photons, the following procedure is applied: For each target photon, if other photons with $p_T > 15$ GeV/c are found within the cone of the target, their p_T values are subtracted from the $E_T^{topo\ iso}$ of the target. The procedure is performed with the nominal p_T value of each overlapping photon, and the $E_T^{topo\ iso}$ variable of the target photon, which has been corrected using standard analysis tools provided by central ATLAS software development. The procedure is validated on MC samples. Figures 1.7 through 1.10 show the $E_T^{topo\ iso}$ distributions for the leading photon passing the T criterion, for two MC samples representing new phenomena, in this case the decay of a Higgs boson into four photons via intermediate pseudoscalars (a), for lower m_a values with the correction applied and for $m_a = 50$ GeV/c^2 with no correction. For the lower m_a values the photons overlap more often, and the correction procedure results in an isolation distribution similar to that of photons where no overlap occurs and no correction has been applied.

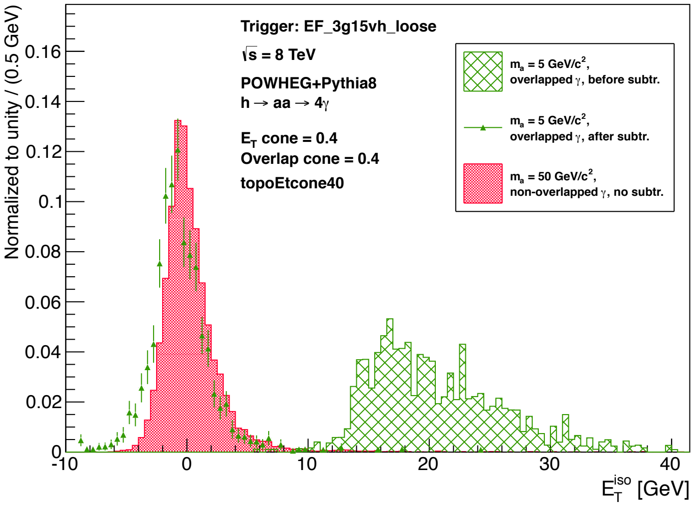

Figure 1.7: Validation of the $E_T^{topo\ iso}$ overlap correction on MC. The distribution of triangles and the cross-hatched histogram are for $m_a = 5$ GeV/c^2 where, due to the lower value of m_a, final state photon pairs frequently overlap; plotted here are only those target photons where another energetic photon has been found within the cone of the target photon. The cross-hatched histogram is for these target photons before correction, and the triangle points are after an overlap correction has been applied. The filled histogram is for $m_a = 50$ GeV/c^2, where, due to the higher value of m_a, little overlap between photon pairs is expected; plotted here are only those target photons where another energetic photon has not been found within the cone of the target photon, and thus no overlap correction has been applied.

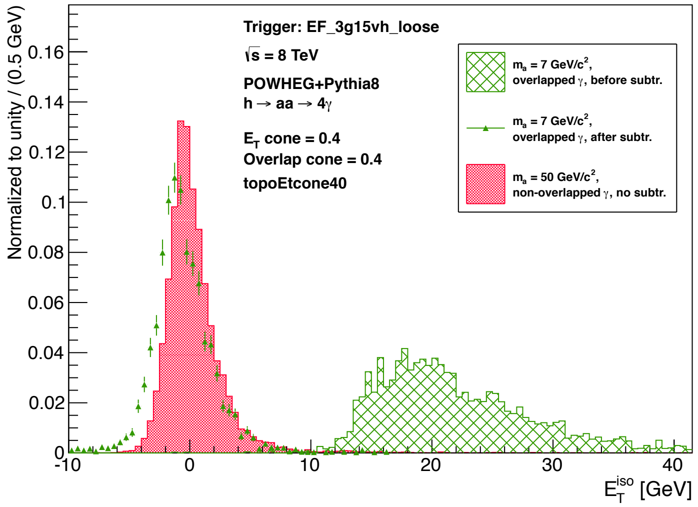

Figure 1.8: Validation of the $E_T^{topo\ iso}$ overlap correction on MC, as previously, but here for m_a = 7 and 50 GeV/c^2.

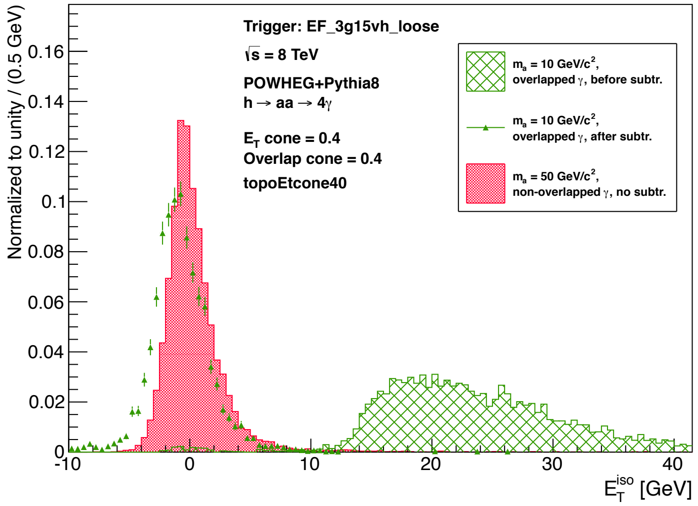

Figure 1.9: Validation of the $E_T^{topo\ iso}$ overlap correction on MC, as previously, but here for m_a = 10 and 50 GeV/c^2.

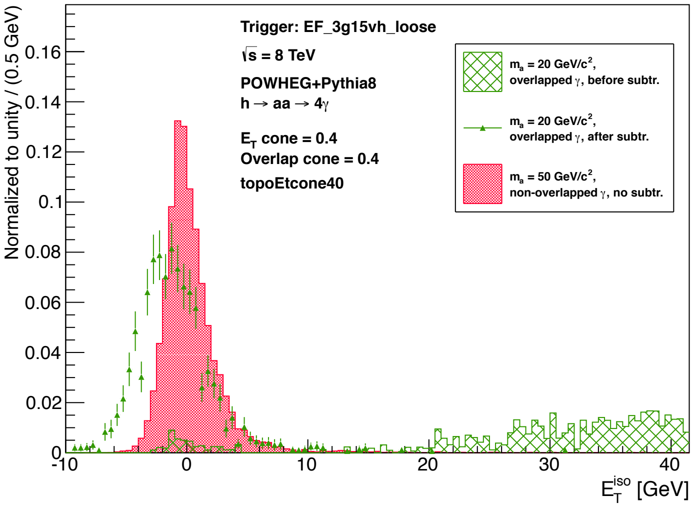

Figure 1.10: Validation of the $E_T^{topo\ iso}$ overlap correction on MC, as previously, but here for $m_a = 20$ and 50 GeV/c^2. Note that for $m_a = 20$ GeV/c^2 there are fewer overlapping photons found than for the lower m_a points.

1.4.4 Signal and control regions

The signal and control regions of multi-photon events are defined starting with the set of events that pass event preselection and contain at least three photons that each pass the above object selection requirements, and additionally pass photon p_T cuts as follows: Photons are ordered by p_T, highest to lowest, and the first three are required to have $p_T >$ 22, 22, and 17 GeV/c respectively. The final two variables used to define signal and control regions are the standard tight (T) ID [42] and the transverse isolation energy of each photon. Isolated photons are those that satisfy $E_T^{topo\ iso} < 4$ GeV. The signal region is composed of preselected events with three good photons that pass the p_T cuts and are all T and isolated.

The signal region is supplemented by several control regions, where at least one of the photon candidates fails either T or isolation, or fails both. These control regions are then used to validate aspects of the analysis.

Data	N_{events}
Three good photons	100121
$p_T > 22$, 22, 17 GeV/c	12226
All three tight	363
All three isolated	141

Table 1.6: Events passing signal region selection criteria, after event preselection and photon object selection, for 10% of 2012 data, at $\sqrt{s} = 8$ TeV.

The cut flow for events falling into the signal region, after event preselection and photon object selection, is shown in Table 1.6.

1.5 Backgrounds

1.5.1 Irreducible photon backgrounds from Monte Carlo

An irreducible background for this search is the prompt production of two photons where a third photon arises from the underlying event. This process is simulated with a Pythia MC sample, described in Section 1.3.2. This sample, in addition to containing 2γ events, also allows for the production of γ+jet events; the only requirement is that events contain at least two hard process or parton shower photons with $p_T > 20$ GeV/c. To avoid double-counting with the exclusive $2\gamma + 1$j (where the jet fakes a photon) backgrounds determined via the data-driven method, truth information is used to select only those events in the 2γ MC that contain three true photons.

Additionally, possible irreducible photon backgrounds from W+$\gamma\gamma$ and SM $h \to \gamma\gamma$ have been investigated and have been found to be negligible.

1.5.2 Scaling of electron backgrounds from Monte Carlo

Backgrounds from processes involving electrons in the final state are modeled with MC. The SM Z boson can decay to an electron-positron pair, and these decay products can be misidentified as photons. Occasionally, an additional photon from initial- or final-state radiation is produced, giving rise to a final state that can be a background to a three-photon search. Possible mis-measurement of the rate of electrons faking photons in MC is addressed with a scale factor.

A subset of 2012 data was selected, using an OR of two electron triggers, `EF_e24vhi_medium1` and `EF_e60_medium1`, which indicate that the event must contain at least one electron satisfying trigger-level medium electron identification criteria, and must satisfy either criteria optimized for lower- or higher-energy electron objects. The energy and shower variables of electrons are then calibrated and events containing one and only one good electron satisfying a more stringent ID criterion, called `tightPP`, with $p_T > 30$ GeV/c and an isolation cut of $E_T^{topo\ iso} < 4$ GeV, plus one and only one good tight, isolated photon with $p_T > 17$ GeV/c, are selected. Invariant mass values are calculated for pairs consisting of the good calibrated photon in the event and the "tagged" electron. With the further requirement that this invariant mass be near the SM Z boson mass, this procedure provides a sample of events in data that have a high probability of arising from a SM Z boson decaying to an electron-positron pair, where one of the electrons has faked a photon. By comparing the distributions of $m_{e,\gamma}$ in data and Z→ e^+e^- MC, which should agree in a range near the Z mass, one can subtract the MC prediction from the data. This should result in a Z-background-subtracted spectrum that is primarily composed of true Z events near the Z mass and all other backgrounds (not included in the MC) in the regions away from the Z mass. By fitting a polynomial to these sideband regions, one can extrapolate into the region around the Z mass and thus determine the non-Z backgrounds not subtracted from the Z MC subtraction. By then subtracting this remaining non-Z background (via the sideband procedure) one can arrive at the distribution of events not estimated by MC, and, thus, the scaling factor that needs to be applied to Z$\rightarrow e^{+}e^{-}$ MC. This procedure is performed on MC, weighted to 2 fb^{-1}, which corresponds to the luminosity of the electron trigger selection of 2012 data for this study. The resulting $m_{e,\gamma}$ distributions for four separate regions of the $\eta - p_T$ plane are shown in Figures 1.11 through 1.14.

The distributions are calculated for separate photon η and p_T regions, and restricted to a window around the Z mass of $70 < m_{e,\gamma} < 140$ GeV/c^2. The MC is then subtracted from the data, and a second-order polynomial is fit to the sidebands of the subtracted distribution, for $70 < m_{e,\gamma} < 78$ GeV/c^2 and $102 < m_{e,\gamma} < 140$ GeV/c^2, as shown in Figures 1.15 through 1.18. The lower bound of $m_{e,\gamma} > 70$ GeV/c^2 is chosen so as to not be affected by the p_T requirements placed on the electron and photon. The tagged electron is required to have $p_{T,e} > 30$ GeV/c, and whereas the overall photon p_T requirement is $p_{T,\gamma} > 17$ GeV/c, this becomes $p_{T,\gamma} > 35$ GeV/c for the higher $p_{T,\gamma}$ range.

The integral of the polynomial fit in the excluded region around the Z peak, for $78 < m_{e,\gamma} < 102$ GeV/c^2, gives the contribution of all other backgrounds not accounted for in the MC stack. This contribution is then subtracted from the full distribution in data, and the scale factor is calculated as (data - background)/MC. This factor is calculated for each region in the $\eta - p_T$ plane; the results are shown in Table 1.7. To determine the contribution of backgrounds with electrons faking photons in the signal region, truth information is used in MC to determine when a

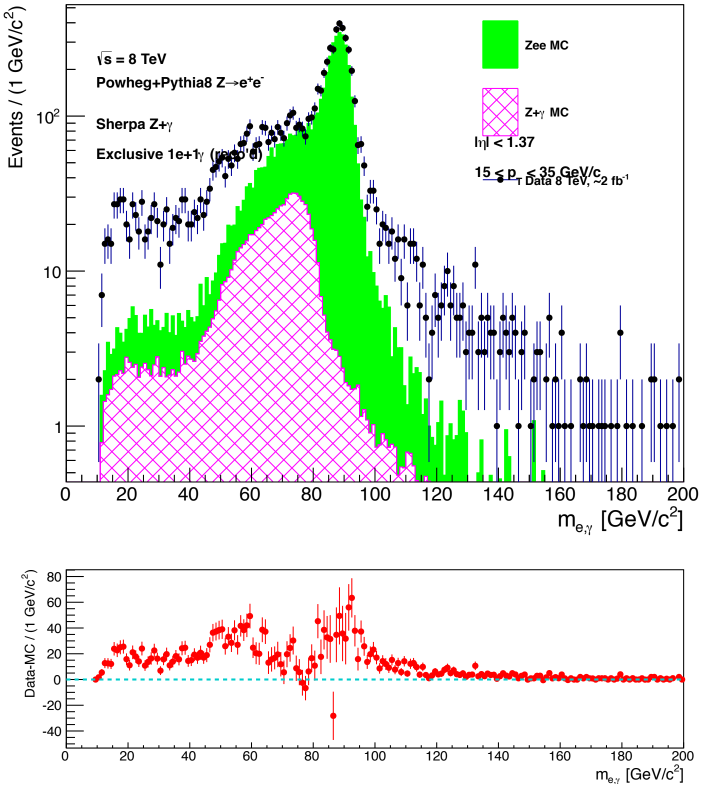

Figure 1.11: Invariant mass of an electron and a photon in events with only one electron and one photon, for 10% of 2012 data and Powheg+Pythia8 Z→ e^+e^- MC and Sherpa Z+γ MC, in events that pass an OR of two electron triggers, `EF_e24vhi_medium1` and `EF_e60_medium1`, for $|\eta_\gamma| < 1.37$ and $15 < p_{T,\gamma} < 35$ GeV/c. Also shown is the subtraction of MC from data.

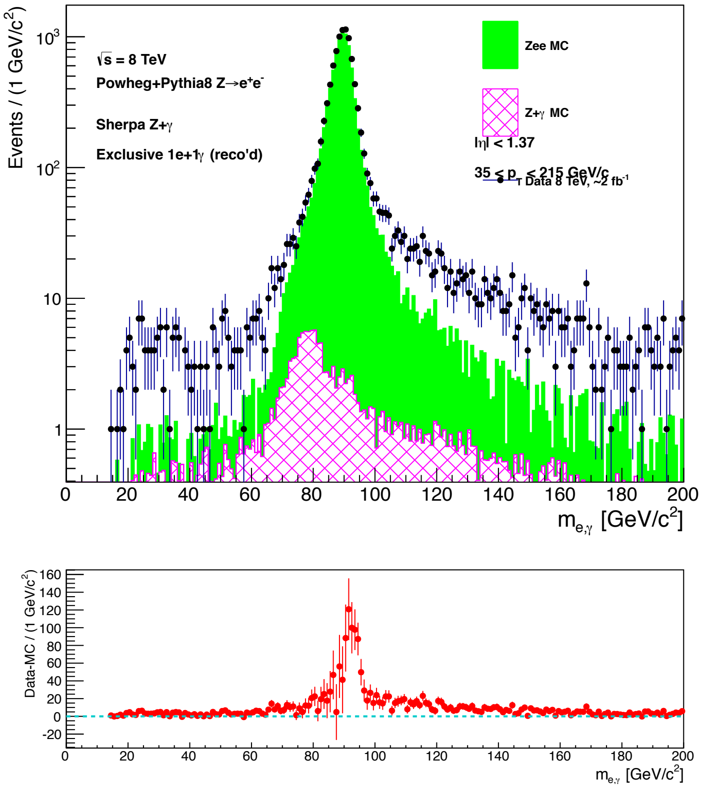

Figure 1.12: Invariant mass of an electron and a photon in events with only one electron and one photon, for 10% of 2012 data and Powheg+Pythia8 Z→ e^+e^- MC and Sherpa Z+γ MC, in events that pass an OR of two electron triggers, `EF_e24vhi_medium1` and `EF_e60_medium1`, for $|\eta_\gamma| < 1.37$ and $p_{T,\gamma} > 35$ GeV/c. Also shown is the subtraction of MC from data.

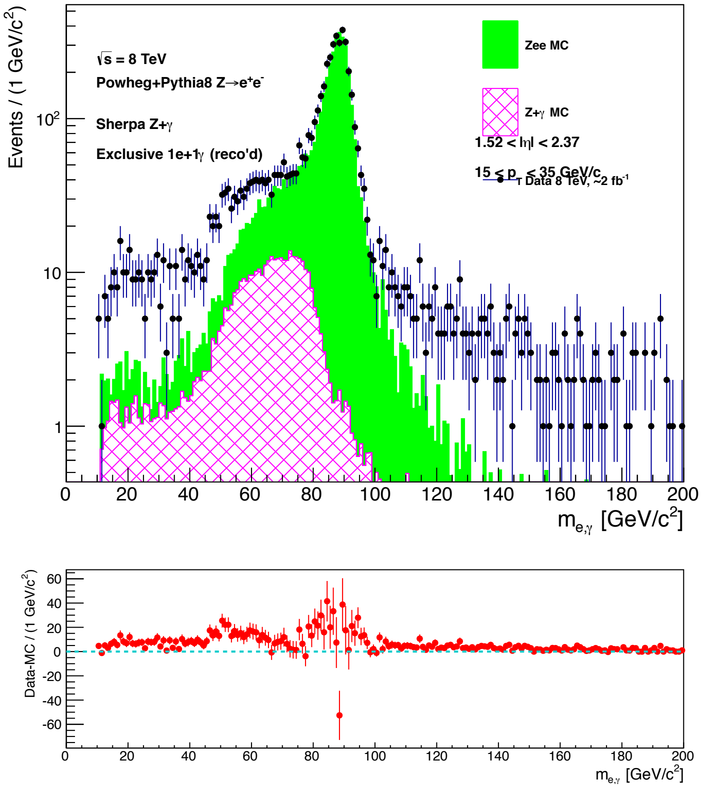

Figure 1.13: Invariant mass of an electron and a photon in events with only one electron and one photon, for 10% of 2012 data and Powheg+Pythia8 Z→ e^+e^- MC and Sherpa Z+γ MC, in events that pass an OR of two electron triggers, `EF_e24vhi_medium1` and `EF_e60_medium1`, for $1.52 < |\eta_\gamma| < 2.37$ and $15 < p_{T,\gamma} <$ 35 GeV/c. Also shown is the subtraction of MC from data.

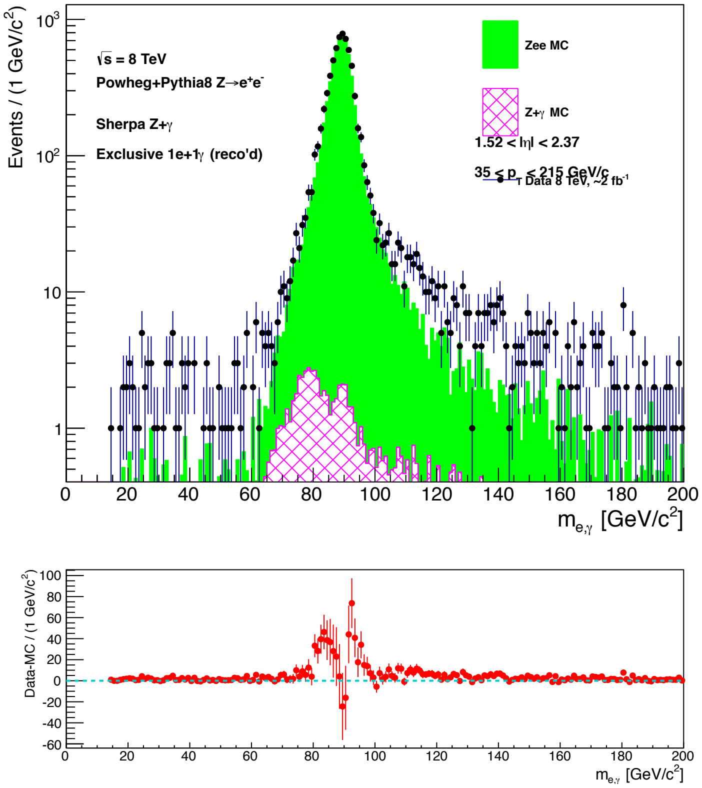

Figure 1.14: Invariant mass of an electron and a photon in events with only one electron and one photon, for 10% of 2012 data and Powheg+Pythia8 Z→ e^+e^- MC and Sherpa Z+γ MC, in events that pass an OR of two electron triggers, `EF_e24vhi_medium1` and `EF_e60_medium1`, for $1.52 < |\eta_\gamma| < 2.37$ and $p_{T,\gamma} > 35$ GeV/c. Also shown is the subtraction of MC from data.

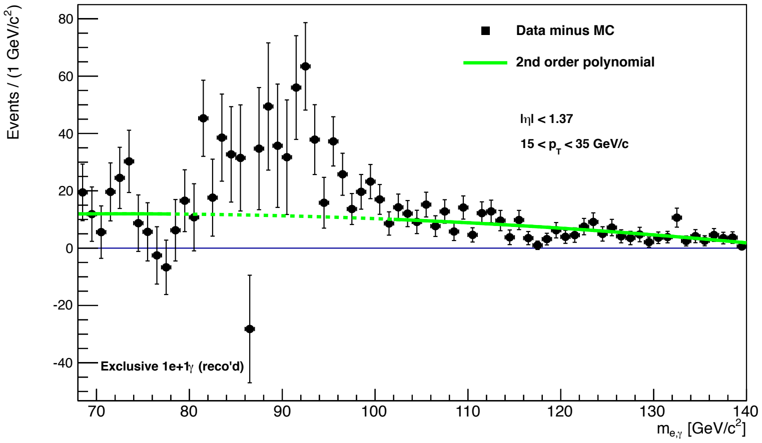

Figure 1.15: Subtraction of Powheg+Pythia8 Z→ e^+e^- MC and Sherpa Z+γ MC from 10% of 2012 data for $e\gamma$ invariant mass in events with only one electron and one photon, in events that pass an OR of two electron triggers, `EF_e24vhi_medium1` and `EF_e60_medium1`, for $|\eta_\gamma| < 1.37$ and $15 < p_{T,\gamma} < 35$ GeV/c, with a second-order polynomial sideband fit.

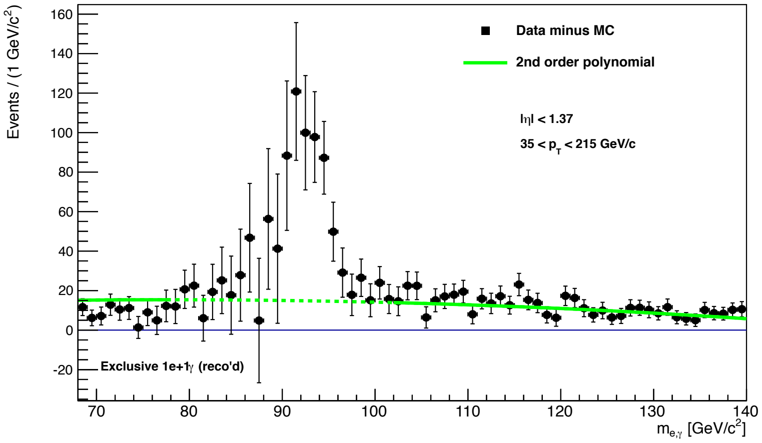

Figure 1.16: Subtraction of Powheg+Pythia8 Z→ e^+e^- MC and Sherpa Z+γ MC from 10% of 2012 data for $e\gamma$ invariant mass in events with only one electron and one photon, in events that pass an OR of two electron triggers, `EF_e24vhi_medium1` and `EF_e60_medium1`, for $|\eta_\gamma| < 1.37$ and $p_{T,\gamma} > 35$ GeV/c, with a second-order polynomial sideband fit.

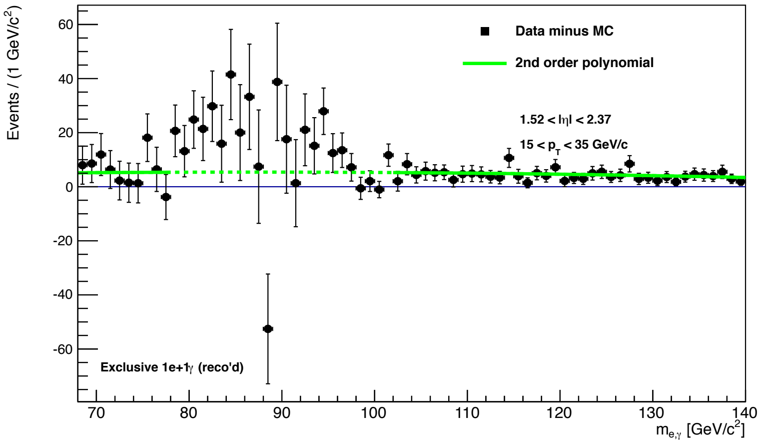

Figure 1.17: Subtraction of Powheg+Pythia8 Z→ e^+e^- MC and Sherpa Z+γ MC from 10% of 2012 data for $e\gamma$ invariant mass in events with only one electron and one photon, in events that pass an OR of two electron triggers, `EF_e24vhi_medium1` and `EF_e60_medium1`, for $1.52 < |\eta_\gamma| < 2.37$ and $15 < p_{T,\gamma} <$ 35 GeV/c, with a second-order polynomial sideband fit.

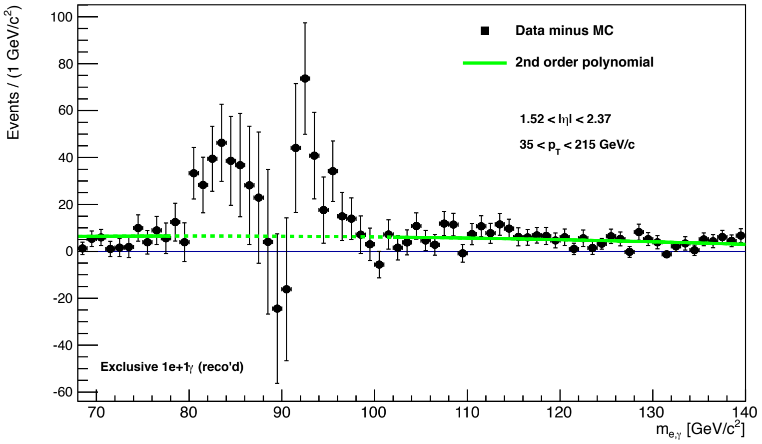

Figure 1.18: Subtraction of Powheg+Pythia8 Z→ e^+e^- MC and Sherpa Z+γ MC from 10% of 2012 data for $e\gamma$ invariant mass in events with only one electron and one photon, in events that pass an OR of two electron triggers, `EF_e24vhi_medium1` and `EF_e60_medium1`, for $1.52 < |\eta_\gamma| < 2.37$ and $p_{T,\gamma} > 35$ GeV/c, with a second-order polynomial sideband fit.

	$15 < p_{T,\gamma} < 35$ GeV/c	$p_{T,\gamma} > 35$ GeV/c
$\lvert\eta\rvert < 1.37$	1.0301 ± 0.0250	1.0300 ± 0.0159
$1.52 < \lvert\eta\rvert < 2.37$	1.0249 ± 0.0215	1.0304 ± 0.0154

Table 1.7: Scaling factors calculated from an electron tag-and-probe method for processes involving Z→ e^+e^-, and applied to true electrons that have faked photons in electron MC.

tight, isolated photon is actually an electron faking a photon, and the event weight is multiplied by the appropriate scaling factor or factors as a function of photon η and p_T.

1.5.3 Jet background estimation

A crucial aspect of the analysis is the data-driven estimate of the jet backgrounds, i.e., SM processes that can produce 2γ+1j, 1γ+2j, and 3j events. Collision data is used to derive efficiencies for photons passing isolation and rates for jets faking isolated photons. The efficiencies and fake rates are then used in a likelihood matrix method to arrive at the final jet background estimate. These approaches are described in detail below.

1.5.3.1 Photon isolation efficiencies and jet fake rates

The standard tight (T) and loose (L) photon identification categories are augmented with a loose-prime (L′) definition [43, 44], intermediate between T and L, that relaxes four strip cuts and, when combined with a further requirement that the photon candidate fail T, provides a sample of photon candidates that is primarily composed of jets faking photons. (For the rest of this note, "L′" denotes the combined requirement of L′-and-not-T.) This method presupposes that 1) the

$E_T^{topo\ iso}$ distribution of the L$'$ sample is composed primarily of jets faking photons, and 2) the tail of the $E_T^{topo\ iso}$ distribution of T photons is dominated by jets faking photons. Under these assumptions, the tail of the L$'$ distribution is scaled to match that of the T distribution, thus providing a determination of the contribution of jets faking photons to the T and isolated sample. This procedure is illustrated in Figure 1.19, which shows the $E_T^{topo\ iso}$ distributions described here for all photon candidates in events passing the `EF_3g15vh_loose` trigger requirement in the full 2012 dataset.

The assumptions described above are checked with and validated on MC samples, as shown in Figure 1.20. A MC sample of multi-jet processes containing photons, generated with PYTHIA 8 at $\sqrt{s} = 8$ TeV, is utilized. Agreement is shown between the $E_T^{topo\ iso}$ distributions of true jets faking T photons and reconstructed L$'$ photons. The procedure of scaling the tail of the L$'$ distribution to that of the T distribution and then subtracting the scaled-L$'$ from the T yields a distribution that is then compared to the $E_T^{topo\ iso}$ distribution of true photons; the distributions should agree. The non-zero true photon contamination in the L$'$ and T-and-not-isolated regions is addressed by assigning a systematic uncertainty, discussed in Section 1.6.1.

For the analysis, photon isolation efficiencies and jet fake rates are calculated as follows: Photons are ordered by p_T, highest to lowest, and then three regions in the $p_T - \eta$ plane are defined in which to calculate photon isolation efficiencies and jet fake rates. The three regions are denoted A, B, and C, where Region A is defined as $15 < p_T < 40$ GeV/c and $|\eta| < 1.37$, Region B is defined as $p_T > 40$ GeV/c and $|\eta| < 1.37$, and Region C is defined as $1.52 < |\eta| < 2.37$. A graphical illustration of these regions is shown in Figure 1.21.

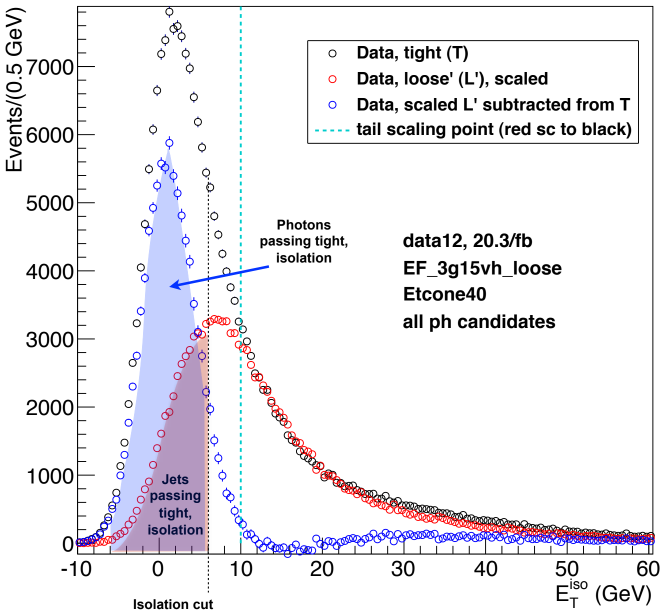

Figure 1.19: Illustration of the procedure for calculating photon isolation efficiencies and jet fake rates described in the text.

Distributions of $E_T^{topo\ iso}$ for T and scaled L′ photon candidates, as well as the subtraction of the scaled L′ from the T, for the three p_T-η bins, are shown in Figures 1.22- 1.24, for $E_T^{topo\ iso}$. For each bin, the L′ distribution is scaled to the tail of the T distribution by computing the integrals of the tails of both L′ and T within an $E_T^{topo\ iso}$ window of $7 < E_T^{topo\ iso} < 25$ GeV. The factor F_{scale} by which L′ is scaled is then

$$F_{scale} = \frac{\int_7^{25} f_T(E_T^{topo\ iso})\ dE_T^{topo\ iso}}{\int_7^{25} f_{L'}(E_T^{topo\ iso})\ dE_T^{topo\ iso}}. \tag{1.1}$$

Photon efficiencies and jet fake rates are then calculated as

$$\epsilon_{photon} = \frac{\int_{-10}^{4} \left[f_T(E_T^{topo\ iso}) - F_{scale} f_{L'}(E_T^{topo\ iso})\right]\ dE_T^{topo\ iso}}{\int_{-10}^{70} \left[f_T(E_T^{topo\ iso}) - F_{scale} f_{L'}(E_T^{topo\ iso})\right]\ dE_T^{topo\ iso}} \tag{1.2}$$

and

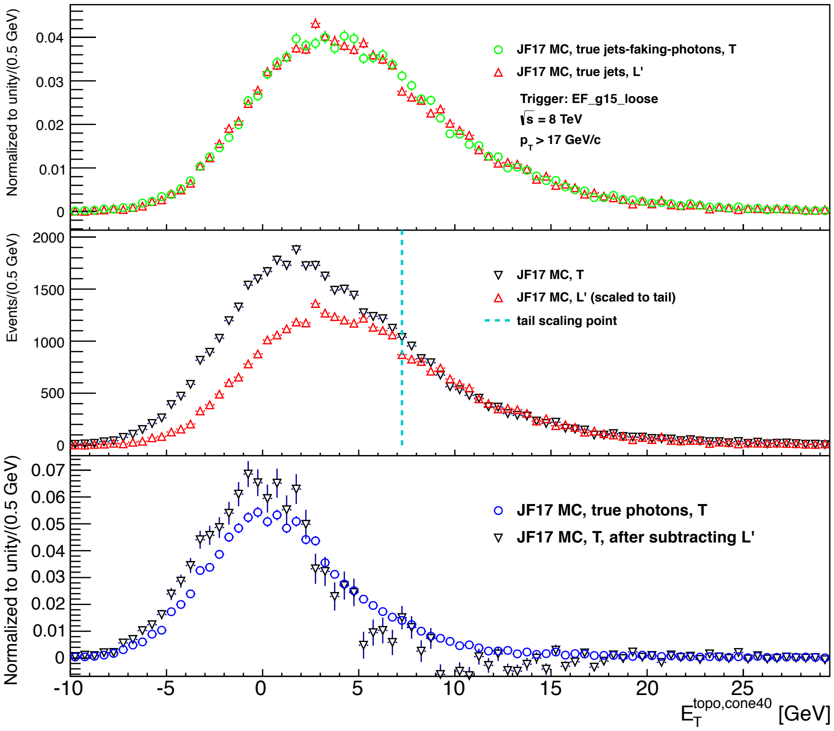

Figure 1.20: Validation on MC of the data-driven method of calculating photon isolation efficiencies and jet fake rates using the T and L′ photon ID definitions. The MC sample used is a Pythia 8 JF17 jet sample, at $\sqrt{s} = 8$ TeV. Top: the $E_T^{topo\ iso}$ distributions of true jets faking T photons and reconstructed L′ photons. Middle: The tail of the L′ distribution is scaled to that of the T distribution. Bottom: The scaled-L′ distribution is subtracted from the T, and is plotted with the distribution of true photons.

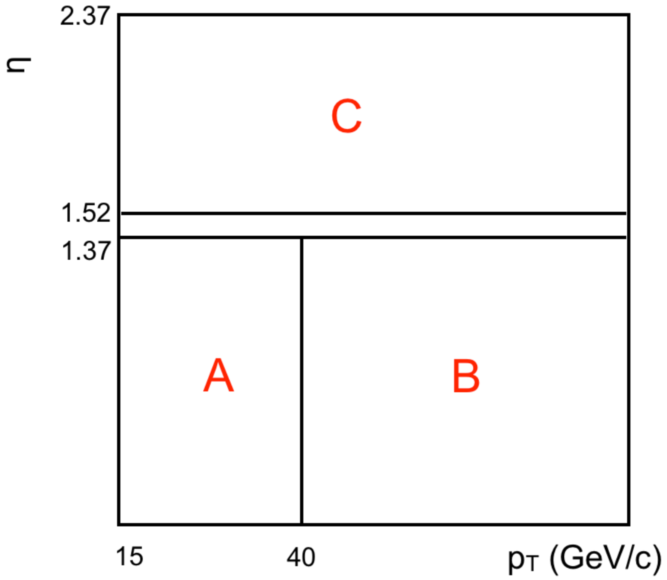

Figure 1.21: A graphical illustration of the three regions in the $p_T - \eta$ plane defined for the calculation of photon isolation efficiencies and jet fake rates, which are then used in the jet background determination.

$$f_{jet} = \frac{\int_{-10}^{4} F_{scale} f_{L'}(E_T^{topo\ iso})\ dE_T^{topo\ iso}}{\int_{-10}^{70} F_{scale} f_{L'}(E_T^{topo\ iso})\ dE_T^{topo\ iso}}, \tag{1.3}$$

recalling that an isolated photon candidate satisfies $E_T^{topo\ iso} < 4$ GeV.

The resulting photon isolation efficiencies and jet fake rates are shown in Figure 1.25.

1.5.3.2 Likelihood matrix method

The data-derived photon efficiencies and jet fake rates are applied to the full sample of data events with three photon candidates. This is done using a likelihood matrix method (LMM), where the expected yield for each three-object final state consisting of jets plus photons or all jets — 2γ+1j, 1γ+2j, 3j — is the result of a fit to the data. For each three-photon combination of T or L′ (TTT, TTL′, etc.,

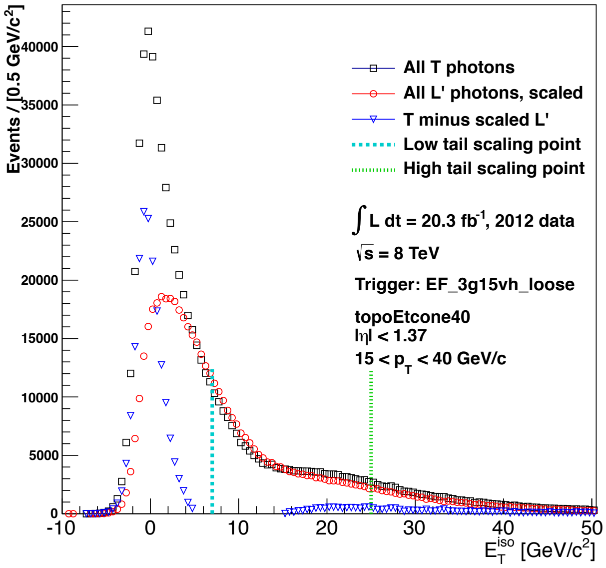

Figure 1.22: Distributions of $E_T^{topo\ iso}$ for T and scaled L′ photon candidates, as well as the subtraction of the scaled L′ from the T, for photons in Region A, defined as $15 < p_T < 40$ GeV/c and $|\eta| < 1.37$.

where "L′" denotes L′-and-not-T), events are placed into orthogonal categories designated by the three values of a kinematic variable (or combination of kinematic variables) and passed-or-failed-isolation statuses of the photon candidates. The baseline analysis utilizes three regions in the $p_T - \eta$ plane to categorize photons and to calculate isolation efficiencies and fake rates. As a cross-check, however, the analysis is performed separately with the kinematic variables of photon p_T and photon η. For simplicity, for the remainder of this section, the procedure is described for p_T-only, but the procedure is similar for each choice of kinematic variable or combination, differing only in the number of kinematic variable categories available for three p_T-ordered photons to populate.

Since each photon either passes (P) or fails (F) isolation, there are $2^3 = 8$ possible isolation combinations for three photons: PPP, PPF, PFP, FPP, PFF,

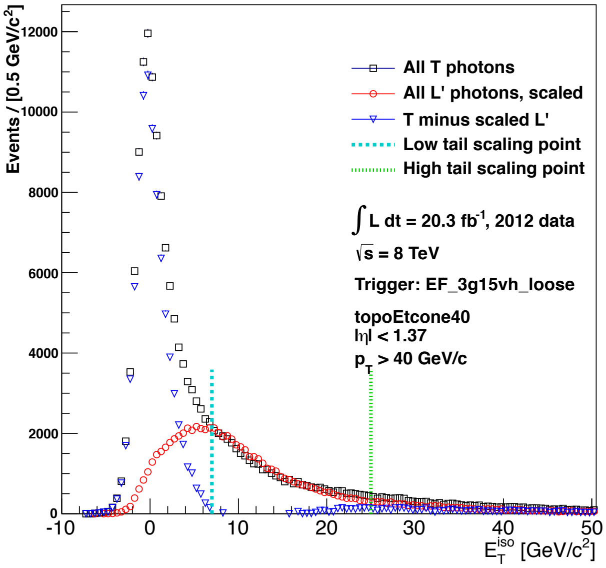

Figure 1.23: Distributions of $E_T^{topo\ iso}$ for T and scaled L′ photon candidates, as well as the subtraction of the scaled L′ from the T, for photons in Region B, defined as $p_T > 40$ GeV/c and $|\eta| < 1.37$.

FPF, FFP, and FFF. Photon isolation efficiencies and jet fake rates are binned in three bins of p_T, denoted L for low, M for medium, and H for high, where $15 < p_T^L \leq 50$ GeV/c, $50 < p_T^M \leq 80$ GeV/c, and $p_T^H > 80$ GeV/c. Since the three photons are ordered by p_T, from highest to lowest, there are ten p_T combinations: HHH, HHM, HHL, HMM, HML, HLL, MMM, MML, MLL, and LLL. This results in $8 \times 10 = 80$ categories, denoted PPP_HHH for those events where the three photon candidates all passed isolation and had H p_T values, PPF_HML for those events where the leading and subleading photons passed isolation and the sub-subleading photon failed isolation, and the p_T values were H, M, and L for the leading, subleading and sub-subleading photons, respectively, etc. The observed number of events in each category, for 10% of 2012 data, is shown in Figure 1.26.

The LMM is related to standard matrix methods in the following way. In

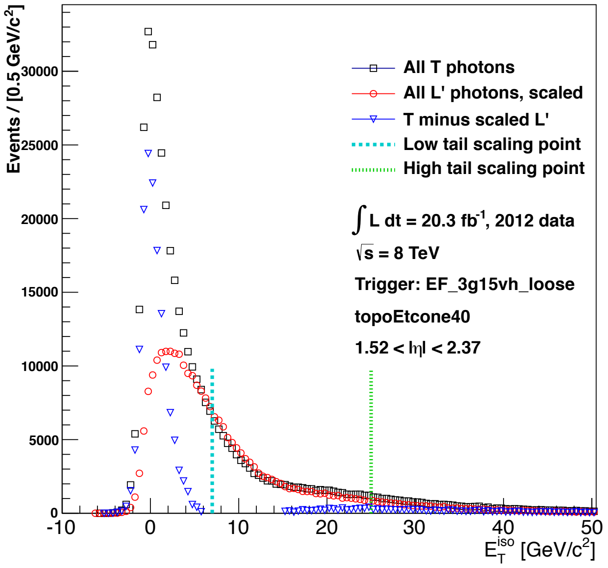

Figure 1.24: Distributions of $E_T^{topo\ iso}$ for T and scaled L$'$ photon candidates, as well as the subtraction of the scaled L$'$ from the T, for photons in Region B, defined as $1.52 < |\eta| < 2.37$.

standard matrix methods, two orthogonal criteria, e.g., photon ID (T,L') and photon isolation (P,F), serve as the basis to a per-photon two-dimensional plane made up of categories that are populated differently by real photons and jets faking photons. For a given selection of photon candidates in one of the bins, e.g., photons that pass T ID, one can determine (via data-driven methods or MC studies) the rates of true photons passing the other criterion (here, passing isolation) and the rates of jets faking photons in the same region. The relationship between the observed photon isolation status and the true final object (photon or jet) is encoded in these efficiencies and fake rates. In the present case, on an event level, this turns into a space made up of a combination of three separate ID and isolation statuses, one for each of the three photons, and the number of observed combination and true final states is increased, as described above, to eight. This

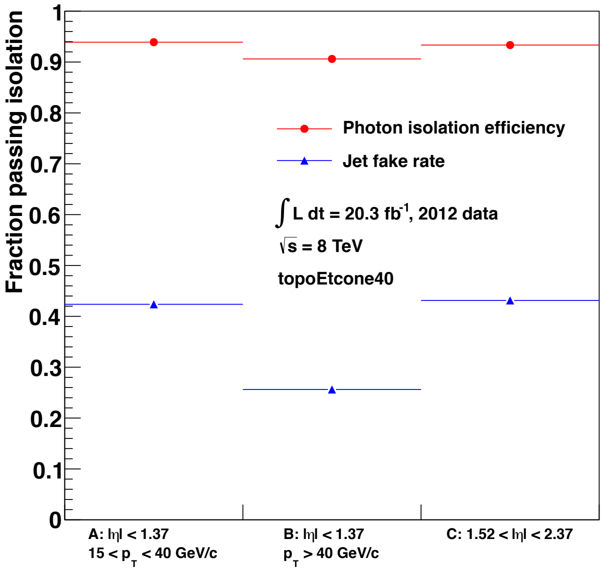

Figure 1.25: Photon isolation efficiencies and jet fake rates from collision data for the three regions in the $p_T - \eta$ plane, used for the jet background estimate, using $E_T^{topo\ iso}$. Photons with $1.37 < |\eta| < 1.52$ are excluded from the analysis.

is expressed as a matrix equation, shown in Eq. 1.4.

$$\begin{pmatrix} N_{\mathrm{PPP}} \\ N_{\mathrm{PPF}} \\ N_{\mathrm{PFP}} \\ N_{\mathrm{FPP}} \\ N_{\mathrm{PFF}} \\ N_{\mathrm{FPF}} \\ N_{\mathrm{FFP}} \\ N_{\mathrm{FFF}} \end{pmatrix} = \begin{pmatrix} \epsilon_1\epsilon_2\epsilon_3 & \epsilon_1\epsilon_2 f_3 & \epsilon_1 f_2\epsilon_3 & f_1\epsilon_2\epsilon_3 & \epsilon_1 f_2 f_3 & f_1\epsilon_2 f_3 & f_1 f_2\epsilon_3 & f_1 f_2 f_3 \\ \epsilon_1\epsilon_2(1-\epsilon_3) & \epsilon_1\epsilon_2(1-f_3) & \epsilon_1 f_2(1-\epsilon_3) & f_1\epsilon_2(1-\epsilon_3) & \text{etc.} & \ldots & \ldots & \ldots \\ \ldots & & & & & & & \\ \ldots & & & & & & & \\ \ldots & & & & & & & \\ \ldots & & & & & & & \\ \ldots & & & & & & & \\ \ldots & & & & & & & \end{pmatrix} \begin{pmatrix} W^{\mathrm{TTT}}_{\gamma\gamma\gamma} \\ W^{\mathrm{TTT}}_{\gamma\gamma\mathrm{j}} \\ W^{\mathrm{TTT}}_{\gamma\mathrm{j}\gamma} \\ W^{\mathrm{TTT}}_{\mathrm{j}\gamma\gamma} \\ W^{\mathrm{TTT}}_{\gamma\mathrm{jj}} \\ W^{\mathrm{TTT}}_{\mathrm{j}\gamma\mathrm{j}} \\ W^{\mathrm{TTT}}_{\mathrm{jj}\gamma} \\ W^{\mathrm{TTT}}_{\mathrm{jjj}} \end{pmatrix} \tag{1.4}$$

In standard matrix methods, this equation is solved on an event-by-event level, and the W^{zzz}_{xxx} values are taken as weights corresponding to each of the possible true final state combinations of photons and jets. Note that nothing prevents these weights from taking negative values. In high-statistics samples, this is typically not a problem, since the weights will sum, over the entire sample, to give the true event yields in each final state.

By contrast, in lower-statistics regimes, the LMM modification of this method provides an improvement over the standard method, since the expected yield for each final state can be constrained to be positive (and hence physical) in the fit. Additionally, it is convenient to increase the number of observed and final state categories, to take into account the p_T and η dependence of the efficiencies and fake rates, and thus more information about the event sample is utilized.

In the context of the current discussion, the number of possible final states for the background estimate method is 80. Each of the 80 categories corresponds to a Poisson function where the observed number of events is the number of events seen in data for that category and the expected number of events is a sum of terms corresponding to each of the possible true final states consisting of photons+jets or only jets for this particular p_T combination, where each term in the sum is multiplied by the appropriate isolation efficiencies and jet fake rates. A likelihood is then constructed consisting of a product of the 80 Poisson terms, as in Eq. 1.5.

$$\begin{aligned}\mathcal{L} \;=\;& Pois(N^{\mathrm{obs}}_{\mathrm{PPP,HHH}} \mid \epsilon_H\epsilon_H\epsilon_H\ \nu^{\mathrm{HHH}}_{\gamma\gamma\gamma} + \epsilon_H\epsilon_H f_H\ \nu^{\mathrm{HHH}}_{\gamma\gamma\mathrm{j}} + \epsilon_H f_H\epsilon_H\ \nu^{\mathrm{HHH}}_{\gamma\mathrm{j}\gamma} + \ \ldots\ ) \times \ldots \\ & \times Pois(N^{\mathrm{obs}}_{\mathrm{PPF,HML}} \mid \epsilon_H\epsilon_M(1-\epsilon_L)\ \nu^{\mathrm{HML}}_{\gamma\gamma\gamma} + \epsilon_H\epsilon_M(1-f_L)\ \nu^{\mathrm{HML}}_{\gamma\gamma\mathrm{j}} + \\ & \epsilon_H f_M(1-\epsilon_L)\ \nu^{\mathrm{HML}}_{\gamma\mathrm{j}\gamma} + \ \ldots\ ) \times \ldots\end{aligned} \tag{1.5}$$

The expectations for each true final state — denoted $\nu^{\mathrm{HML}}_{\gamma\gamma\mathrm{j}}$, etc. — are the result of a fit to the data, and are constrained to be positive. The estimated number of events of a given final state in a particular signal or control region defined by the T or L$'$ ID statuses and P or F isolation statuses of the three photons is determined by summing the resulting expectations ν_{xxx}^{zzz} from the fit times the appropriate efficiencies and fake rates. For example, to determine the estimated number of $\gamma\gamma$j events in the PPP region, the sum given by

$$N_{\gamma\gamma\mathrm{j}}^{PPP} \;=\; \epsilon_H \epsilon_H f_H \; \nu_{\gamma\gamma\mathrm{j}}^{\mathrm{HHH}} + \epsilon_H \epsilon_H f_M \; \nu_{\gamma\gamma\mathrm{j}}^{\mathrm{HHM}} + \;\ldots \tag{1.6}$$

is formed. Possible correlations between the ν_{xxx}^{zzz} variables in the fit are taken into account when calculating the uncertainty on each estimated number of events N_{yyy} by including the covariance terms between variables in a given N_{yyy} sum. For example, the uncertainty on $N_{\gamma\gamma j}^{PPP}$ is given by

$$\begin{aligned} \sigma_{\gamma\gamma\mathrm{j}}^{PPP} \;=\; & \Bigg((\sigma_{\gamma\gamma\mathrm{j}}^{\mathrm{HHH}})^2 + (\sigma_{\gamma\gamma\mathrm{j}}^{\mathrm{HHM}})^2 + \;\ldots \\ & \ldots + 2[\epsilon_H \epsilon_H f_H][\epsilon_H \epsilon_H f_M] \times \mathrm{cov}(\nu_{\gamma\gamma\mathrm{j}}^{\mathrm{HHH}}, \nu_{\gamma\gamma\mathrm{j}}^{\mathrm{HHM}}) + \;\ldots \Bigg)^{1/2} \end{aligned} \tag{1.7}$$

where, e.g., $\sigma_{\gamma\gamma\mathrm{j}}^{\mathrm{HHM}}$ is the uncertainty on the $\epsilon_H \epsilon_H f_M \;\; \nu_{\gamma\gamma\mathrm{j}}^{\mathrm{HHM}}$ term in the sum in Equation 1.6, and is given by

$$\sigma_{\gamma\gamma\mathrm{j}}^{\mathrm{HHM}} = \epsilon_H \epsilon_H f_M \; \nu_{\gamma\gamma\mathrm{j}}^{\mathrm{HHM}} \left[\left(\frac{\sigma_{\epsilon_H}}{\epsilon_H} \right)^2 + \left(\frac{\sigma_{\epsilon_H}}{\epsilon_H} \right)^2 + \left(\frac{\sigma_{f_M}}{f_M} \right)^2 + \left(\frac{\sigma_{\nu_{\gamma\gamma\mathrm{j}}^{\mathrm{HHM}}}}{\nu_{\gamma\gamma\mathrm{j}}^{\mathrm{HHM}}} \right)^2 \right]^{1/2}, \tag{1.8}$$

and $\mathrm{cov}(\nu_{\gamma\gamma\mathrm{j}}^{\mathrm{HHH}}, \nu_{\gamma\gamma\mathrm{j}}^{\mathrm{HHM}})$ is the covariance between the indicated fit values, extracted from the covariance matrix returned by MINUIT.

The method is validated on a MC sample consisting of photon(s)+jet(s) events. Figure 1.27 shows the results of the likelihood matrix method when applied to this

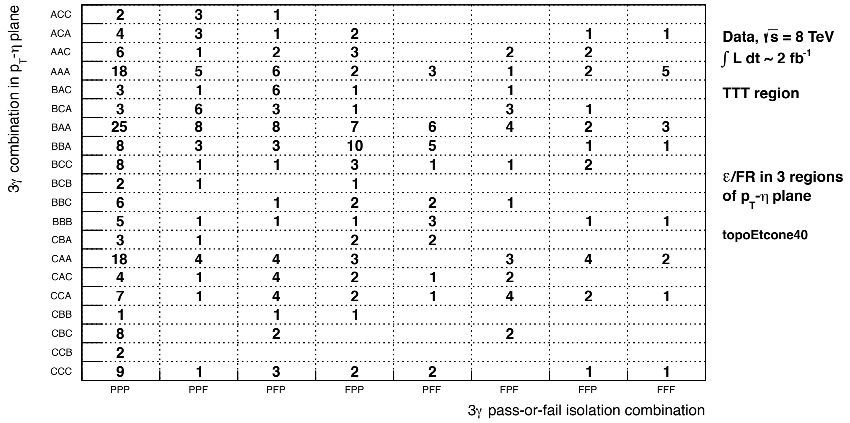

	PPP	PPF	PFP	FPP	PFF	FPF	FFP	FFF
ACC	2	3	1					
ACA	4	3	1	2			1	1
AAC	6	1	2	3		2	2	
AAA	18	5	6	2	3	1	2	5
BAC	3	1	6	1		1		
BCA	3	6	3	1		3	1	
BAA	25	8	8	7	6	4	2	3
BBA	8	3	3	10	5		1	1
BCC	8	1	1	3	1	1	2	
BCB	2	1		1				
BBC	6		1	2	2	1		
BBB	5	1	1	1	3		1	1
CBA	3	1		2	2			
CAA	18	4	4	3		3	4	2
CAC	4	1	4	2	1	2		
CCA	7	1	4	2	1	4	2	1
CBB	1		1	1				
CBC	8		2			2		
CCB	2							
CCC	9	1	3	2	2		1	1

Figure 1.26: Observed number of events in 10% of 2012 data for the orthogonal categories used as inputs to the likelihood matrix method, using $E_T^{topo\ iso}$, where the photon candidates are ordered by p_T, highest to lowest, and photon isolation efficiencies and jet fake rates are calculated for three regions in the $p_T - \eta$ plane.

MC sample, generated with Alpgen [33], for $\sqrt{s} = 7$ TeV, and the true final states in the MC.

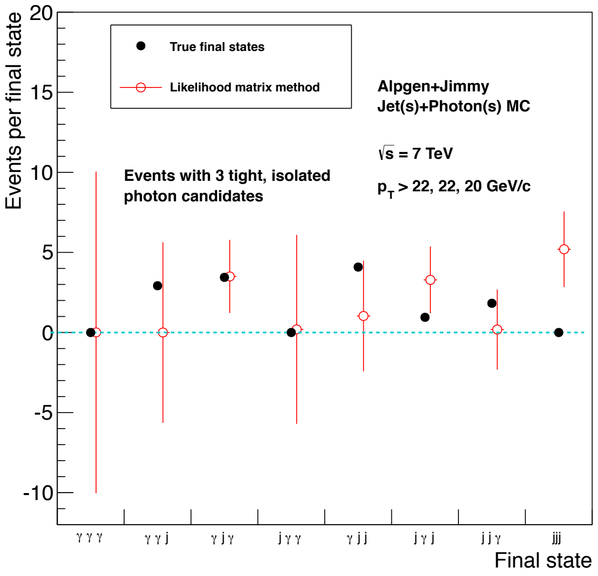

Figure 1.27: Validation of the likelihood matrix method on MC. Filled points are the true final states in the Alpgen photon+jet MC sample, and open circles are the estimates determined from the likelihood matrix method.

1.6 Systematic uncertainties

This section details the systematic uncertainties considered in this analysis. For the data-driven jet background estimation, described in Section 1.5.3, systematic uncertainties arise in the calculation of rates of photons passing isolation and jets faking isolated photons. For MC, uncertainties on the theoretical cross sections are accounted for, as well as the correction factors applied to yield agreement between MC and data. More detail is given in subsections below. A summary of all systematic uncertainties considered, and their values, is presented in Table 1.8.

Systematic	Value
γ ID	± 3.4%
γ $E_T^{topo\ iso}$ correction	± 0.1%
γ energy scale	± 0.8%
γ energy resolution	± 0.4%
Electron MC scaling factor	± 3.9%
Trigger	± 1%
Luminosity	± 2.8%
PDF sets for MC	± —
γ contamination in data-driven methods, combined	± 23%
Kinematic variable choice in data-driven methods	± 13%

Table 1.8: Systematic uncertainties considered in this analysis. Note: At the time of this writing, the analysis of the full 2012 ATLAS dataset for this search is still subject to approval, and hence some systematic uncertainties are incomplete or are subject to change.

1.6.1 Data-driven uncertainties

The calculation of photon isolation efficiencies and rates of jets faking isolated photons, described in Section 1.5.3.1, relies upon the assumptions that both the tail of the T distribution and the entirety of the L' distribution are primarily composed of jets faking photons. Tests on a MC sample composed of a large number of jets indicate that conservative estimates of the true photon contamination in these distributions in the three regions (denoted $\mathrm{T}\widetilde{\mathrm{I}}$, $\mathrm{L}'\mathrm{I}$, and $\mathrm{L}'\widetilde{\mathrm{I}}$, where I indicates isolated and $\widetilde{\mathrm{I}}$ indicates non-isolated) are 15% for $\mathrm{T}\widetilde{\mathrm{I}}$ and 5% each for $\mathrm{L}'\mathrm{I}$, and $\mathrm{L}'\widetilde{\mathrm{I}}$. To assess the affect of this contamination on the estimate of the 2γ+1j, 1γ+2j, and 3j backgrounds, separate photon isolation efficiencies and jet fake rates are calculated where the percentage of true photons in these three regions is set to these contamination values. For each of these values, the entire jet background estimate, using the likelihood matrix method, is performed, leading to alternate values of the estimate of the 2γ+1j, 1γ+2j, and 3j event yields. These results

Final state	Yield				
	Nominal	$\mathrm{T}\widetilde{\mathrm{I}}$, 15% contam	$\mathrm{L}'\mathrm{I}$, 5% contam	$\mathrm{L}'\widetilde{\mathrm{I}}$, 5% contam	Combined variatio
$\gamma\gamma$j	35.06	36.90	34.85	35.88	0.06
γjj	15.36	15.60	14.14	16.68	0.12
jjj	2.70	2.79	2.36	3.07	0.19

Table 1.9: Estimated event yields in the signal region of three tight, isolated photons for the 2γ+1j, 1γ+2j, and 3j backgrounds combined, for the nominal expectation as well as different values of the fractional contamination of true photons in each of the regions assumed to be primarily jets. The contamination is set to the possible true γ fractions indicated, separately for each of the three regions assumed to be jets, and the event yield estimated.

are shown in Table 1.9. The deviations from the nominal yield (assuming no true photon contamination) are calculated separately and added quadratically, and this value (the final column in Table 1.9) is taken as the systematic uncertainty on the event yield for each of the three data-driven backgrounds.

An additional data-driven uncertainty arises from the choice of kinematic variable used to categorize photons and then to calculate and apply photon isolation efficiencies and rates of jets faking isolated photons. The baseline analysis uses three bins in the $p_T-\eta$ plane, and independent versions using either p_T-dependence only or η-dependence only are conducted as well. The largest deviation of the two alternate methods from the nominal method is taken as an additional source of systematic uncertainty.

1.6.2 Simulation uncertainties

- Photon identification: The uncertainty on the event yield due to systematic uncertainties in the standard photon identification definitions is derived by following the official recommendations of the ATLAS eGamma CP group [45].

- Photon isolation: The analysis supplements the recommended isolation prescription — $E_T^{topo\ iso} < 4$ GeV, with a cone size of $\Delta R < 0.4$ — with an isolation energy correction that is applied to photons with overlapping isolation cones, described in Section 1.4.3. To account for this, an additional systematic uncertainty is assessed for this approach. Signal MC samples of the BSM Higgs decay of $h \rightarrow aa \rightarrow 4\gamma$ are used as an example of a resonance that decays to two photons in events with at least three photons, and which may or may not have other photons found within a given photon isolation cone. Truth information is used to select three-photon events in the analysis signal region that are also truth-isolated, i.e., events where none of the three photons contains another photon of $p_T > 15$ GeV/c within its isolation cone. The effects in the final signal yield of applying or not applying the isolation correction on these events is found to plateau to $\sim$0.1% for $m_a > 10$ GeV/c^2.

- Photon energy scale and resolution: The uncertainty on the event yield due to systematic uncertainties in the photon energy scale and resolution are calculated by adjusting the energies of all photons, according to the photon energy scale uncertainty determined by the ATLAS EGamma CP group [45], and propagating the effects to the final event selection. The individual contributions to the total energy scale and resolution uncertainties can be found in Table 1.10.

- Electron scaling factor: The systematic uncertainty on the scaling factor for electron MC processes, described in Section 1.5.2, is taken to be the statistical uncertainty arising from the calculation. The separate values for each of the kinematic bins are summed quadratically, and this is taken as an additional systematic uncertainty on electron MC.

- Trigger efficiency: In progress; an official study of the `EF_g15vh_loose` trigger chain has not been done, and has been requested. A temporary value of 1% is used here, which is based on a conservative increase of the uncertainty of 0.5% on the `EF_g35_loose_g25_loose` trigger, as indicated in Ref. [46].

- Luminosity: An uncertainty of ±2.8% is assigned to the measurement of the integrated luminosity, in accordance with official ATLAS calculations, found in Ref. [47].

- MC cross sections: Uncertainties on the calculated cross sections for MC background and benchmark signal scenarios can be found in Tables 1.11 through 1.13. (In progess. Note: At the time of this writing, the analysis of the full 2012 ATLAS dataset for this search is still subject to approval, and hence some systematic uncertainties are incomplete or are subject to change.) For the BSM Higgs scenario of $h \to aa \to 4\gamma$ the ATLAS-recommended gluon-gluon fusion Higgs production cross sections [2] are used, and the calculated uncertainties are taken from the same source. For the rare decay of the SM Z boson to 3γ, the ppZ production cross section is used, as calculated by MadGraph.

- PDF sets for MC: In progress. Note: At the time of this writing, the analysis of the full 2012 ATLAS dataset for this search is still subject to approval, and hence some systematic uncertainties are incomplete or are subject to change.

---

[2] https://twiki.cern.ch/twiki/bin/view/LHCPhysics/CERNYellowReportPageAt8TeV

Systematic	Value
ZeeAllUp	0.8%
ZeeAllDown	0.6%
R12StatUp	0.8%
R12StatDown	0.8%
PSStatUp	1.0%
PSStatDown	0.8%
LowPtUp	0.8%
LowPtDown	0.8%
ESMUp	0.2%
ESMDown	0.8%
Combined E Scale	2.2%
Combined E Res.	0.8%

Table 1.10: Individual contributions to the systematic uncertainty on the photon energy scale.

MC process	Generator	Cross section uncertainty
2γ	Pythia 8	± —
3γ	MadGraph 5	± —
4γ	MadGraph 5	± —
Zee	Powheg+Pythia 8	± —
Z+γ	Sherpa	± —
W+γ+Np0	Alpgen+Herwig	± —
W+γ+Np1	Alpgen+Herwig	± —
W+γ+Np2	Alpgen+Herwig	± —

Table 1.11: Systematic uncertainties on MC cross sections for background processes. Note: At the time of this writing, the analysis of the full 2012 ATLAS dataset for this search is still subject to approval, and hence some systematic uncertainties are incomplete or are subject to change.

m_h [GeV/c^2]	ggF cross section uncertainties		
	QCD Scale	PDF+α_s	Overall
125	$^{+7.2\%}_{-7.8\%}$	$^{+7.5\%}_{-6.9\%}$	

Table 1.12: Systematic uncertainties on MC cross sections for Higgs signal processes. Note: At the time of this writing, the analysis of the full 2012 ATLAS dataset for this search is still subject to approval, and hence some systematic uncertainties are incomplete or are subject to change.

MC process	Generator	Cross section uncertainties		
		QCD Scale	PDF+α_s	Overall
Z→ 3γ	MadGraph5	—	—	± —

Table 1.13: Systematic uncertainties on MC cross sections for other signal processes. Note: At the time of this writing, the analysis of the full 2012 ATLAS dataset for this search is still subject to approval, and hence some systematic uncertainties are incomplete or are subject to change.

1.7 Results

1.7.1 Expected and observed event yields

Figures 1.28 through 1.34 show the results in signal and control regions defined by the photon ID combination and passed-or-failed isolation combination of events with three photon candidates, using photon isolation efficiencies and jet fake rates calculated for three regions in the $p_T - \eta$ plane. The observed yields in 10% of 8 TeV data are shown as points, and the expectation from backgrounds, which is a combination of the data-driven LMM and MC samples, are shown as stacked histograms. The same information is presented in Tables 1.14 and 1.15. (Note: At the time of this writing, the analysis of the full 2012 ATLAS dataset for this search is still subject to approval, and is blinded. Results are thus shown here for the 10% of the 2012 dataset that has been unblinding to develop and validate the analysis procedures.)

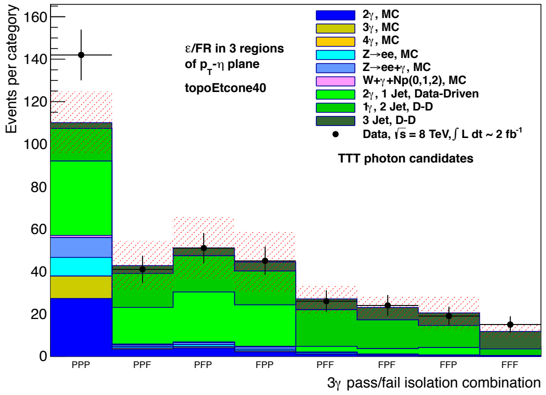

Figure 1.28: Observed and expected yields in events with three photons, where photon isolation efficiencies and jet fake rates are calculated in three regions of the $p_T - \eta$ plane, and have been used for the data-driven jet background estimate, using $E_T^{topo\ iso}$ as the isolation variable, TTT region. The red cross-hatched band is the combined statistical uncertainty of the data-driven jet background estimate and the MC in the stack. As a result of the data-driven jet background estimate, the uncertainty in each bin is partially correlated with the uncertainty on the data in that bin.

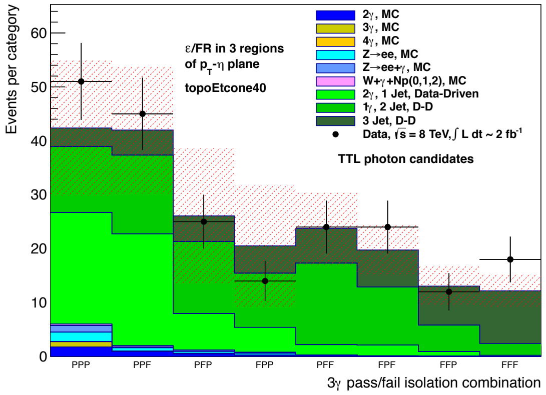

Figure 1.29: Observed and expected yields in events with three photons, where photon isolation efficiencies and jet fake rates are calculated in three regions of the $p_T - \eta$ plane, and have been used for the data-driven jet background estimate, using $E_T^{topo\ iso}$ as the isolation variable, TTL′ region. The red cross-hatched band is the combined statistical uncertainty of the data-driven jet background estimate and the MC in the stack. As a result of the data-driven jet background estimate, the uncertainty in each bin is partially correlated with the uncertainty on the data in that bin.

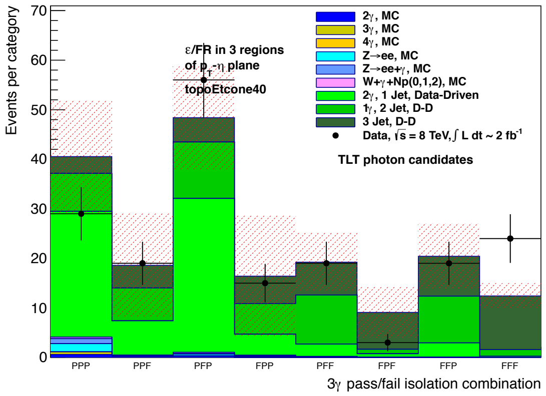

Figure 1.30: Observed and expected yields in events with three photons, where photon isolation efficiencies and jet fake rates are calculated in three regions of the $p_T - \eta$ plane, and have been used for the data-driven jet background estimate, using $E_T^{topo\ iso}$ as the isolation variable, TL′T region. The red cross-hatched band is the combined statistical uncertainty of the data-driven jet background estimate and the MC in the stack. As a result of the data-driven jet background estimate, the uncertainty in each bin is partially correlated with the uncertainty on the data in that bin.

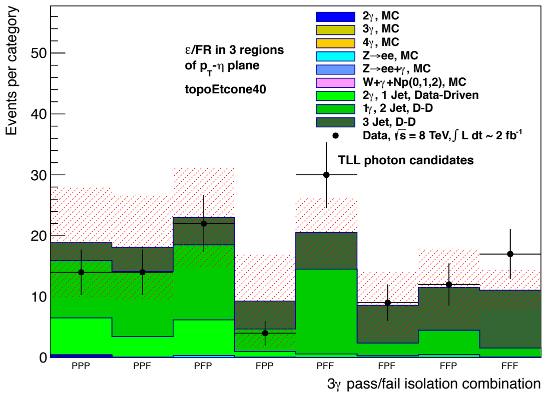

Figure 1.31: Observed and expected yields in events with three photons, where photon isolation efficiencies and jet fake rates are calculated in three regions of the $p_T - \eta$ plane, and have been used for the data-driven jet background estimate, using $E_T^{topo\ iso}$ as the isolation variable, TL′L′ region region. The red cross-hatched band is the combined statistical uncertainty of the data-driven jet background estimate and the MC in the stack. As a result of the data-driven jet background estimate, the uncertainty in each bin is partially correlated with the uncertainty on the data in that bin.

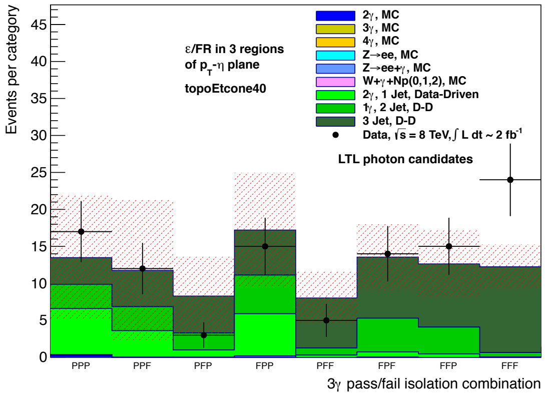

Figure 1.32: Observed and expected yields in events with three photons, where photon isolation efficiencies and jet fake rates are calculated in three regions of the $p_T - \eta$ plane, and have been used for the data-driven jet background estimate, using $E_T^{topo\ iso}$ as the isolation variable, L′TL′ region. The red cross-hatched band is the combined statistical uncertainty of the data-driven jet background estimate and the MC in the stack. As a result of the data-driven jet background estimate, the uncertainty in each bin is partially correlated with the uncertainty on the data in that bin.

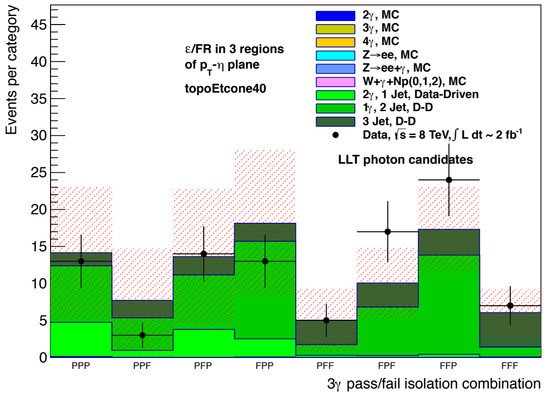

Figure 1.33: Observed and expected yields in events with three photons, where photon isolation efficiencies and jet fake rates are calculated in three regions of the $p_T - \eta$ plane, and have been used for the data-driven jet background estimate, using $E_T^{topo\ iso}$ as the isolation variable, L′L′T region. The red cross-hatched band is the combined statistical uncertainty of the data-driven jet background estimate and the MC in the stack. As a result of the data-driven jet background estimate, the uncertainty in each bin is partially correlated with the uncertainty on the data in that bin.

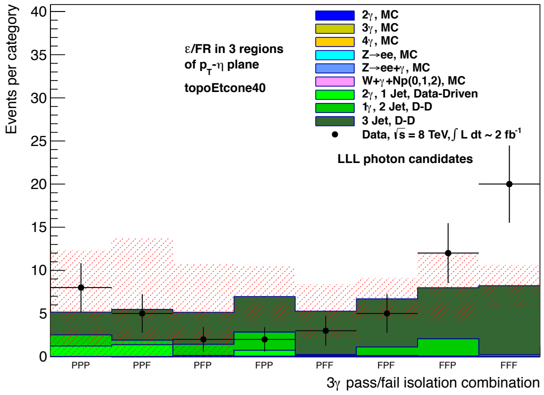

Figure 1.34: Observed and expected yields in events with three photons, where photon isolation efficiencies and jet fake rates are calculated in three regions of the $p_T - \eta$ plane, and have been used for the data-driven jet background estimate, using $E_T^{topo\ iso}$ as the isolation variable, L′L′L′ region. The red cross-hatched band is the combined statistical uncertainty of the data-driven jet background estimate and the MC in the stack. As a result of the data-driven jet background estimate, the uncertainty in each bin is partially correlated with the uncertainty on the data in that bin.

Background	TTT	TTL′	TL′T	TL′L′
2γ (MC)	27.06 ± 2.51	1.91 ± 0.65	0.59 ± 0.38	0.21 ± 0.21
3γ (MC)	10.62 ± 0.13	0.97 ± 0.04	0.54 ± 0.03	0.07 ± 0.01
4γ (MC)	0.06 ± 0.00	0.00 ± 0.00	0.00 ± 0.00	0.00 ± 0.00
2γ,1j (D-D)	35.06 ± 13.64	20.67 ± 11.68	25.38 ± 10.39	6.05 ± 7.93
1γ,2j (D-D)	15.36 ± 4.31	12.23 ± 4.01	7.66 ± 4.41	9.38 ± 4.24
3j (D-D)	2.70 ± 0.81	3.45 ± 1.06	3.40 ± 0.74	2.98 ± 1.17
Zee (MC)	8.75 ± 1.59	1.77 ± 0.70	1.65 ± 0.68	0.00 ± 0.00
Z+γ (MC)	9.13 ± 0.48	1.21 ± 0.18	1.00 ± 0.16	0.14 ± 0.06
W+γ+Np(0,1,2) (MC)	1.02 ± 0.11	0.29 ± 0.06	0.32 ± 0.06	0.03 ± 0.02
Total SM exp.	109.76 ± 14.64	42.52 ± 12.44	40.54 ± 11.34	18.87 ± 9.07
Observed 8 TeV (2 fb^{-1})	142	51	29	14

Table 1.14: Expected and observed event yields in signal and control regions defined in the text, for 10% of 8 TeV data. The three photon candidates are ordered by p_T, from highest to lowest, and photon isolation efficiencies and jet fake rates are calculated in three regions of the $p_T - \eta$ plane, and are used for the γ+j and all-jet background estimates, using $E_T^{topo\ iso}$ as the isolation variable. Background expectations taken from Monte Carlo simulations (data-driven calculations) are marked MC (D-D). Uncertainties are statistical only.

Background	L′TL′	L′L′T	L′L′L′
2γ (MC)	0.22 ± 0.22	0.00 ± 0.00	0.00 ± 0.00
3γ (MC)	0.03 ± 0.01	0.03 ± 0.01	0.01 ± 0.00
4γ (MC)	0.00 ± 0.00	0.00 ± 0.00	0.00 ± 0.00
2γ,1j (D-D)	5.43 ± 7.78	3.56 ± 8.22	1.23 ± 4.24
1γ,2j (D-D)	3.43 ± 2.59	5.99 ± 4.14	1.29 ± 1.24
3j (D-D)	3.68 ± 0.73	2.86 ± 1.17	2.75 ± 0.59
Zee (MC)	0.00 ± 0.00	0.00 ± 0.00	0.00 ± 0.00
Z+γ (MC)	0.12 ± 0.06	0.02 ± 0.01	0.00 ± 0.00
W+γ+Np(0,1,2) (MC)	0.03 ± 0.02	0.06 ± 0.03	0.00 ± 0.00
Total SM exp.	12.94 ± 8.23	12.52 ± 9.27	5.28 ± 4.46
Observed 8 TeV (2 fb^{-1})	17	12	7

Table 1.15: Expected and observed event yields in signal and control regions defined in the text, for 10% of 8 TeV data, continued. The three photon candidates are ordered by p_T, from highest to lowest, and photon isolation efficiencies and jet fake rates are calculated in three regions of the $p_T - \eta$ plane, and are used for the γ+j and all-jet background estimates, using $E_T^{topo\ iso}$ as the isolation variable. Background expectations taken from Monte Carlo simulations (data-driven calculations) are marked MC (D-D). Uncertainties are statistical only.

$h \to aa \to 4\gamma$ m_a (GeV/c^2)	TTT	TTL$'$	TL$'$T	TL$'$L$'$
1	0.00 ± 0.00	0.00 ± 0.00	0.00 ± 0.00	0.00 ± 0.00
5	28.74 ± 1.98	0.06 ± 0.06	0.72 ± 0.29	0.00 ± 0.00
7	166.58 ± 4.80	2.74 ± 0.63	3.02 ± 0.65	0.00 ± 0.00
10	405.94 ± 7.56	10.12 ± 1.16	11.95 ± 1.29	0.52 ± 0.27
15	545.28 ± 8.73	50.28 ± 2.66	33.36 ± 2.18	5.03 ± 0.86
20	583.48 ± 9.03	59.67 ± 2.88	33.50 ± 2.18	3.95 ± 0.75
30	578.21 ± 8.99	63.55 ± 3.00	38.02 ± 2.31	4.70 ± 0.84
40	603.91 ± 9.18	58.59 ± 2.86	39.15 ± 2.32	3.71 ± 0.71
50	722.12 ± 10.03	72.09 ± 3.22	49.35 ± 2.64	5.50 ± 0.85
60	974.62 ± 11.68	94.03 ± 3.62	63.15 ± 3.00	8.12 ± 1.09
62	1011.59 ± 11.91	92.47 ± 3.60	63.59 ± 3.01	7.98 ± 1.09

Table 1.16: Event yields in signal and control regions defined in the text, for the benchmark BSM scenario of a Higgs decaying to four photons, using $E_T^{topo\ iso}$ as the isolation variable. The three photon candidates are ordered by p_T, highest to lowest. Events have been weighted to correspond to expectations in 10% of 8 TeV data, for the gluon fusion Higgs production cross section and a branching ratio of $h \to aa$ of 0.1. Uncertainties are statistical only.

$h \to aa \to 4\gamma$ m_a (GeV/c^2)	L$'$TL$'$	L$'$L$'$T	L$'$L$'$L$'$
1	0.00 ± 0.00	0.00 ± 0.00	0.00 ± 0.00
5	0.00 ± 0.00	0.00 ± 0.00	0.00 ± 0.00
7	0.00 ± 0.00	0.00 ± 0.00	0.00 ± 0.00
10	0.14 ± 0.14	0.24 ± 0.17	0.00 ± 0.00
15	2.28 ± 0.57	1.12 ± 0.38	0.27 ± 0.16
20	2.22 ± 0.57	1.20 ± 0.42	0.52 ± 0.26
30	1.91 ± 0.50	2.40 ± 0.57	0.52 ± 0.26
40	2.54 ± 0.57	2.65 ± 0.63	0.69 ± 0.31
50	4.63 ± 0.81	2.42 ± 0.57	0.31 ± 0.19
60	5.25 ± 0.84	5.02 ± 0.84	1.00 ± 0.36
62	5.04 ± 0.83	4.62 ± 0.79	0.54 ± 0.28

Table 1.17: Event yields in signal and control regions defined in the text, for the benchmark BSM scenario of a Higgs decaying to four photons, using $E_T^{topo\ iso}$ as the isolation variable, continued. The three photon candidates are ordered by p_T, highest to lowest. Events have been weighted to correspond to expectations in 10% of 8 TeV data, for the gluon fusion Higgs production cross section and a branching ratio of $h \to aa$ of 0.1. Uncertainties are statistical only.

1.7.2 Limits on fiducial cross section for events from non-SM processes

For 10% of 2012 data, the total background expectation (from a combination of MC and data-driven jet background estimates) is 109.76 ± 18.22 (stat. and syst.) and the observed event yield is 142 (as shown in Table 1.14). This corresponds to a p-value of 0.095 with an equivalent significance, in units of Gaussian σ, of 1.31.

1.7.3 Search for local excesses in two-photon and three-photon invariant mass distributions

Additionally, searches for local excesses in the two-photon and three-photon invariant mass distributions are performed. The following is a determination of expected limits for the full 2012 dataset derived from 10% of that data (see the discussion in Section 1.7.1). For the purposes of projected expected limits, using a small subset of data, the two-photon distribution presented here is for $m_{\gamma_2\gamma_3}$, that is, photons 2 and 3 of the three p_T-ordered photons in events in the signal region. Based on studies of signal MC, the 2-3 pairing is the most frequently correct pairing, occurring roughly 50% of the time across the full m_a spectrum. The expected upper limits quoted have then been scaled to take into account this 0.5 efficiency for choosing $m_{\gamma_2\gamma_3}$. Figures 1.35 and 1.36 show the two- and three-photon invariant mass distributions, respectively, for events in the signal region, for ~2 fb^{-1} of 2012 data. Also shown are the results of fitting a function to the data. The function fit is the product of a Rayleigh function, given by

$$f_{\mathrm{Rayleigh}} = \frac{x}{\sigma^2} e^{-x^2/2\sigma^2}, \tag{1.9}$$

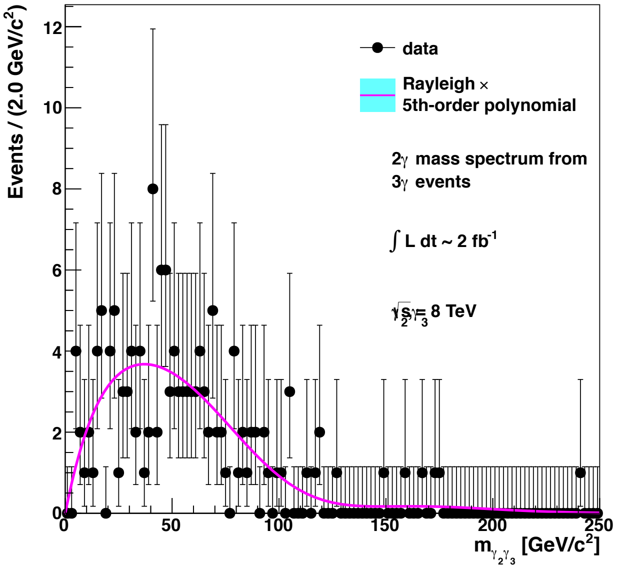

Figure 1.35: Distribution of $m_{\gamma_2\gamma_3}$ for events in the signal region, for ~2 fb^{-1} of 2012 data.

and a 5th-order Bernstein polynomial.

The fitted function is then used to generate an ideal dataset with statistics equal to the total number of events expected in the signal region in the full 2012 dataset, i.e., the integral of the ~2 fb^{-1} dataset multiplied by 10. These ideal datasets, for the two- and three-photon invariant mass spectra, with 2 GeV/c^2 binning, are shown in Figures 1.37 and 1.38, respectively.

Expected upper limits on the cross section for new particles that decay to two or three photons in three-photon events are calculated by performing a resonance search in these ideal invariant mass spectra. The search is performed along the full mass spectrum, in steps of 2 GeV/c^2 with a window size of 40 GeV/c^2, using a Gaussian function for the signal, for fixed Gaussian widths of 2, 3, and 4 GeV/c^2. For a given mass hypothesis, an upper limit, at the 95% confidence level, on the number of signal events, N_{sig}, is determined via a hypothesis test, using the profile

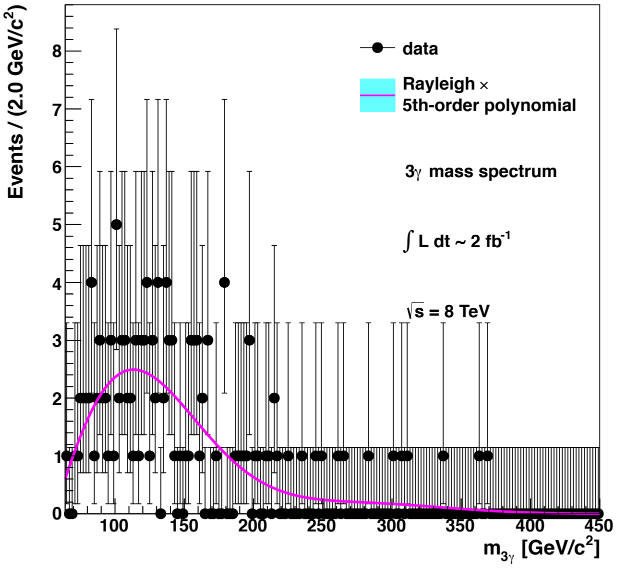

Figure 1.36: Distribution of $m_{3\gamma}$ for events in the signal region, for ~2 fb^{-1} of 2012 data.

likelihood ratio [48] as the basis for the test statistic. $N_{sig,UL}$ is then used to compute an upper limit on $\sigma \times \mathcal{A}$ for new particles, as a function of particle mass.

Additionally, utilizing the fiducial efficiencies for resonances shown in Figure 1.47, upper limits on the fiducial cross section for resonances that decay to two photons in three-photon events are computed, and the results are shown in Figure 1.41.

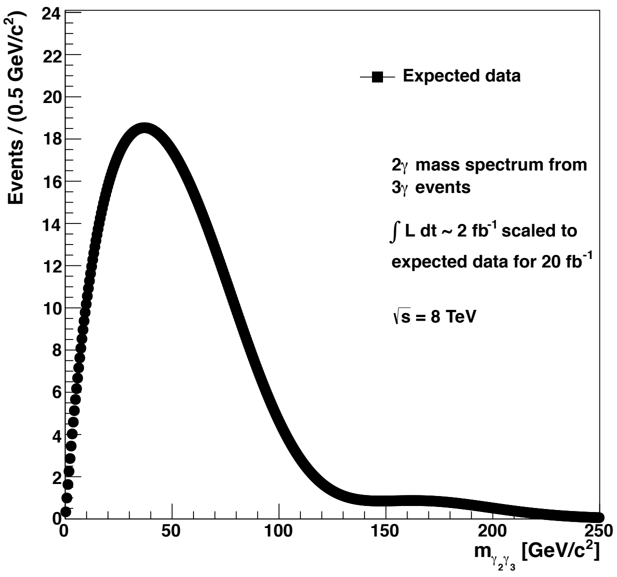

Figure 1.37: An ideal spectrum of $m_{\gamma_2\gamma_3}$ with statistics equal to the total number of events expected in the signal region in the full 2012 dataset, i.e., the integral of the ∼2 fb^{-1} dataset multiplied by 10. The dataset has been generated from a function (also shown) fit to the distribution of $m_{\gamma_2\gamma_3}$ for events in the signal region, for ∼2 fb^{-1} of 2012 data.

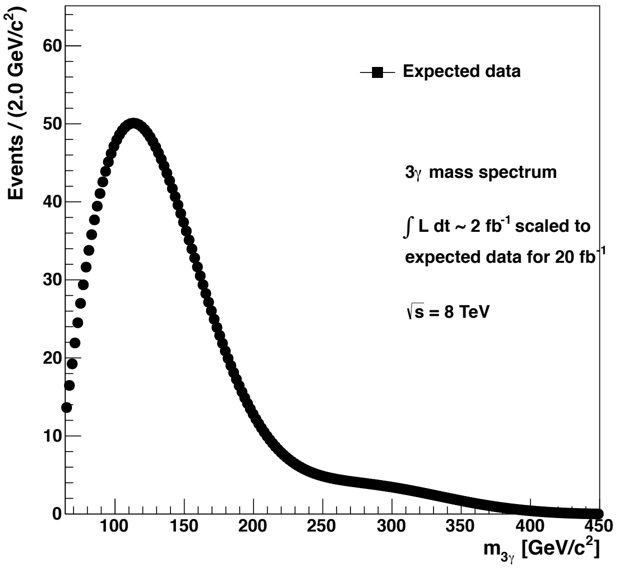

Figure 1.38: An ideal spectrum of $m_{3\gamma}$ with statistics equal to the total number of events expected in the signal region in the full 2012 dataset, i.e., the integral of the $\sim$2 fb^{-1} dataset multiplied by 10. The dataset has been generated from a function (also shown) fit to the distribution of $m_{3\gamma}$ for events in the signal region, for $\sim$2 fb^{-1} of 2012 data.

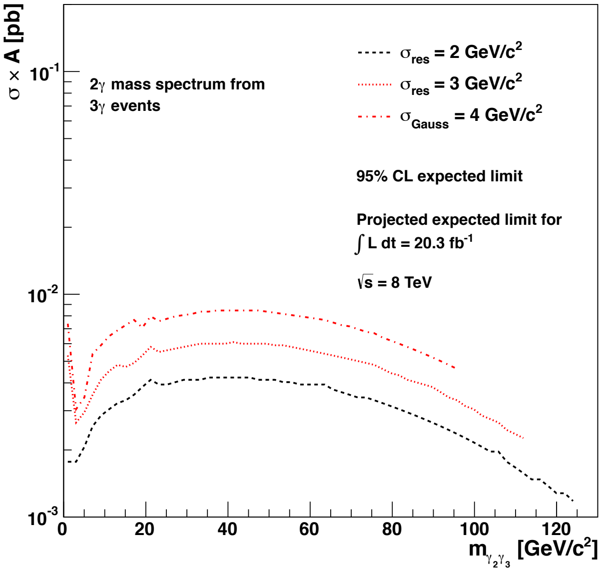

Figure 1.39: Expected upper limits on the cross section (σ) times acceptance (A) for new particles that decay to two photons in three-photon events, using a Gaussian resonance hypothesis, for Gaussian widths of 2, 3, and 4 GeV/c^2. The expected limits have been derived starting from a fit to the $m_{2\gamma}$ spectrum for events in the signal region, for $\sim$2 fb^{-1} of 2012 data, which is then used to generated an invariant mass spectrum with statistics equal to the total number of events expected in the full 2012 dataset, i.e., the integral of the $\sim$2 fb^{-1} dataset multiplied by 10.

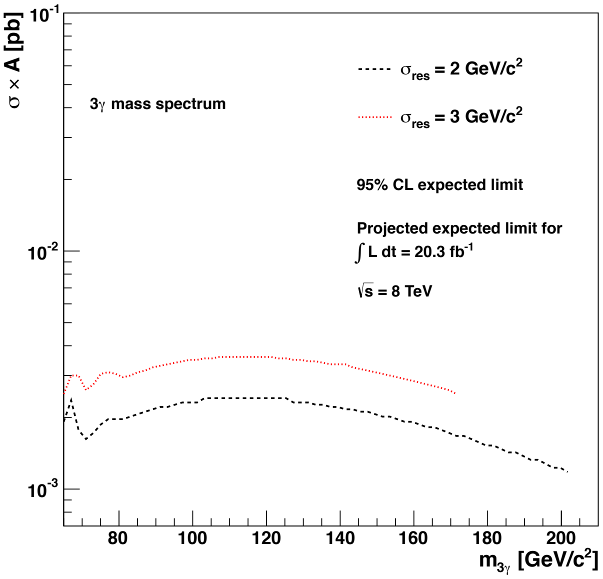

Figure 1.40: Expected upper limits on the cross section (σ) times acceptance (A) for new particles that decay to three photons in three-photon events, using a Gaussian resonance hypothesis, for Gaussian widths of 2 and 3 GeV/c^2. The expected limits have been derived starting from a fit to the $m_{3\gamma}$ spectrum for events in the signal region, for ∼2 fb^{-1} of 2012 data, which is then used to generated an invariant mass spectrum with statistics equal to the total number of events expected in the full 2012 dataset, i.e., the integral of the ∼2 fb^{-1} dataset multiplied by 10.

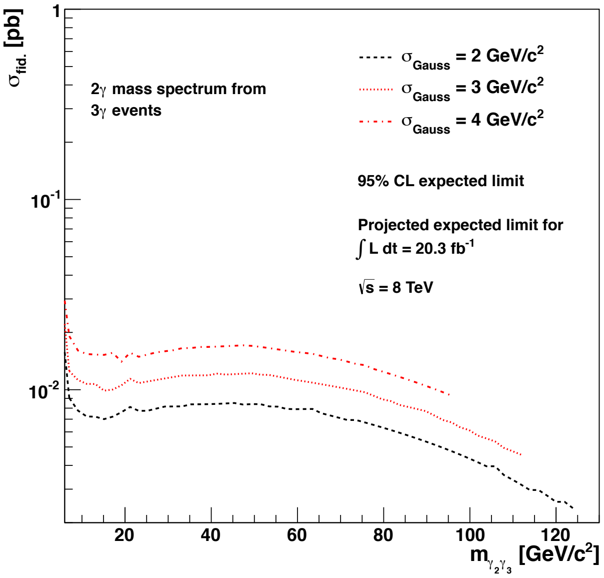

Figure 1.41: Expected upper limits on the fiducial cross section ($\sigma_{fid.}$) for new particles that decay to two photons in three-photon events, using a Gaussian resonance hypothesis, for Gaussian widths of 2, 3, and 4 GeV/c^2. The expected limits have been derived starting from a fit to the $m_{2\gamma}$ spectrum for events in the signal region, for ~2 fb^{-1} of 2012 data, which is then used to generated an invariant mass spectrum with statistics equal to the total number of events expected in the full 2012 dataset, i.e., the integral of the ~2 fb^{-1} dataset multiplied by 10.

1.8 Interpretations

1.8.1 Exotic Higgs decays

The results of the search are interpreted in a BSM scenario where a Higgs boson decays into four photons via two intermediate pseudoscalar (a) particles. As mentioned previously, MC simulations of these events are performed with POWHEG-BOX+PYTHIA 8.163, for eleven m_a points from 1 GeV/c^2 to 62 GeV/c^2.

Figures 1.42 and 1.43 show the ΔR and p_T distributions, respectively, for the three highest-p_T photon candidates in signal events. The ΔR distributions are shown for the pairings of photons 1 and 3, and 2 and 3, where the photons have passed T ID. The signal efficiency with respect to the event selection criteria outlined previously, for three tight, isolated photons, as a function of m_a, is shown in Figure 1.44, and the same information appears in Table 1.18. The decrease in efficiency for low m_a values is primarily due to photons close together in ΔR, which leads to at least one of the photons failing either isolation or T identification. For $m_a < 20$ GeV/c^2, the photons frequently overlap within the cone of ΔR = 0.4, thus leading to at least one of the photons failing the isolation criterion. To mitigate this loss of signal efficiency and to recover cone-overlapping photons that fail isolation (as discussed in Section 1.4.3), an overlap correction to $E_T^{topo\ iso}$ is applied to all selected photon candidates, which results in the increase in signal efficiency shown in Figure 1.45.

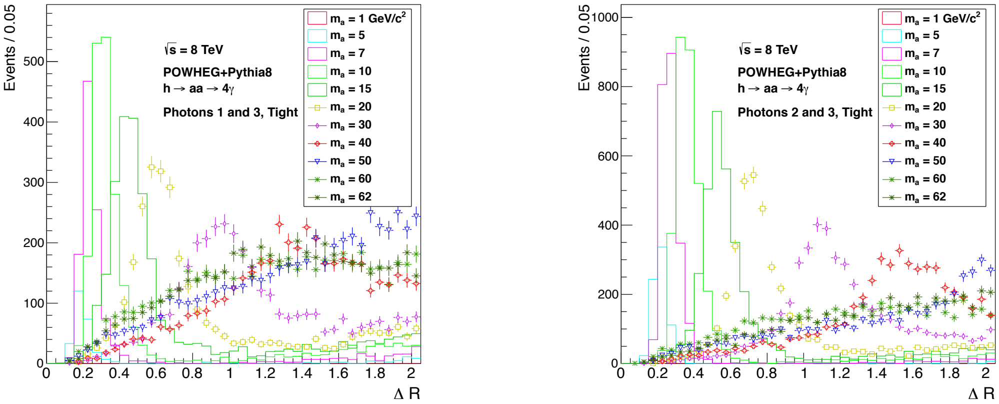

Figure 1.42: Distance in ΔR between reconstructed, p_T-ordered photon candidates 1 and 3, and 2 and 3, that have passed T ID, for the exotic Higgs decay scenario for events with three tight photons, with no requirement on $E_T^{topo\ iso}$.

$h \to aa \to 4\gamma$ m_a (GeV/c^2)	3γ Overall Efficiency	3γ Fiducial Efficiency
1	0.000	0.000
5	0.007	0.053
7	0.043	0.217
10	0.104	0.368
15	0.139	0.472
20	0.149	0.507
30	0.148	0.504
40	0.154	0.501
50	0.184	0.486
60	0.249	0.490
62	0.258	0.489

Table 1.18: Signal efficiency for events with three tight, isolated photons, overall and for a fiducial region defined in the text, for the benchmark BSM scenario of a Higgs decaying to four photons.

To test the dependence of signal efficiency on overlapping photons failing T ID, a fiducial region is defined. Using truth information in MC, events with three photon candidates are tested as follows, in order:

- η: All three photons appear in good regions of the detector, satisfying $|\eta| < 1.37$ or > 1.52, and also $|\eta| < 2.37$.
- p_T: All three photons, ordered from highest to lowest p_T, must satisfy $p_T >$ 22, 22, and 17 GeV/c.
- Isolation: All three photons must satisfy $E_T^{truth\ iso} < 4$ GeV, where $E_T^{truth\ iso}$ is calculated by summing the E_T values of all truth particles (except muons and neutrinos) within a cone of $\Delta R = 0.4$ around the photon, excluding the energy of the photon itself and excluding other photons with $p_T > 15$ GeV/c, to match the requirements of the $E_T^{topo\ iso}$ overlap correction applied

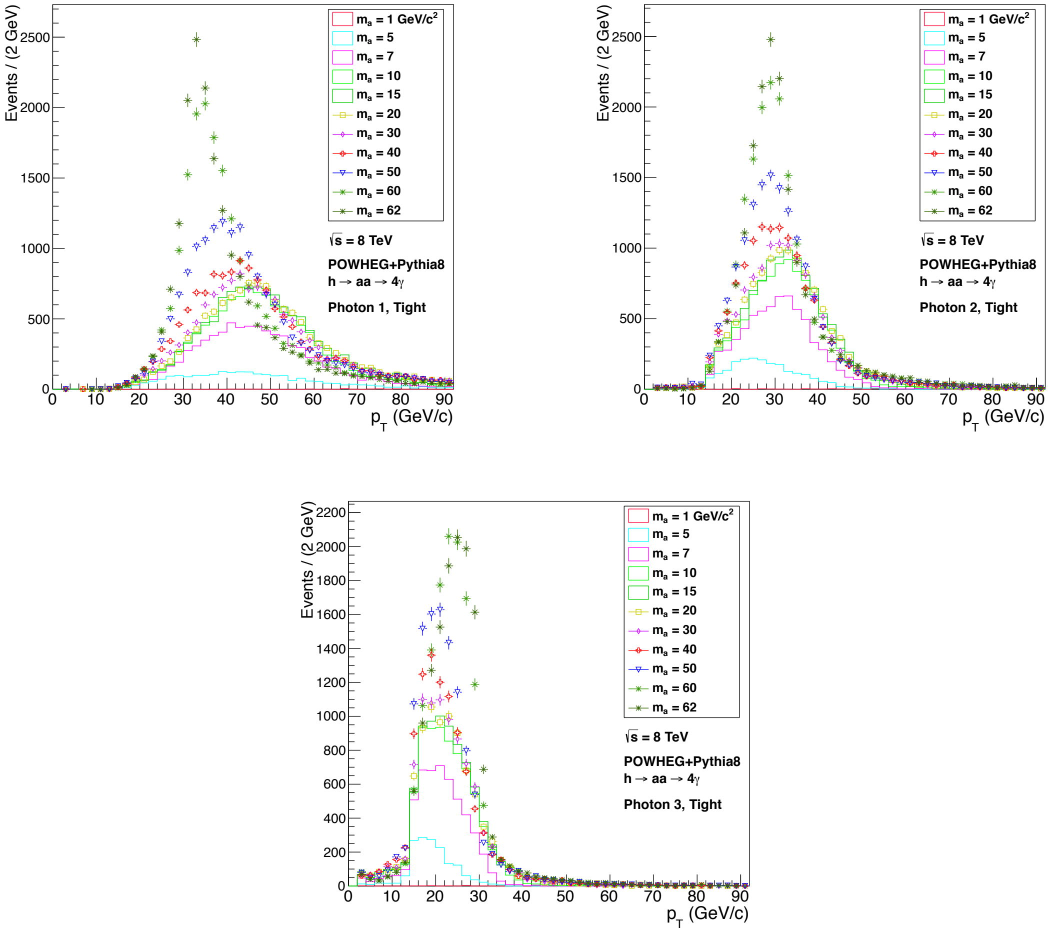

Figure 1.43: Distributions of reconstructed photon p_T for the benchmark Higgs scenario for photons that pass tight (T) ID, for the three highest-p_T photons separately.

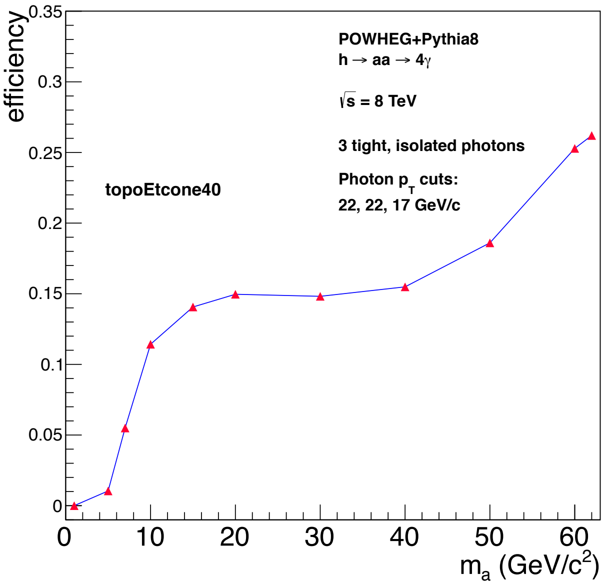

Figure 1.44: Signal efficiency for a BSM scenario with a Higgs boson decaying via intermediate pseudoscalars (a) into four photons, as a function of m_a.

to reconstructed photons.

The fiducial efficiency is then the ratio of the number of reconstructed signal events passing the analysis cuts to the number of truth events falling into this fiducial region. The fiducial efficiency, shown in Figure 1.47 as a function of m_a, is demonstrated to plateau for $m_a > 10$ GeV/c^2. The cut flow for the fiducial region is shown in Figure 1.46, and both the overall signal efficiencies and the fiducial efficiencies appear in Table 1.18.

Expected upper limits on the product of branching ratios, $BR(h \to aa) \times BR(a \to \gamma\gamma)^2$, for this BSM Higgs decay are calculated as a function of m_a following the resonance search procedure described in Section 1.7.3, but here for local resonances with widths equal to those determined via independent fits to the signal MC samples, and taking into about the signal efficiency shown in Figure 1.44.

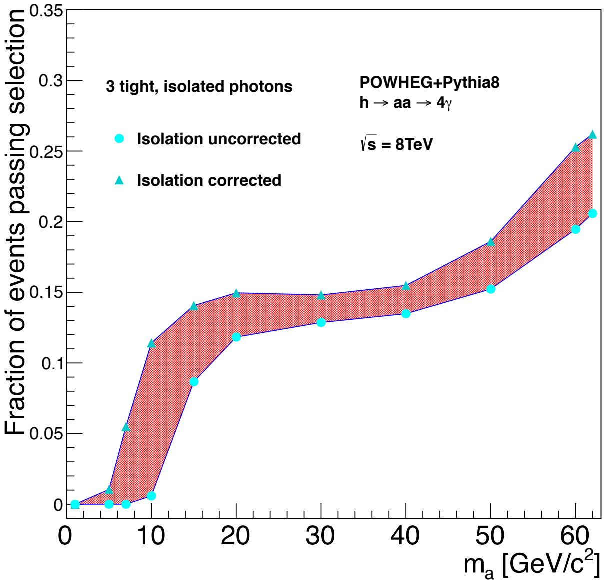

Figure 1.45: Signal efficiency for a BSM scenario with a Higgs boson decaying via intermediate pseudoscalars (a) into four photons, as a function of m_a. Shown here is efficiency before and after applying the correction to $E_T^{topo\ iso}$ due to overlapping photons.

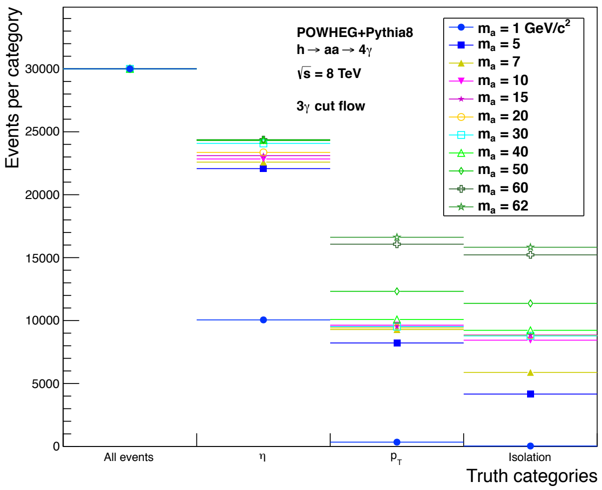

Figure 1.46: Cut flow for a fiducial kinematic region, using truth MC information, defined as the set of events that contain three photons that 1) are in the good detector volume, 2) satisfy $p_T > 22$, 22, and 17 GeV/c, and 3) satisfy $E_T^{truth\ iso} < 4$ GeV, for a BSM scenario with a Higgs boson decaying via intermediate pseudoscalars (a) into four photons, for several values of m_a.

The resulting expected upper limits on $BR(h \to aa) \times BR(a \to \gamma\gamma)^2$ are shown in Figure 1.50.

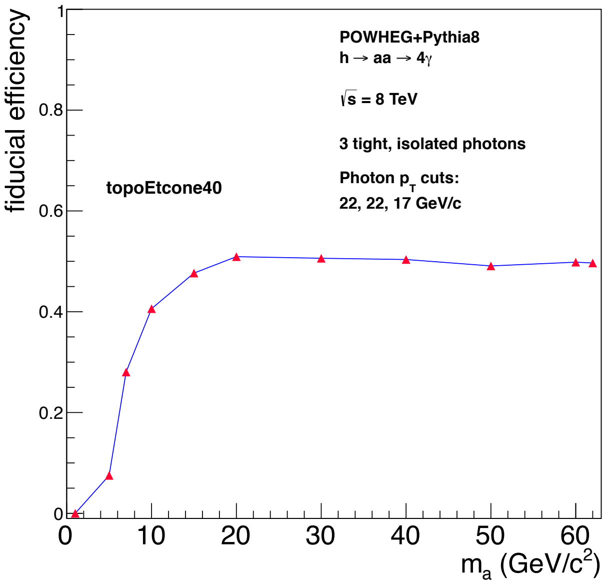

Figure 1.47: Signal efficiency for a fiducial kinematic region, using truth information, defined as the set of events that contain three photons that 1) are in the good detector volume, 2) satisfy $p_T > 22$, 22, and 17 GeV/c, and 3) satisfy $E_T^{truth\ iso} <$ 4 GeV, for a BSM scenario with a Higgs boson decaying via intermediate pseudoscalars (a) into four photons, as a function of m_a.

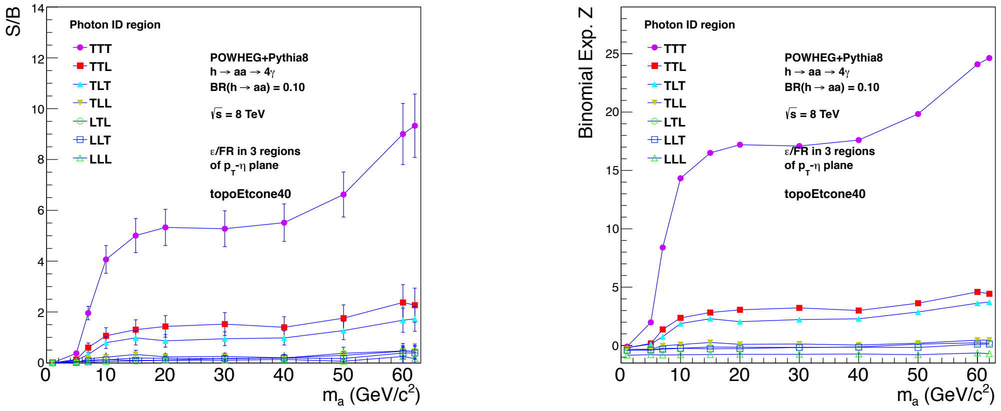

Figure 1.48: Left: Ratio of signal yield to background expectation in signal and control regions for a BSM scenario with a Higgs boson decaying via intermediate pseudoscalars (a) into four photons, for a branching ratio of $h \rightarrow aa$ of 0.1, as a function of m_a, in final states where only three good, reconstructed photons that pass isolation are required. The filled circles are for the signal region, where all three photons satisfy T photon ID. The other points correspond to control regions where one or more of the photons fails T. Right: Expected significance, in units of Gaussian sigma, that takes into account the fractional background uncertainty (here statistical only) on the background expectation. The significance is calculated from the expected p-value for the $N^{signal}_{events} = 0$ hypothesis, given the expected signal and background yields, and the background uncertainty.

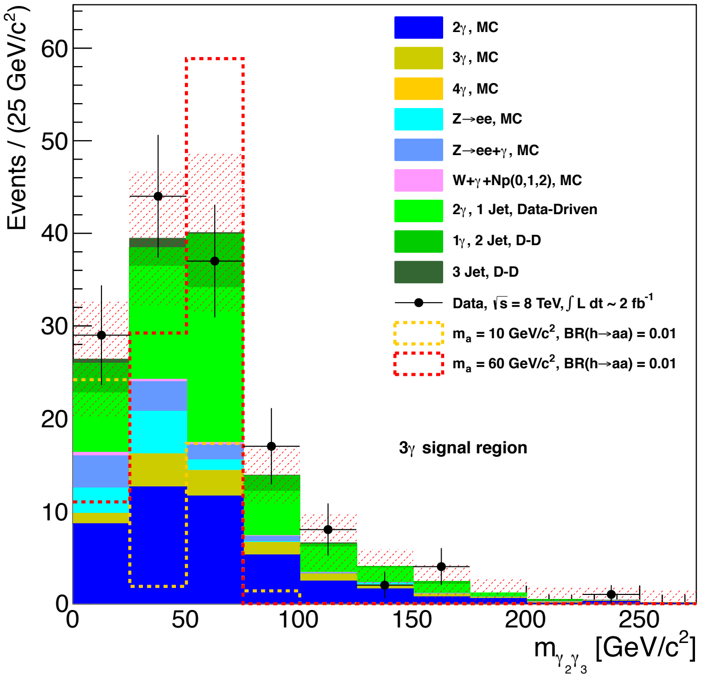

Figure 1.49: Comparison of observed data and background expectation (both MC and data-driven) as a function of $m_{\gamma_2\gamma_3}$. Also shown is the MC expectation for the BSM scenario with a Higgs boson decaying via intermediate pseudoscalars (a) into four photons, for a branching ratio of $h \to aa$ of 0.01.

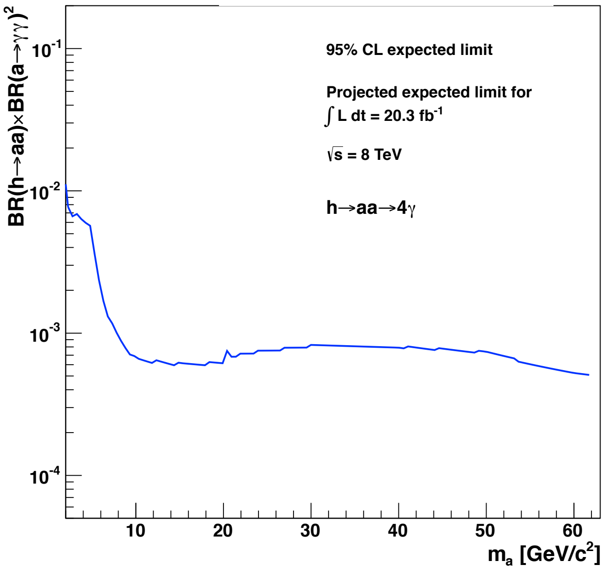

Figure 1.50: Expected upper limits on $BR(h \to aa) \times BR(a \to \gamma\gamma)^2$ for the decay $h \to aa \to 4\gamma$, using resonance hypotheses determined via fits to signal MC, and taking into account the signal efficiency. The expected limits have been derived starting from a fit to the $m_{2\gamma}$ spectrum for events in the signal region, for ~2 fb^{-1} of 2012 data, which is then used to generated an invariant mass spectrum with statistics equal to the total number of events expected in the full 2012 dataset, i.e., the integral of the ~2 fb^{-1} dataset multiplied by 10.

1.8.2 Rare SM Z decay: Z $\rightarrow 3\gamma$

The SM Z boson can decay to three photons via a loop of $W^{+/-}$ bosons or fermions. The decay is heavily suppressed and the branching ratio is predicted to be $\sim 5 \times 10^{-10}$ [24]. The $Z\gamma\gamma\gamma$ effective vertex has been implemented with FeynRules, and then output to a customized MadGraph 5 model. The two nontrivial, independent, lowest-order effective Lagrangians implemented are shown in Eqs. 1.10 and 1.11 (from Ref. [49]), each of which contains a dimensionful coupling constant, i.e., G_1 and G_2 [GeV^{-4}].

$$\mathcal{L}_1 = G_1 F^{\alpha\mu} F^{\sigma\nu} \partial_\alpha F_{\mu\nu} Z_\sigma \tag{1.10}$$

$$\mathcal{L}_2 = G_2 F^{\alpha\beta} F^{\nu}_{\beta} \partial_\alpha F_{\sigma\nu} Z^\sigma \tag{1.11}$$

Using the SM expected Z $\rightarrow 3\gamma$ branching ratio of 5.41×10^{-10}, the authors in Ref. [50] calculate $G_1 = 1.63\times10^{-10}$ and $G_2 = 1.33\times10^{-10}$, and those values have been used to generate the MC sample presented here. The distribution of the generated Z mass is shown in Figure 1.51, and distributions of the true p_T of the Z (where "true" and "truth", hereafter, refer to the values determined from the MC generator), the truth p_T of the three photons from the Z decay, and he truth η of the three photons are shown in Figures 1.52, 1.53, and 1.54, respectively. Distributions of reconstructed p_T of the leading, sub-leading, and sub-sub-leading photons in fully simulated and reconstructed events, for events in the analysis signal region, are shown in Figure 1.55. The number of events that pass each selection criterion in succession and that thus appear in the analysis signal region, and the resulting signal efficiency, are shown in Table 1.19. Also shown is number

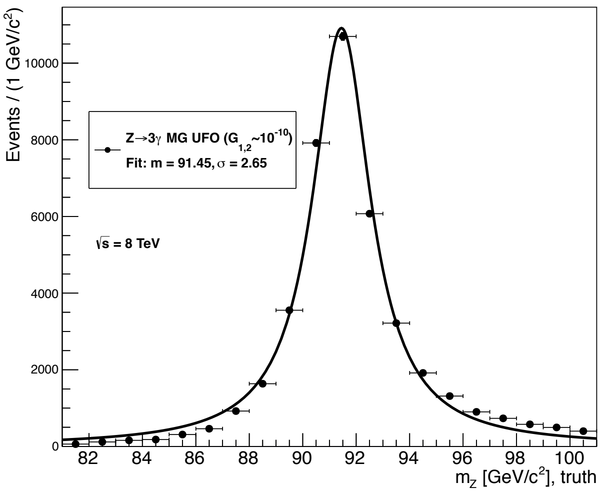

Figure 1.51: Distribution of truth m_Z for the rare decay of the SM $Z \to 3\gamma$, simulated with FeynRules and MadGraph 5.

of events retained and the efficiency for the further requirement of $80 < m_{3\gamma} < 100$ GeV/c^2.

The observed and expected yields in the signal and control regions are shown in Figures 1.58 through 1.64, where analysis has been restricted to those events with $80 < m_{3\gamma} < 100$ GeV/c^2. The full likelihood matrix method, to estimate the contribution from jet backgrounds, has been performed with this further requirement. The same information appears in Tables 1.20 and 1.21.

The differential width for this process, calculated in Ref. [24], is given in terms of two three-dimensional phase space variables as

$$\begin{aligned}\frac{d\Gamma}{dx\,dy} &= \frac{1}{(2\pi)^3}\frac{m_Z^9}{2304}\big\{G_1^2[2xy(1-x-y)+3x^2y^2+3(x^2+y^2)(1-x-y)^2] \\ &\quad +4(G_2^2-G_1G_2)[xy(1-x-y)+x^2y^2+(x^2+y^2)(1-x-y)^2]\big\}\end{aligned} \tag{1.12}$$

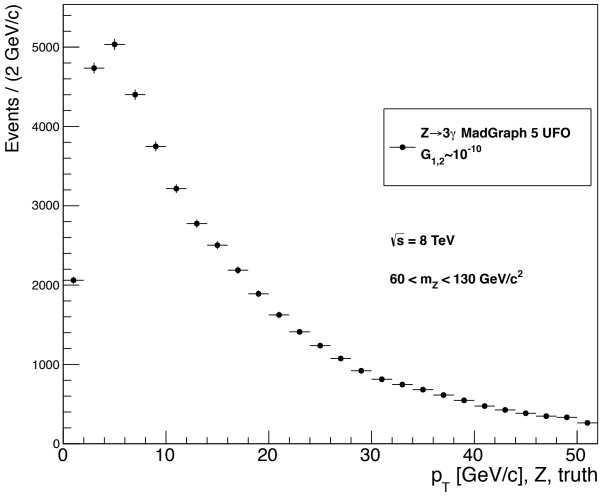

Figure 1.52: Distribution of truth p_T for Z boson in the rare decay of the SM $Z \to 3\gamma$, simulated with FeynRules and MadGraph 5.

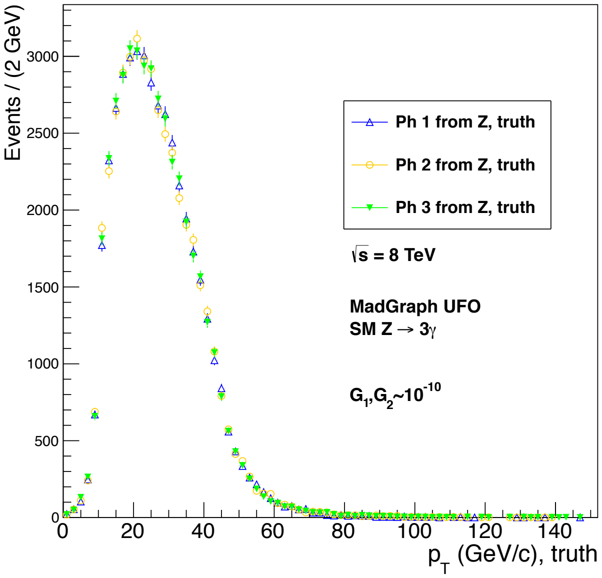

Figure 1.53: Distributions of truth p_T for the three photons from the rare decay of the SM $Z \to 3\gamma$, simulated with FeynRules and MadGraph 5.

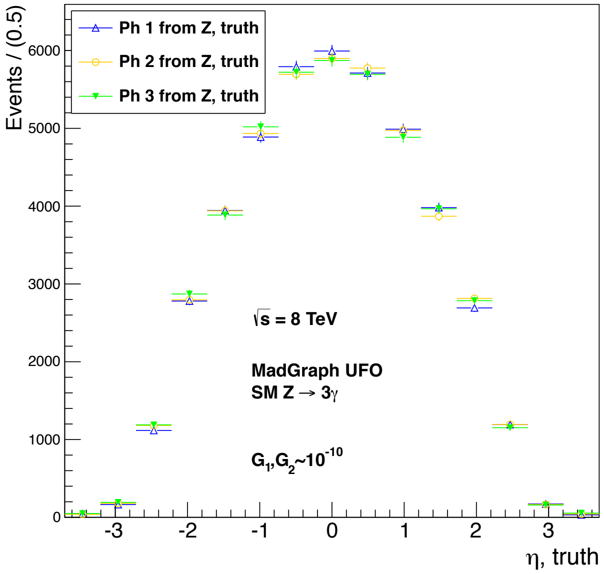

Figure 1.54: Distributions of truth η for the three photons from the rare decay of the SM $Z \to 3\gamma$, simulated with FeynRules and MadGraph 5.

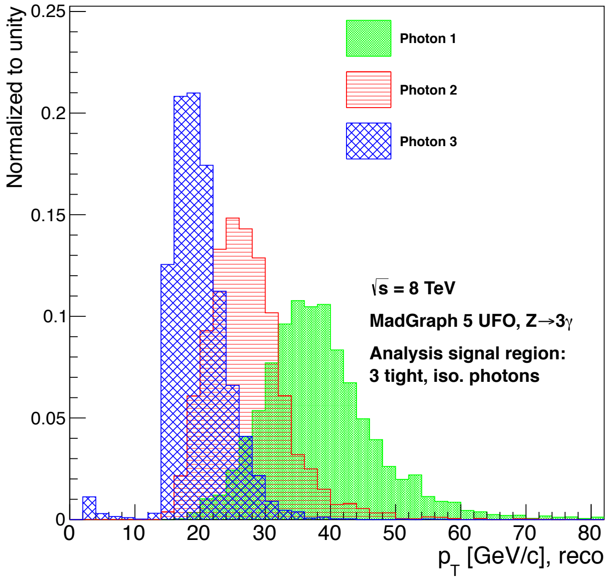

Figure 1.55: Distributions of p_T for the leading, sub-leading, and sub-sub-leading photons in the analysis signal region for the rare decay of the SM Z boson to three photons, simulated with FeynRules and MadGraph 5 and fully reconstructed.

Z$\to$ 3γ MC	N$_{events}$
All events	30000
Trigger	13883
Three good photons	10534
$p_T >$ 22, 22, 17 GeV/c	5928
All three tight	3446
All three isolated	2960
Efficiency	0.099
80 $< m_{3\gamma} <$ 100 GeV/c^2	2367
Efficiency	0.079

Table 1.19: Events passing signal region selection criteria, after event preselection and photon object selection, for the rare decay of the SM Z boson to three photons, simulated with FeynRules and MadGraph 5 and fully reconstructed.

where x and y (and z, which has been integrated over for the previous expression) are scaled photon energies for three photons, given by

$$x = 1 - \frac{2E_1}{m_Z}, \quad y = 1 - \frac{2E_2}{m_Z}, \quad z = 1 - \frac{2E_3}{m_Z}. \tag{1.13}$$

The analytical expression in Equation 1.12 as a function of x and y is shown in the left plot in Figure 1.56, for a fixed value of m_Z = 91.19 GeV/c^2. Additionally, Figure 1.56 displays the same distributions of Equation 1.12 determined from the MC samples generated with the values of the coupling constants set to 1 (middle plot), as well as set to those values mentioned above, $G_1 = 1.63\times10^{-10}$ and $G_2 = 1.33\times10^{-10}$ (right plot). In the MC plots, the values shown are from events where the restriction 90 $< m_{3\gamma} <$ 92 GeV/c^2 has been applied.

The upper limit on $BR(Z \to 3\gamma)$ is determined using the observed and expected yields in the signal region for 10% of 8 TeV data with the restriction 80 $< m_{3\gamma} <$ 100 GeV/c^2. A one-sided frequentist limit approach is used, with the profile likelihood ratio as the basis for the test statistic, taking into account all

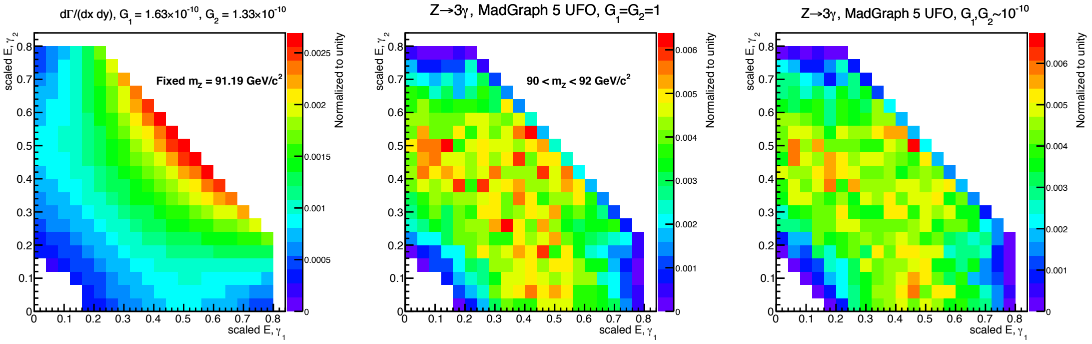

Figure 1.56: Distributions of the differential decay widths, as a function of two variables from three-dimensional phase space, for the rare decay of the SM Z boson to three photons. Left: The analytical expression in Equation 1.12, for a fixed value of m_Z = 91.19 GeV/c^2. Middle: Simulated with FeynRules and MadGraph 5, where the dimensionful coupling constants have been set to $G_1 = G_2 = 1$, restricted to a window of $90 < m_{3\gamma} < 92$ GeV/c^2. Right: Simulated with FeynRules and MadGraph 5, where the dimensionful coupling constants have been set to $G_1 = 1.63\times10^{-10}$ and $G_2 = 1.33\times10^{-10}$, restricted to a window of 90 $< m_{3\gamma} < 92$ GeV/c^2.

systematic uncertainties on the background expectation, separately for each MC and data-driven background estimate. For 10% of the 2012 dataset, the observed upper limit, at the 95% CL, is found to be $BR(Z \to 3\gamma) < 3.09 \times 10^{-6}$.

An expected projected upper limit on $BR(Z \to 3\gamma)$ is determined using the observed and expected yields in the signal region for 10% of 8 TeV data with the restriction $80 < m_{3\gamma} < 100$ GeV/c^2, and then scaling all yields to the expectation for the full 2012 dataset, i.e., multiplying by 10. The expected upper limit is then computed in the same manner as above. Assuming no change in the uncertainty on the background from 10% to the full 2012 dataset, the expected upper limit, at the 95% CL, is found to be $BR(Z \to 3\gamma) \lesssim 1.99 \times 10^{-6}$, which would be the strongest bound on this process.

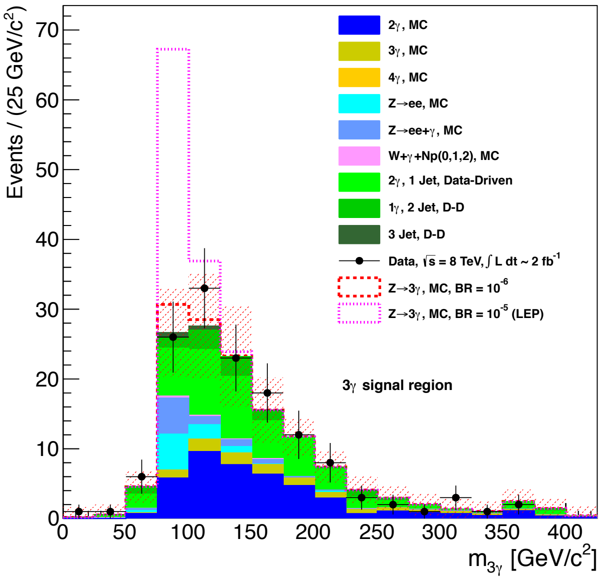

Figure 1.57: Comparison of observed data and background expectation (both MC and data-driven) as a function of $m_{3\gamma}$. Also shown is the expectation for the rare decay of the SM $Z \rightarrow 3\gamma$, simulated with FeynRules and MadGraph 5, which has been added to the full background estimate. The signal MC is shown for two different values of $BR(Z \rightarrow 3\gamma)$, that for the LEP observed limit of 10^{-5} and for 10^{-6}.

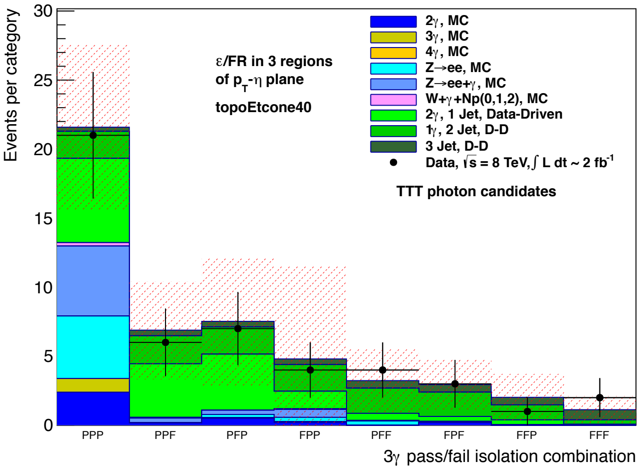

Figure 1.58: Observed and expected yields in events with three photons, where photon isolation efficiencies and jet fake rates are calculated in three regions of the $p_T - \eta$ plane, and have been used for the data-driven jet background estimate, using $E_T^{topo\ iso}$ as the isolation variable, TTT region, restricted to $80 < m_{3\gamma} < 100$ GeV/c^2. The red cross-hatched band is the combined statistical uncertainty of the data-driven jet background estimate and the sum of all MC samples. As a result of the data-driven jet background estimate, the uncertainty in each bin is partially correlated with the uncertainty on the data in that bin.

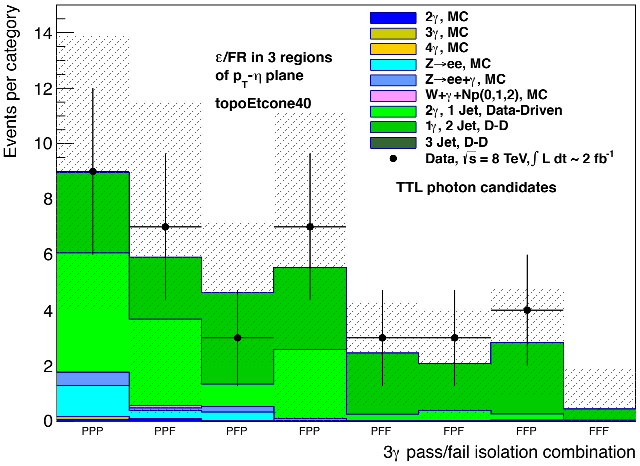

Figure 1.59: Observed and expected yields in events with three photons, where photon isolation efficiencies and jet fake rates are calculated in three regions of the $p_T - \eta$ plane, and have been used for the data-driven jet background estimate, using $E_T^{topo\ iso}$ as the isolation variable, TTL$'$ region, restricted to $80 < m_{3\gamma} < 100$ GeV$/c^2$. The red cross-hatched band is the combined statistical uncertainty of the data-driven jet background estimate and the sum of all MC samples. As a result of the data-driven jet background estimate, the uncertainty in each bin is partially correlated with the uncertainty on the data in that bin.

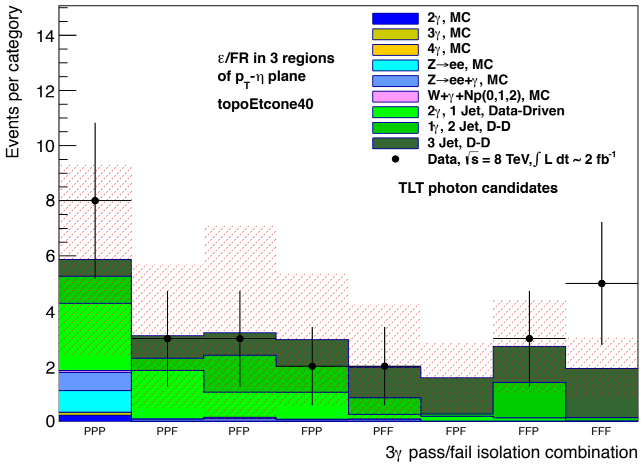

Figure 1.60: Observed and expected yields in events with three photons, where photon isolation efficiencies and jet fake rates are calculated in three regions of the $p_T - \eta$ plane, and have been used for the data-driven jet background estimate, using $E_T^{topo\ iso}$ as the isolation variable, TL′T region, restricted to $80 < m_{3\gamma} < 100$ GeV$/c^2$. The red cross-hatched band is the combined statistical uncertainty of the data-driven jet background estimate and the sum of all MC samples. As a result of the data-driven jet background estimate, the uncertainty in each bin is partially correlated with the uncertainty on the data in that bin.

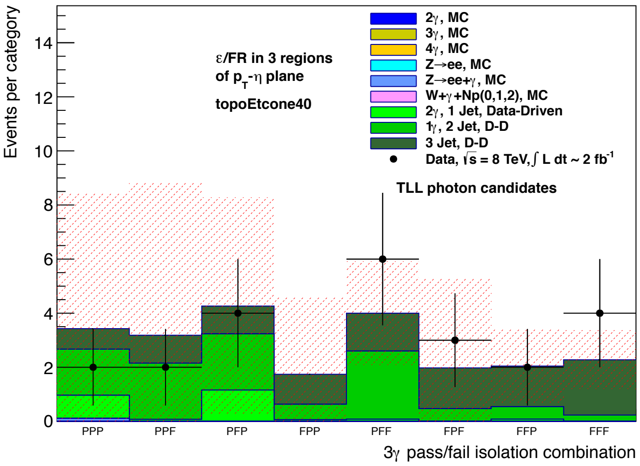

Figure 1.61: Observed and expected yields in events with three photons, where photon isolation efficiencies and jet fake rates are calculated in three regions of the $p_T - \eta$ plane, and have been used for the data-driven jet background estimate, using $E_T^{topo\ iso}$ as the isolation variable, TL$'$L$'$ region region, restricted to $80 < m_{3\gamma} < 100$ GeV$/c^2$. The red cross-hatched band is the combined statistical uncertainty of the data-driven jet background estimate and the sum of all MC samples. As a result of the data-driven jet background estimate, the uncertainty in each bin is partially correlated with the uncertainty on the data in that bin.

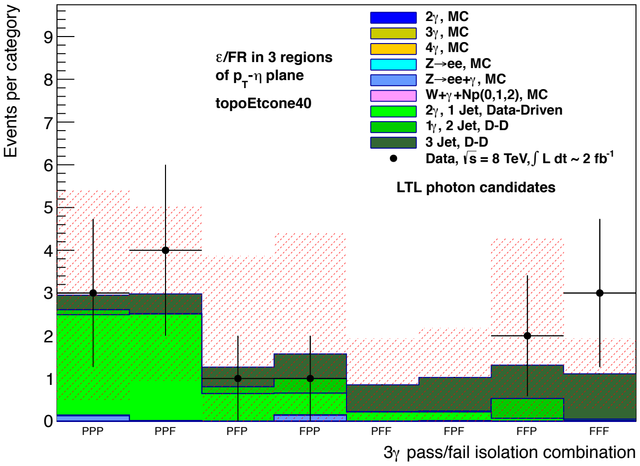

Figure 1.62: Observed and expected yields in events with three photons, where photon isolation efficiencies and jet fake rates are calculated in three regions of the $p_T - \eta$ plane, and have been used for the data-driven jet background estimate, using $E_T^{topo\ iso}$ as the isolation variable, L$'$TL$'$ region, restricted to $80 < m_{3\gamma} < 100$ GeV$/c^2$. The red cross-hatched band is the combined statistical uncertainty of the data-driven jet background estimate and the sum of all MC samples. As a result of the data-driven jet background estimate, the uncertainty in each bin is partially correlated with the uncertainty on the data in that bin.

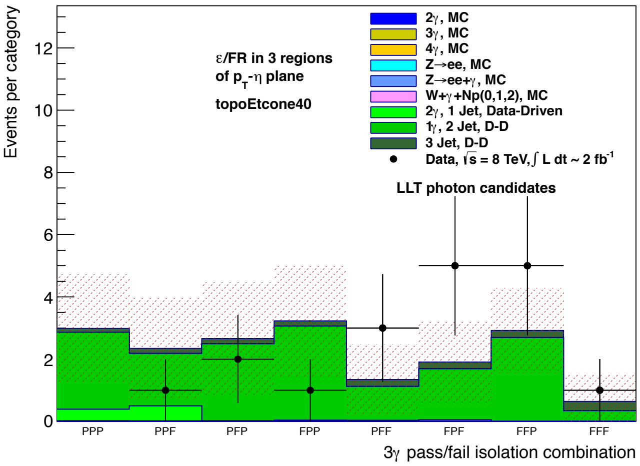

Figure 1.63: Observed and expected yields in events with three photons, where photon isolation efficiencies and jet fake rates are calculated in three regions of the $p_T - \eta$ plane, and have been used for the data-driven jet background estimate, using $E_T^{topo\ iso}$ as the isolation variable, L′L′T region, restricted to $80 < m_{3\gamma} < 100$ GeV$/c^2$. The red cross-hatched band is the combined statistical uncertainty of the data-driven jet background estimate and the sum of all MC samples. As a result of the data-driven jet background estimate, the uncertainty in each bin is partially correlated with the uncertainty on the data in that bin.

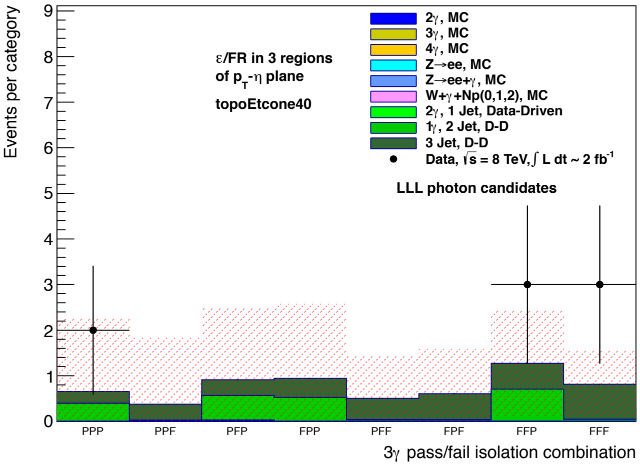

Figure 1.64: Observed and expected yields in events with three photons, where photon isolation efficiencies and jet fake rates are calculated in three regions of the $p_T - \eta$ plane, and have been used for the data-driven jet background estimate, using $E_T^{topo\ iso}$ as the isolation variable, L′L′L′ region, restricted to $80 < m_{3\gamma} < 100$ GeV/c^2. The red cross-hatched band is the combined statistical uncertainty of the data-driven jet background estimate and the sum of all MC samples. As a result of the data-driven jet background estimate, the uncertainty in each bin is partially correlated with the uncertainty on the data in that bin.

Background	TTT	TTL$'$	TL$'$T	TL$'$L$'$
2γ (MC)	2.39 ± 0.74	0.05 ± 0.04	0.22 ± 0.22	0.00 ± 0.00
3γ (MC)	1.00 ± 0.04	0.11 ± 0.01	0.11 ± 0.01	0.01 ± 0.00
4γ (MC)	0.00 ± 0.00	0.00 ± 0.00	0.00 ± 0.00	0.00 ± 0.00
2γ,1j (D-D)	6.10 ± 5.60	6.30 ± 4.13	2.97 ± 3.12	0.50 ± 4.64
1γ,2j (D-D)	1.96 ± 1.47	2.88 ± 1.31	0.98 ± 1.40	1.86 ± 1.01
3j (D-D)	0.30 ± 0.31	0.00 ± 0.53	0.61 ± 0.38	0.76 ± 0.62
Zee (MC)	4.52 ± 1.10	0.85 ± 0.53	0.32 ± 0.30	0.00 ± 0.00
Z+γ (MC)	5.07 ± 0.36	0.32 ± 0.09	0.44 ± 0.11	0.08 ± 0.04
W+γ+Np(0,1,2) (MC)	0.25 ± 0.06	0.01 ± 0.01	0.07 ± 0.03	0.00 ± 0.00
Total SM exp.	21.59 ± 5.96	10.53 ± 4.40	5.71 ± 3.46	3.20 ± 4.79
Observed 8 TeV (2 fb^{-1})	21	6	7	2

Table 1.20: Expected and observed event yields in signal and control regions defined in the text, for 10% of 8 TeV data, restricted to $80 < m_{3\gamma} < 100$ GeV/c^2. The three photon candidates are ordered by p_T, from highest to lowest, and photon isolation efficiencies and jet fake rates are calculated in three regions of the $p_T - \eta$ plane, and are used for the γ+j and all-jet background estimates, using $E_T^{topo\ iso}$ as the isolation variable. Background expectations taken from Monte Carlo simulations (data-driven calculations) are marked MC (D-D). Uncertainties are statistical only.

Background	L′TL′	L′L′T	L′L′L′
2γ (MC)	0.00 ± 0.00	0.00 ± 0.00	0.00 ± 0.00
3γ (MC)	0.00 ± 0.00	0.01 ± 0.00	0.00 ± 0.00
4γ (MC)	0.00 ± 0.00	0.00 ± 0.00	0.00 ± 0.00
2γ,1j (D-D)	2.35 ± 1.84	0.37 ± 1.54	0.00 ± 1.43
1γ,2j (D-D)	0.12 ± 1.60	2.48 ± 0.85	0.11 ± 0.65
3j (D-D)	0.34 ± 0.21	0.12 ± 0.32	0.39 ± 0.24
Zee (MC)	0.00 ± 0.00	0.00 ± 0.00	0.00 ± 0.00
Z+γ (MC)	0.12 ± 0.06	0.00 ± 0.00	0.00 ± 0.00
W+γ+Np(0,1,2) (MC)	0.02 ± 0.01	0.02 ± 0.02	0.00 ± 0.00
Total SM exp.	2.95 ± 2.45	2.99 ± 1.79	0.50 ± 1.59
Observed 8 TeV (2 fb^{-1})	3	0	2

Table 1.21: Expected and observed event yields in signal and control regions defined in the text, for 10% of 8 TeV data, restricted to $80 < m_{3\gamma} < 100$ GeV/c^2, continued. The three photon candidates are ordered by p_T, from highest to lowest, and photon isolation efficiencies and jet fake rates are calculated in three regions of the $p_T - \eta$ plane, and are used for the γ+j and all-jet background estimates, using $E_T^{topo\ iso}$ as the isolation variable. Background expectations taken from Monte Carlo simulations (data-driven calculations) are marked MC (D-D). Uncertainties are statistical only.

1.9 Conclusion

A search has been performed for new phenomena in events with at least three photons using 10% of 20.3 fb^{-1} of ATLAS data at $\sqrt{s} = 8$ TeV. The p-value for the null (SM) hypothesis is observed to be 0.095, corresponding to a significance, in units of Gaussian σ, of 1.31.

In addition, a search for local excesses in the two-photon and three-photon invariant mass distributions has been conducted. Upper limits at the 95% CL are calculated on the fiducial cross section for events from non-SM processes σ_{fid} as a function of new particle mass, for a general Gaussian resonance of fixed width 2 GeV/c^2, and are expected to range from 2×10^{-3} to 7×10^{-3} for $5 < m_{2\gamma} < 125$ GeV/c^2. Moreover, the 95% CL upper limits on $\sigma \times \mathcal{A}$ as a function of new particle mass, for a general Gaussian resonance of fixed width 2 GeV/c^2, are expected to range from 1×10^{-3} to 4×10^{-3} for $5 < m_{2\gamma} < 125$ GeV/c^2 and $\sim 2 \times 10^{-3}$ for 70 $< m_{3\gamma} < 200$ GeV/c^2.

The results are interpreted in the context of a benchmark signal scenario of a Higgs boson decaying into four photons via two intermediate pseudoscalar (a) particles, and limits for the full 2012 dataset are expected to be $BR(h \to aa) \times BR(a \to \gamma\gamma)^2 < 6 \times 10^{-4}$, for $10 < \mathrm{m}_a < 60$ GeV/c^2, and the upper limit on $BR(h \to aa) \times BR(a \to \gamma\gamma)^2$ ranging from 6×10^{-3} to 5×10^{-4}, for $5 < \mathrm{m}_a < 10$ GeV/c^2. Additionally, the limit on the branching ratio of a SM Z boson decaying to three photons is found to be $BR(Z \to 3\gamma) < 3.09 \times 10^{-6}$.

Chapter 2

A search for a new, low mass vector gauge boson, with APEX

APEX is an experiment at Thomas Jefferson National Accelerator Facility (JLab) in Virginia, USA, that searches for a new gauge boson (A') with sub-GeV mass and coupling to ordinary matter of $g' \sim (10^{-6} - 10^{-2})e$. The experimental setup at JLab's Hall A is ideally suited to search for an A', as the accelerator system is designed to deliver medium-high-energy (1 GeV to 6 GeV, currently upgrading to 12 GeV) electrons with very small bunch spacing, allowing experiments to achieve large datasets in a relatively short amount of time. For APEX, electrons impinge upon a fixed target of high-Z material, and an A' would be produced via a process analogous to photon bremsstrahlung, decaying to an e^+e^- pair. A test run for the experiment, demonstrating proof of concept in addition to achieving a physics result published in PRL [51] was held in July of 2010, covering $m_{A'} =$ 175 to 250 MeV and couplings $g'/e > 10^{-3}$. A full run is approved and will cover $m_{A'} \sim 65$ to 525 MeV and $g'/e > 2.3 \times 10^{-4}$.

The remainder of this chapter describes APEX in more detail.

2.1 Motivations

The Standard Model (SM) of particle interactions is described by an $\mathrm{SU}(3)_C\times\mathrm{SU}(2)_L\times\mathrm{U}(1)_Y$ gauge group, where the forces are mediated by vector bosons. For an extension of this model to have thus far evaded detection the corresponding gauge boson must have a mass of $\mathcal{O}(\mathrm{TeV})$ or must be very weakly coupled to ordinary matter, with a coupling strength g' suppressed relative to the electromagnetic charge e by $\epsilon \equiv g'/e \sim 10^{-6} - 10^{-2}$ [52] (or, equivalently, $\alpha'/\alpha = \epsilon^2$). This new gauge boson, A', corresponding to a $\mathrm{U}(1)'$ extension of the SM, can acquire an effective interaction with electromagnetism via kinetic mixing, where quantum loops of arbitrarily heavy particles provide a means by which the hidden $\mathrm{U}(1)'$ sector couples to the visible sector; see, e.g., [17, 18, 19, 53, 54]. The possibility of the existence of an A' with a small EM charge can be tested at fixed target electron beam facilities such as the Thomas Jefferson National Accelerator Facility (JLab). APEX, The A Prime EXperiment, searches for an A' at JLab and is described in brief here. For a full description of the experiment see [55] and for a more detailed description of the results of the test run see [51].

In addition to the general interest in discovering an extension of the SM, a hidden gauge sector with a gauge boson with mass in the MeV to GeV range could address dark matter anomalies and the anomalous magnetic moment of the muon. For a complete discussion of these possibilities, see [20].

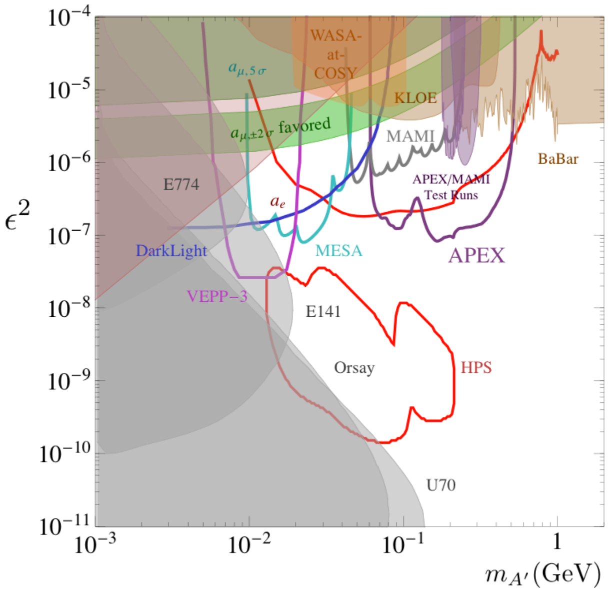

Figure 2.1: Existing and planned constraints in the $\epsilon - m_{A'}$ plane, as of late 2013.

2.2 Existing Constraints

Aside from these suggestive motivations, the coupling strength and mass of the A' are not predicted. Thus, searches for this new gauge boson must be conducted over wide ranges of both. As a result, prior to 2009, the areas of parameter space probed by APEX were remarkably weakly constrained, since previous collider experiments that are sensitive to low mass particles would not have been able to collect large enough datasets to discover a particle with such a weak coupling to ordinary matter. Following the observation [20] that much of this range could be probed at existing experimental facilities, a renewed interest in such experiments has led to the current constraints and planned experimental sensitivities shown in Figure 2.1 (from [56]). For a complete description of these constraints, see [57] and references therein.

As seen in Figure 2.1, APEX covers a large portion of this area of parameter

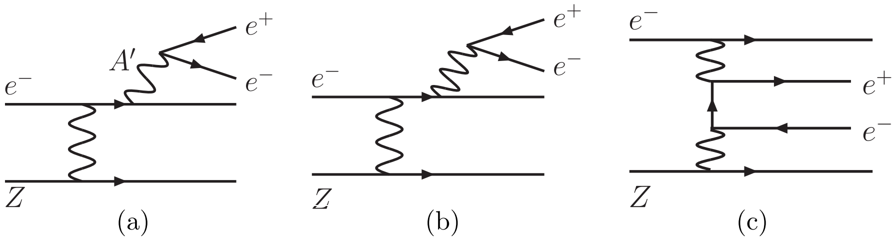

Figure 2.2: A' signal process (a) and irreducible QED backgrounds (b) and (c).

space, from $m_{A'} \sim 65$ to 525 MeV and with coupling reach to $g'/e > 2.3 \times 10^{-4}$. A test run for APEX was performed in July of 2010 and demonstrated the feasibility of the full experiment.

2.3 APEX at Jefferson Lab's Hall A

APEX is designed to take full advantage of JLab's Continuous Electron Beam Accelerator Facility and the two High Resolution Spectrometers (HRSs) in Hall A. For the test run, an electron beam of energy 2.260 GeV and an intensity of up to 150 μA was used, incident upon a tantalum foil of thickness 22 mg/cm^2. The central momentum of each HRS was $\simeq 1.131$ GeV with a momentum acceptance of ± 4.5%.

An A' is produced via a process analogous to photon bremsstrahlung and decays to an e^+e^- pair; thus, the A' signal will appear as a small, narrow bump in the invariant mass spectrum of e^+e^- pairs from background QED processes. The diagrams for signal and irreducible backgrounds are shown in Figure 2.2.

The opening angle Θ_0 of the e^+e^- pair is set by $m_{A'}$ and the incident electron beam energy as $\Theta_0 \sim m_{A'}/E_b \approx 5^\circ$, with no such expectation for the QED backgrounds. This motivates a symmetric HRS configuration with both spectrometer arms positioned far forward. To optimize sensitivity to A' decays, dipole sep-

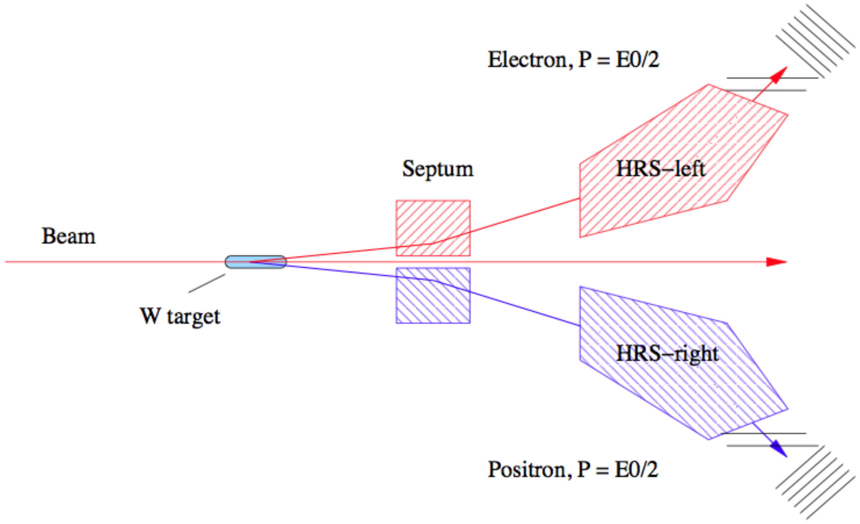

Figure 2.3: A schematic overhead view of the setup in JLab's Hall A, indicating the positioning of the septum magnets just past the target enclosure, so placed as to allow for the detection of A' decay products which are expected to have a very small opening angle.

tum magnets are placed between the target and the HRS aperture. A schematic overhead view of this setup is shown in Figure 2.3, and a side view in Figure 2.4.

The Hall A HRSs consist of several different components to allow for the measurement of the position and momentum of charged particles to a high degree of accuracy. A schematic view is shown in Figure 2.5. Vertical drift chambers allow for an accurate determination of the full 3D track of an incoming particle. Two separate sets of scintillators provide timing information, to identify coincident e^+e^- pairs. Online particle ID is provided by a gas Cherenkov detector and a lead glass calorimeter allows for further offline rejection of pion backgrounds. A sieve-slit method is used for optics calibration.

Excellent mass resolution is required to enable the identification of an A' resonance. The HRSs are designed to achieve high momentum resolution at the level of $\delta p/p \sim 10^{-4}$, providing a negligible contribution to the mass resolution. Angular

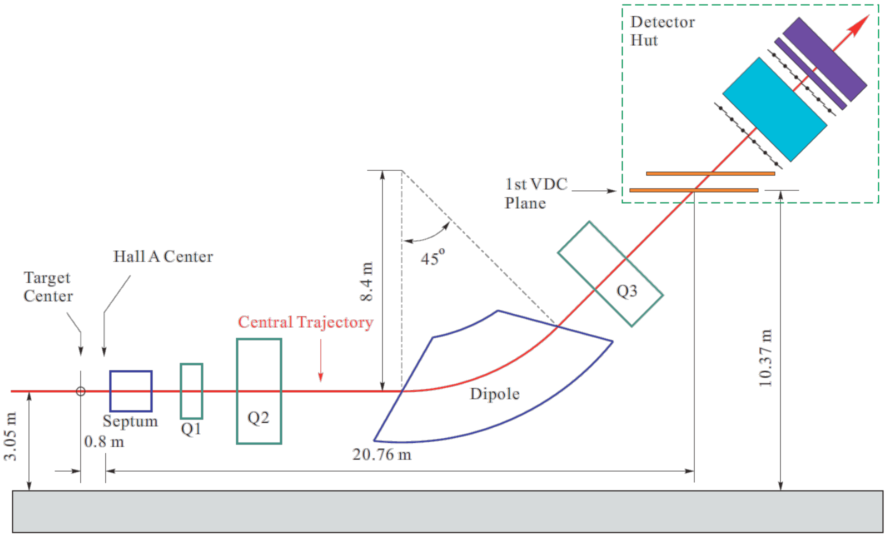

Figure 2.4: A schematic side view of the setup in JLab's Hall A.

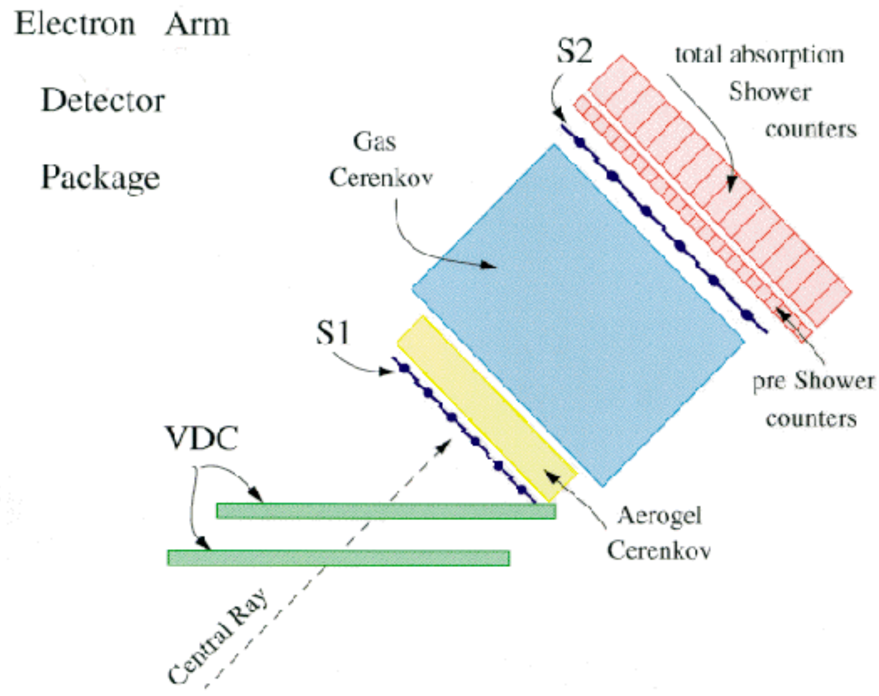

Figure 2.5: A schematic side view of electron-arm High Resolution Spectrometer (HRS) in JLab's Hall A. A similar setup is available in the positron arm.

mrad	Optics	Tracking	MS in target
σ(horiz)	0.11	~0.4	0.37
σ(vert)	0.22	~1.8	0.37

Table 2.1: Contributions to APEX mass resolution.

resolution and multiple scattering in the target are the dominant contributions to the mass resolution, as shown in Table 2.1.

For the test run, APEX achieved a mass resolution of $\sigma \sim 0.85-1.11$ MeV, varying over the full $m_{A'}$ range.

Reducible backgrounds, including electron or proton singles, pions, accidental e^+e^- coincidences, and e^+e^- pairs from real photon conversions, are rejected using a combination of different triggers.

The final event sample trigger for the test run required a double coincidence gas Cherenkov signal within a 12.5 ns window in each arm. The resulting data sample consisted of 770,500 true e^+e^- coincident events with 0.9% (7.4%) meson (accidental e^+e^- coincidence) contamination.

2.4 Resonance search

The final data sample forms the basis of an invariant mass spectrum of e^+e^- pairs (shown in Figure 2.6), which is the starting point for the $A' \to e^+e^-$ search. Since the A' is expected to appear as a small, narrow bump on top of a smooth spectrum of background processes, a resonance search (also known as a raster scan or bump hunt) is performed to identify statistically significant excesses along the full mass spectrum.

In general, the procedure is as follows: One scans along the mass spectrum, and at each mass bin one hypothesizes a Gaussian peak of an unknown height and width

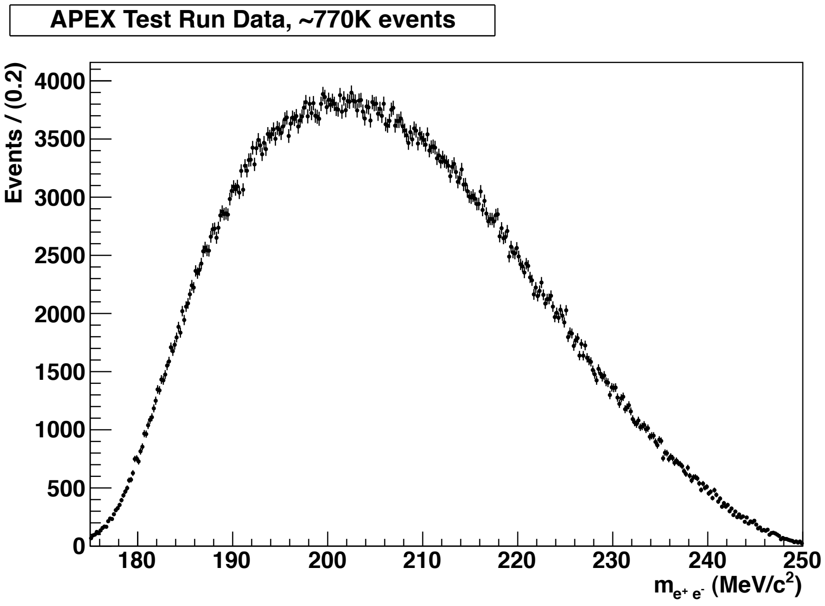

Figure 2.6: Distribution of $m_{e^+e^-}$, the result of the final selection for the APEX test run data.

σ (also unknown but expected to be $\mathcal{O}(\mathrm{MeV/c^2})$) equal to the experimental mass resolution. For a fixed A' mass $m_{A'}$ and given hypotheses for the number of signal events S and number of background events B, one models events as distributed according to a probability distribution given by

$$P(m_{e^+e^-}) = \frac{1}{S+B}(S \cdot \mathrm{N}(m_{e^+e^-}|m_{A'}, \sigma) + B \cdot \mathrm{Polynomial}(m_{e^+e^-}, a_i)) \qquad (2.1)$$

where m_{e+e-} is the invariant mass of the electron-positron pair, N is a normal/Gaussian probability distribution, and the background shape is given by a polynomial with coefficients a_i. From the likelihood function, L, based on this probability model, we form a test statistic, $-2\, ln\, \lambda(\mathrm{S})$, where $\lambda(\mathrm{S})$ is the profile likelihood ratio (PLR),

$$\lambda(S) = \frac{L(S, \hat{\hat{B}}, \hat{\hat{a}}_i)}{L(\hat{S}, \hat{B}, \hat{a}_i)} \tag{2.2}$$

and where $\hat{}$ ($\hat{\hat{}}$) indicates the unconditional (conditional) maximum likelihood estimator for that parameter, arrived at via fits of the model to the data. The systematic uncertainty in the background shape is incorporated into the profile likelihood ratio via the nuisance parameters a_i, the coefficients of the polynomial. An example of the results of the procedure of fitting the probability model to the data within one window is shown in Figure 2.7. We then determine a confidence interval in number of signal events S, i.e., we determine the range in S consistent with the data at a given confidence level. The upper limit of this confidence interval corresponds to a limit on S.

For the specifics of the analysis of the APEX test run data, based on extensive simulated-experiment studies, a 7th-order polynomial fit over a 30.5 MeV window is found to strike a near optimal balance between the simultaneous needs to maximize sensitivity to a signal and minimize pull (defined as $S_{bestfit}/\sigma_{S,bestfit}$) across the full mass spectrum; see Figures 2.8 and 2.9.

A symmetric scanning window is used, except for candidate A' masses within 15 MeV of the upper or lower boundaries, for which the window size is adjusted to correspond to twice the distance from the candidate mass to the boundary. The binned PLR described above is computed as a function of number of signal events S at the candidate mass, using 0.05 MeV bins. The PLR is used to derive the local probability (p-value) at $S = 0$ (i.e. the probability of a larger PLR arising from statistical fluctuations in the background-only model) and a 90%-confidence upper limit on the signal. The sensitivity of the search is defined in terms of a

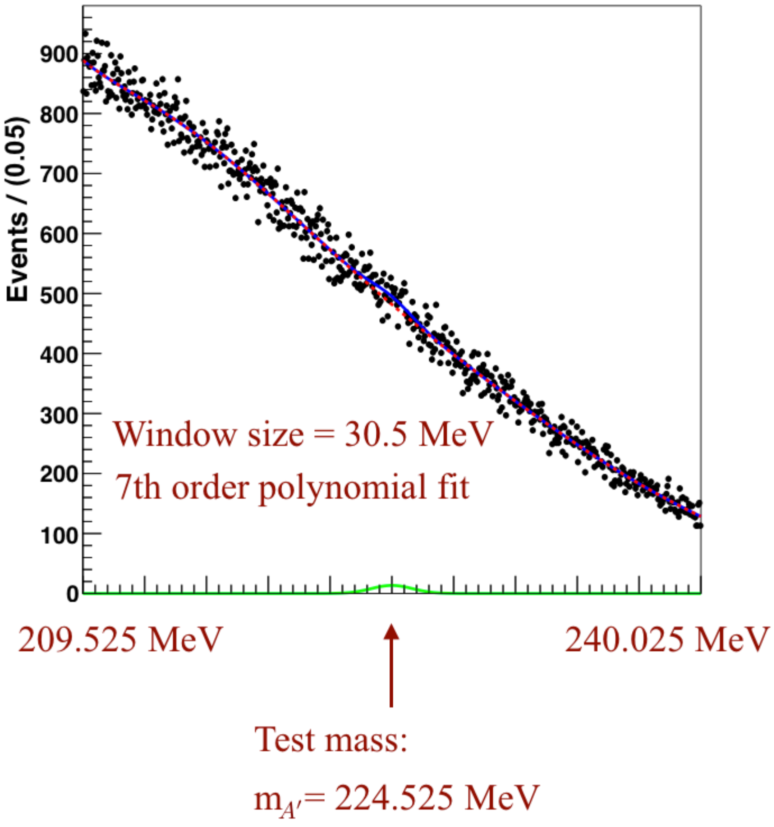

Figure 2.7: An example window for the resonance search across the APEX test run dataset, consisting of the invariant masses of e^+e- pairs. The full probability model that is fit to the data is composed of the background polynomial model, shown as the red dotted line, and the Gaussian signal component, shown as the green line at the bottom of the plot. The signal+background model is shown as the blue curve.

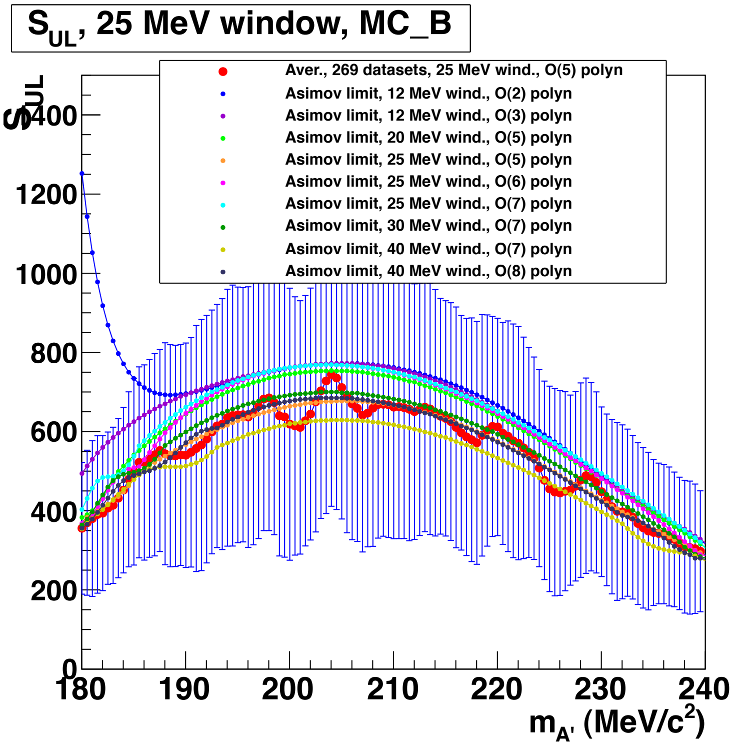

Figure 2.8: Upper limit on number of signal events, S, a result of a scanning-window resonance search, as a function of $m_{A'}$, for both an ensemble of 269 pseudodatasets based on the APEX test run data, and for ideal expected datasets without fluctuations (Asimov). The different limit curves correspond to different values used for the size of the scanning window and the order of the polynomial used in the window. This plot, in conjunction with Figure 2.9, indicates that the optimal values are a 30 MeV window and 7th order polynomial.

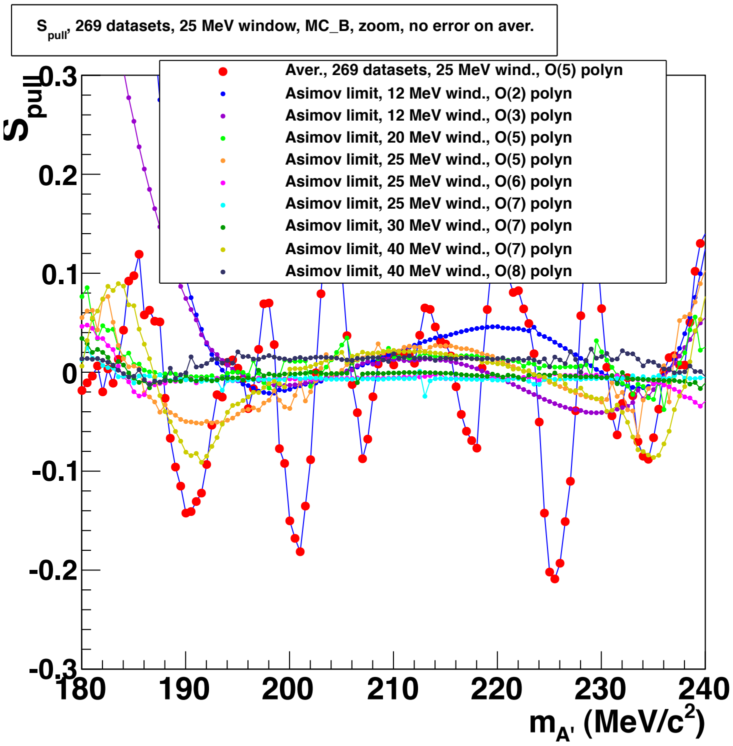

Figure 2.9: Signal pull, defined as $S_{bestfit}/\sigma_{S,bestfit}$, a result of a scanning-window resonance search, as a function of $m_{A'}$, for both an ensemble of 269 pseudodatasets based on the APEX test run data, and for ideal expected datasets without fluctuations (Asimov). The different limit curves correspond to different values used for the size of the scanning window and the order of the polynomial used in the window. This plot, in conjunction with Figure 2.8, indicates that the optimal values are a 30 MeV window and 7th order polynomial.

50% power-constraint [58], which means we do not regard a value of S as excluded if it falls below the expected limit. This procedure is repeated in steps of 0.25 MeV/c^2. A *global* p-value, corrected for the "look-elsewhere effect", (the fact that an excess of events *anywhere* in the range can mimic a signal), is derived from the lowest local p-value observed over the full mass range, and calibrated using simulated experiments.

2.5 Test Run Results

No significant excess was found over the invariant mass range of $m_{A'} = 175$ to 250 MeV; see Figures 2.10, 2.11 and 2.13. The most significant excess was at 224.5 MeV with a p-value of 0.06%. Out of ~1000 pseudoexperiments based on the test run data, 40% yielded a p-value at least as extreme as 0.06% somewhere in the mass range.

The upper limit on number of signal events, S, compatible with a background fluctuation at the 90% CL was translated into an upper limit on the A' coupling, α'/α, by exploiting the kinematic similarities between A' and γ^* production [20]. Based on Monte Carlo simulations, the ratio f of the radiative-only cross section to the full QED background cross section varies linearly from 0.21 to 0.25 across the APEX mass range and, thus, all backgrounds can be normalized to the radiative background. The final expression relating S_{max} and $(\alpha'/\alpha)_{max}$ is

$$\left(\frac{\alpha'}{\alpha}\right)_{max} = \left(\frac{S_{max}/m_{A'}}{f \cdot \Delta B/\Delta m}\right) \times \left(\frac{2N_{\text{eff}}\alpha}{3\pi}\right),$$

where N_{eff} counts the number of available decay channels ($N_{eff} = 1$ for $m_{A'} < 2m_\mu$, and increases to $\simeq 1.6$ at $m_{A'} \simeq 250$ MeV). A schematic view of the approach

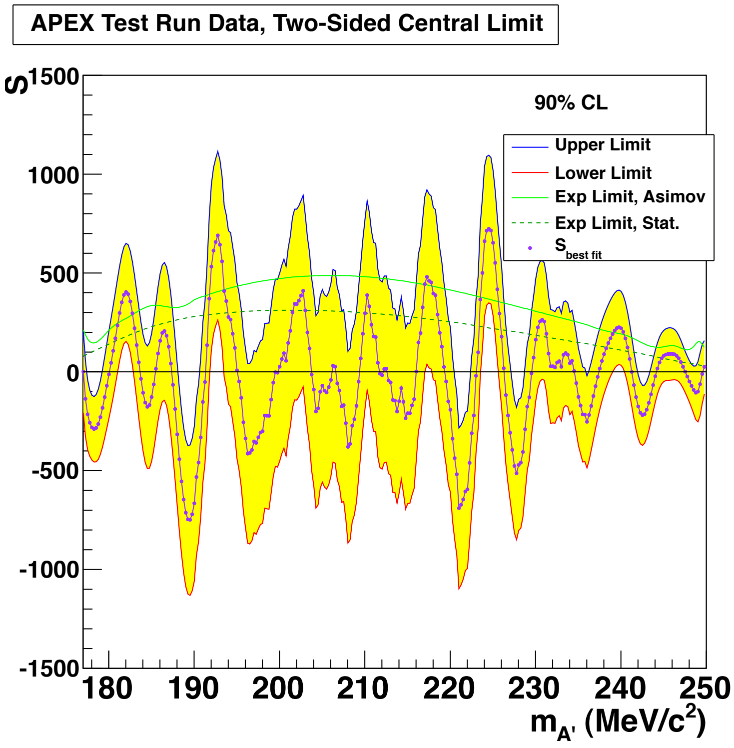

Figure 2.10: Two-sided central limits on number of signal events, S, a result of a scanning-window resonance search, as a function of $m_{A'}$, for the APEX test run data.

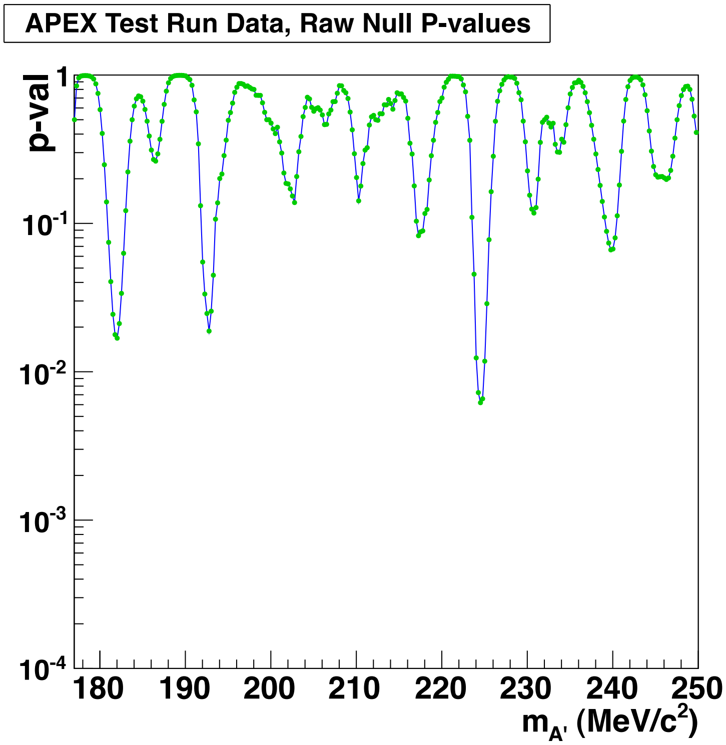

Figure 2.11: P-values for the null hypothesis, the result of a scanning-window resonance search, as a function of $m_{A'}$, for the APEX test run data.

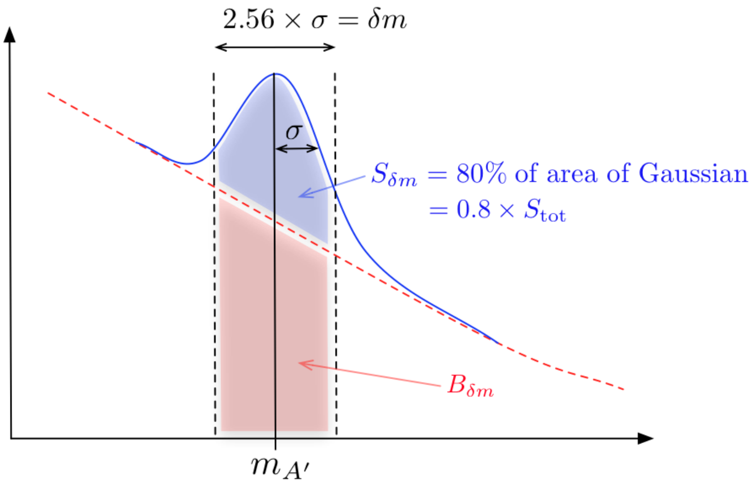

Figure 2.12: A schematic of the approach to determining number of signal events, S, over number of background events, B, in a resonance search.

by which S and B are calculated for each mass hypothesis is shown in Figure 2.12. The upper limit on coupling is shown in Figure 2.14.

The data from the test run, in the form of the invariant mass values of the e^+e^- pairs, are publicly available [59].

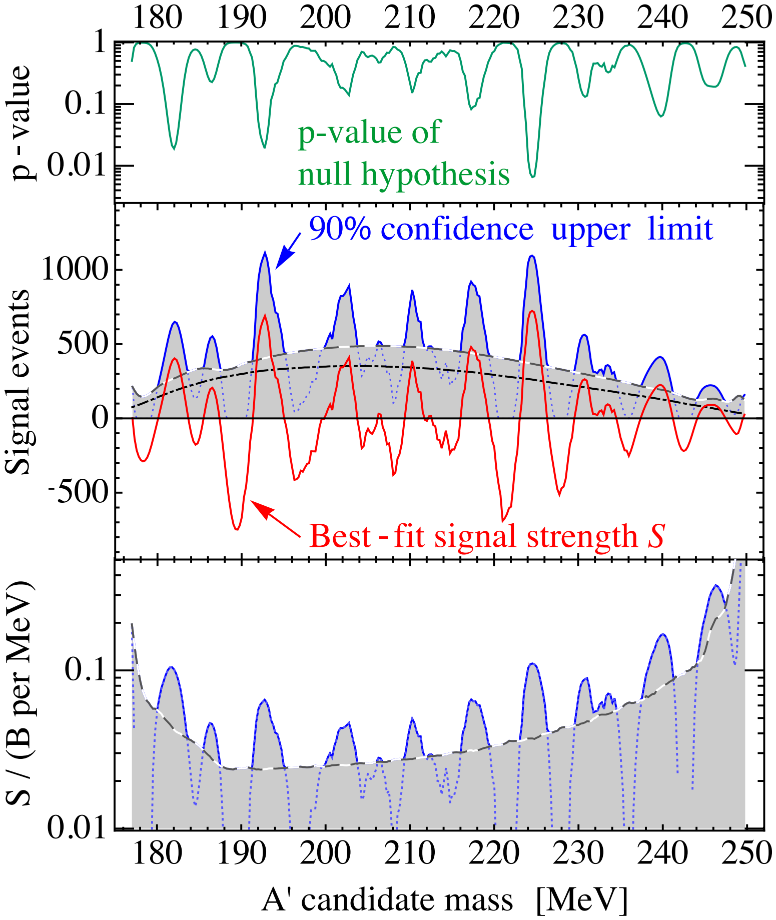

Figure 2.13: Results of the resonance search.

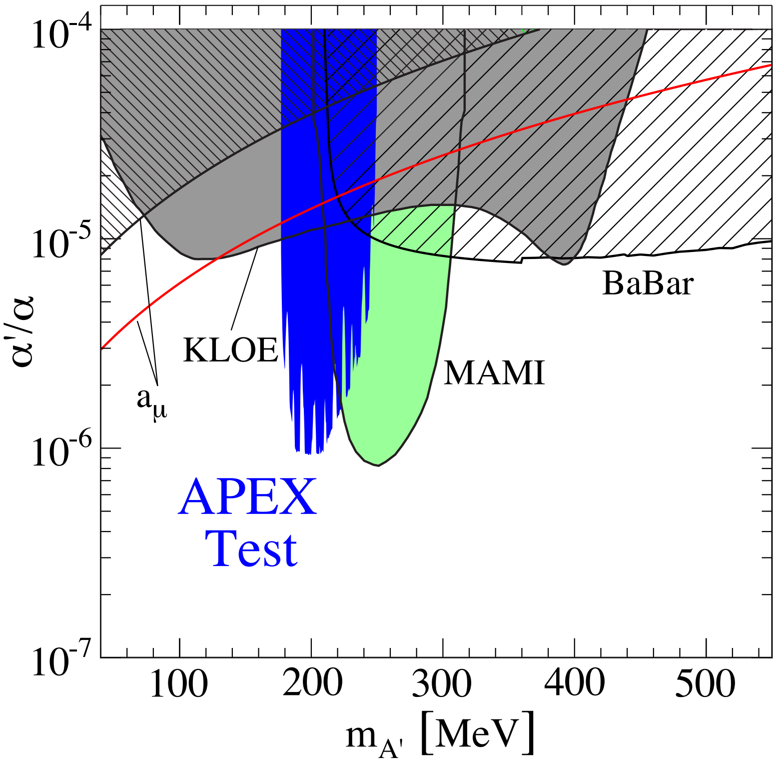

Figure 2.14: Upper limit on coupling.

Chapter 3

A search for $h \to aa \to 4\tau$, with ALEPH

3.1 Overview: Higgs to four taus at ALEPH

A search has been performed on 683 pb^{-1} of data collected by the ALEPH detector at the Large Electron-Positron (LEP) collider at center-of-mass energies from 183 to 209 GeV looking for a Higgs boson decaying into four τ leptons via intermediate pseudoscalar a particles, for a Higgs mass range of 70 to 114 GeV/c^2 and an a mass range of 4 to 12 GeV/c^2. No excess above background is seen and a limit is placed on $\xi^2 = \frac{\sigma(e^+e^- \to Z+h)}{\sigma_{SM}(e^+e^- \to Z+h)} \times (h \to aa) \times (a \to \tau^+\tau^-)^2$ in the m_h, m_a plane. For $m_h < 114$ GeV/c^2 and $m_a < 10$ GeV/c^2, $\xi^2 > 1$ can be excluded at the 95% confidence level.

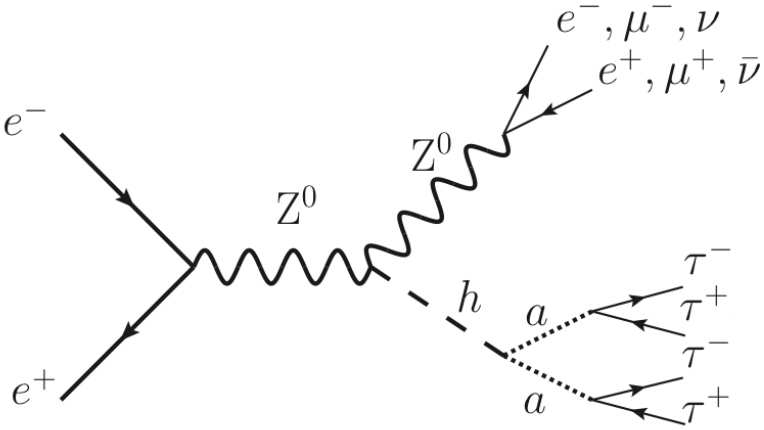

Figure 3.1: The Feynman diagram for the production of a Higgs boson in association with a Z boson in e^+e^- collisions with the decay of the Z boson to neutrinos, electrons or muons, and the decay of the Higgs to four tau leptons via intermediate pseudoscalar a particles.

3.2 Introduction

Direct searches at LEP2 for the standard model (SM) Higgs boson, h, decaying into $b\bar{b}$ or $\tau^+\tau^-$ placed a lower bound of 114 GeV/c^2 on the Higgs mass [60]. However, prior to the discovery of the SM Higgs by the ATLAS and CMS Collaborations in July of 2012, fits of the SM to electroweak precision data favored a SM Higgs with a mass within the kinematic limit of LEP. Additionally, a small, non-SM-like excess observed at a Higgs mass of around 100 GeV/c^2 in the $b\bar{b}$ final state at LEP, combined with the fine-tuning needed in the minimal supersymmetric standard model (MSSM), led to the consideration of models, such as the next-to minimal supersymmetric standard model (NMSSM) [61], that featured exotic Higgs boson decays and naturally light pseudoscalar particles, a. Such models and related scenarios often feature scalar and pseudoscalar particles that can accompany the scalar boson with a mass of ∼126 GeV/c^2 discovered at the LHC as part of an extended Higgs section. Indeed, for simplicity, for the rest of this chapter, the symbol h and the word "Higgs" can represent lighter scalars than the SM Higgs discovered at the LHC.

In these models with lighter Higgs particles, new decay channels, such as $h \to aa$, can dominate over $h \to b\bar{b}$ and render the Higgs boson "invisible" to conventional searches. In particular, the Higgs can decay into four SM particles instead of two, via two intermediate a particles. Several of these possible final states, such as $h \to 2a \to 4b$, are already highly constrained by existing analyses; see Ref. [62], for example. For $m_a < 2m_b$, however, the decay $a \to \tau^+\tau^-$ is expected; this process, with the Higgs decaying into $\tau^+\tau^-\tau^+\tau^-$ for a Higgs mass range of 86 to 114 GeV/c^2, is not covered by existing analyses. The Feynman diagram for this process, for the decay channels considered in this analysis, is shown in Figure 3.1. To investigate this range, the ALEPH data has been revisited. The present analysis is described in detail in Ref. [63].

3.3 The ALEPH Detector

A complete description of ALEPH ("A detector for LEP PHysics"), shown in Figure 3.2, is presented in Ref. [64] and an account of its performance in Ref. [65]. The central part of the detector provides tracking for charged particles, and consists of a silicon vertex detector (VDET), a cylindrical drift chamber (ITC), and a large time projection chamber (TPC), all immersed in a 1.5 T magnetic field, generated by a superconducting solenoid. The VDET includes two concentric layers of silicon microstrip detectors that are an average of 6.5 cm and 11.3 cm away from the nominal interaction point. The inner and outer VDET layers cover 85% and 69% of the solid angle, respectively. The ITC, which is a multilayer axial-wire drift

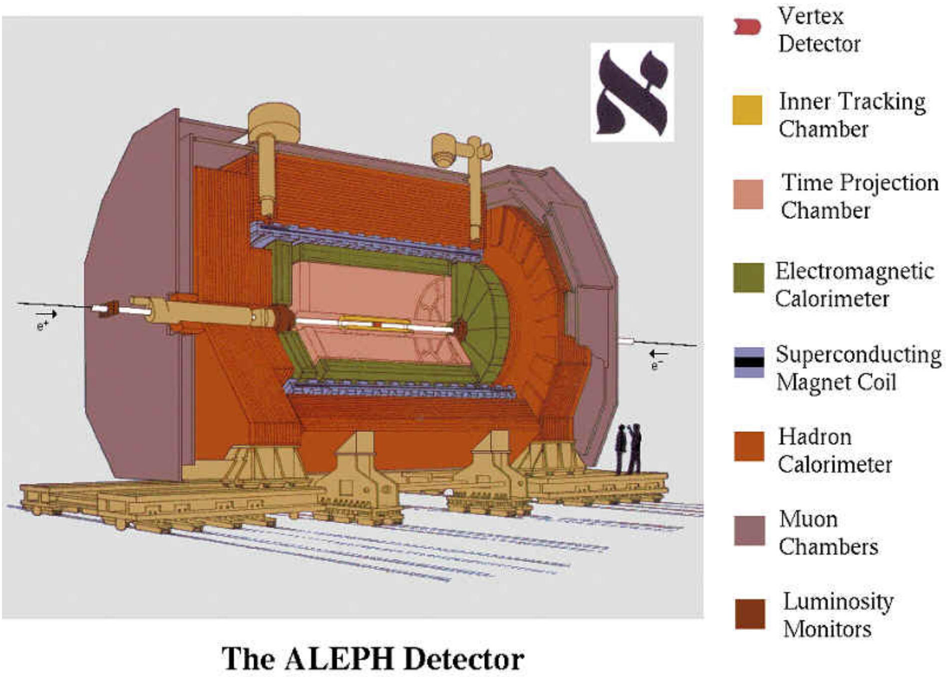

Figure 3.2: The ALEPH detector.

chamber also with cylindrical geometry, surrounds the VDET. The TPC provides up to 21 three-dimensional space points and 338 samples of ionization loss for charged particle tracks at radii between 30 and 180 cm. Overall, a transverse momentum resolution of $\sigma(1/p_T) = 0.6 \times 10^{-3} \oplus 0.005/p_T$ (GeV/c)$^{-1}$ is achieved.

The electromagnetic calorimeter (ECAL) is contained within the superconducting coil and surrounds the TPC. It is a lead/proportional-wire-chamber sampling device with fine readout segmentation and encompassing 22 radiation lengths. The ECAL allows for the identification of and discrimination between electrons and photons due to their characteristic showers. The energy resolution achieved for isolated electrons and photons is $\sigma(E)/E = 0.18/\sqrt{E} + 0.009$ (E in GeV).

The hadronic calorimeter (HCAL) is formed by the 1.2 m-thick magnetic field return yoke which serves as an absorber, and which is a large, fully instrumented iron structure. It consists of 23 layers of streamer tubes (for a total of 7.2 interaction lengths), together with two surrounding double-layers of muon chambers. The HCAL serves to provide a measurement of the hadronic energy, with a relative energy resolution of $\sigma(E)/E = 0.85/\sqrt{E}$ (E in GeV), and, together with the surrounding muon chambers, facilitates the identification of muons.

An energy flow algorithm has been developed to measure the total visible energy in an event, and which combines all of the above measurements [65], and which provides a relative resolution on the total visible energy of $0.60/\sqrt{E}$ for high multiplicity final states. Additionally, the application of the algorithm results in a set of reconstructed objects — *energy-flow objects* — that are categorized as charged particles, photons, or neutral hadrons. These energy-flow objects are the basic entities used in this analysis.

Below polar angles of 12° and down to 34 mrad from the beam axis, the acceptance is closed at both ends of the experiment by the luminosity calorimeter (LCAL) and a tungsten-silicon calorimeter (SICAL) originally designed for the LEP 1 luminosity measurement.

During LEP2 the machine operated at centre-of-mass energies from 183 to 209 GeV and collected data corresponding to a total integrated luminosity of 683 pb^{-1}. The average centre-of-mass energies and the corresponding integrated luminosities used in this analysis are presented in Table 3.1.

Table 3.1: Integrated luminosities collected at the different average centre-of-mass energies.

E_{CM}(GeV)	182.65	188.63	191.58	195.52	199.52	201.62	204.86	206.53
$\int \mathcal{L}dt$ (pb^{-1})	56.8	174.2	28.9	79.9	86.3	41.9	81.4	133.2

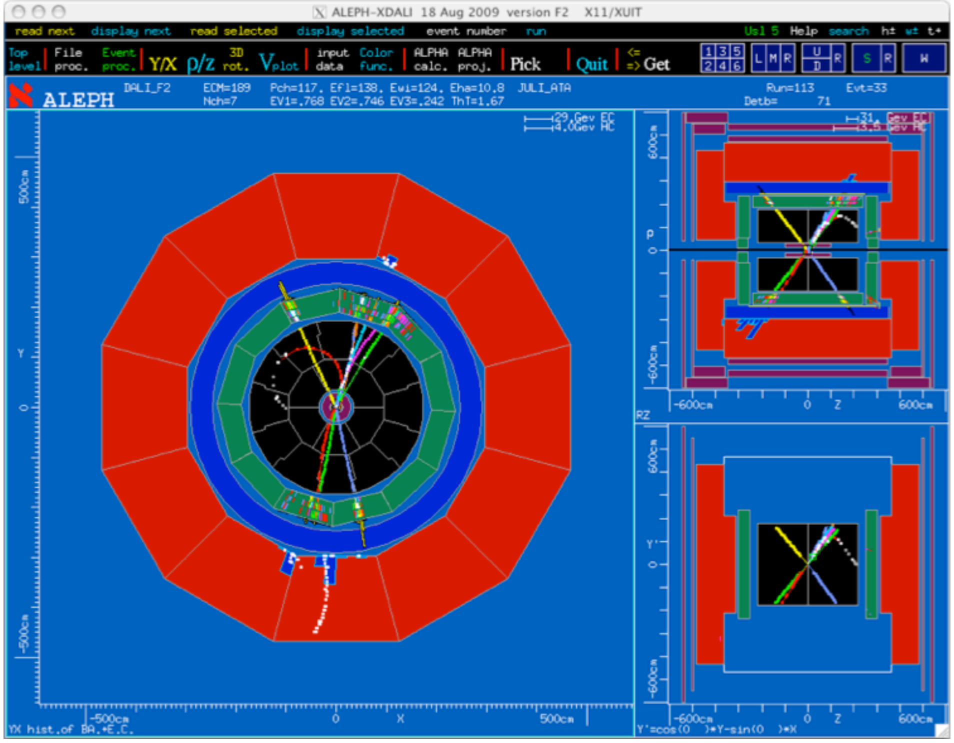

Figure 3.3: A simulated signal event for the Z decay channel of Z $\rightarrow e^+e^-$ as it would appear in the ALEPH detector.

3.4 Signal and Background Samples

All steps of the ALEPH analysis framework were revived for this analysis, including the ability to generate simulated samples of standard model background and data. Simulated signal events (with $h \rightarrow aa$ followed by $a \rightarrow \tau^+\tau^-$) were produced for each of the three Z decay channels considered and for each combination of Higgs boson and pseudoscalar masses in the ranges $70 < m_h < 114$ GeV/c^2 and $4 < m_a < 12$ GeV/c^2 in steps of 2 GeV/c^2, and included 3000 events per point. For the relevant background processes, the samples were either 10-30 or 300-1000 times larger than the data, depending upon the process. An event display for a simulated signal event for the Z decay channel of Z $\rightarrow e^+e^-$ is shown in Figure 3.3.

3.5 Event Selection

For the mass range considered, the Higgs is produced approximately at rest, and thus the decay $h \to 2a \to 4\tau$ results in a pair of taus recoiling against another pair of taus. For the a mass range considered, the decay products of each 2τ system will be observed as a highly-collimated jet of charged particles. Due to this high level of collimation, individual identification of taus, via standard algorithms, would fail. Instead, the fact that each tau decays into either one charged particle or three charged particles was used, and one would thus expect each a jet to contain two, four or six tracks. The JADE algorithm was used to form jets with a y_{cut} chosen to merge proto-jets up to a mass of $m_{jet} = 15$ GeV/c^2.

Three possible decays of the Z boson were considered, namely Z $\to e^+e^-$, Z $\to \mu^+\mu^-$, and Z $\to \nu\bar{\nu}$, and a set of *loose* selection criteria (convenient to allow comparison of data and simulation at an intermediate stage without compromising the blind nature of the analysis) and *final* selection criteria were formulated for each of the two Z decay classes considered: Z $\to l^+l^-$ (where $l = e$ or μ) and Z $\to \nu\bar{\nu}$.

3.5.1 Z $\to l^+l^-$

For the Z $\to l^+l^-$ channel, four-fermion background processes are prominent. The ALEPH lepton identification algorithms were used to mask the two most energetic leptons in the event from the list of objects clustered by the JADE jet-finding algorithm. The loose selection consisted of the following requirements: Two oppositely-charged, isolated leptons; two jets, well-contained within the tracking volume ($|\cos\theta_j| < 0.9$); and the jets and leptons sufficiently isolated from each other ($|\cos\theta_{jl}^{min}| < 0.95$). The final selection consisted of the following requirements: The invariant mass of the lepton pair near the Z mass ($80 < m_{l^+l^-(\gamma)} < 120$ GeV/c^2, where γ indicates an isolated photon that may have been radiated from one of the leptons and which is added to the di-lepton system if doing so corresponds to an invariant mass closer to the Z mass than the di-lepton pair alone); missing energy due to neutrinos from tau decays ($\not{E} > 20$ GeV); jets sufficiently separated ($|\cos\theta_{jj}| < 0$); and a signal-like track multiplicity, i.e., each jet must contain either two or four tracks.

3.5.2 Z $\rightarrow \nu\bar{\nu}$

The Z $\rightarrow \nu\bar{\nu}$ channel represents a larger branching ratio of the Z than the lepton channel, and thus drives the analysis. A major background contribution arises from $\gamma\gamma$ events. The loose selection consisted of the following requirements: Modest missing energy and missing mass ($\not{E} > 30$ GeV and $\not{m} > 20$ GeV/c^2); exactly two jets, well-contained in the tracking volume, with a modest invariant mass cut on the dijet system ($|\cos\theta_j| < 0.85$ and $m_{jj} > 10$ GeV/c^2); requirements on the angle of the missing momentum vector with the beam axis and the total visible energy in the event, to reject substantial portions of two-photon-initiated and beam background events ($|\cos\theta_{miss}| < 0.9$ and $E_{vis} > 0.05\ E_{CM}$); and modest requirements on the most energetic jet ($E_{j_1} > 25$ GeV and containing either two or four tracks). The final selection consisted of the following requirements: Less than 5 GeV within 30° of the beam axis, to reject events with energy deposits in the forward region of the detector; consistency with the Z boson decaying to neutrinos ($\not{E} > 60$ GeV and $\not{m} > 90$ GeV/c^2); small aplanarity (< 0.05), consistent with two back-to-back, highly collimated jets; and a signal-like track multiplicity, i.e., each

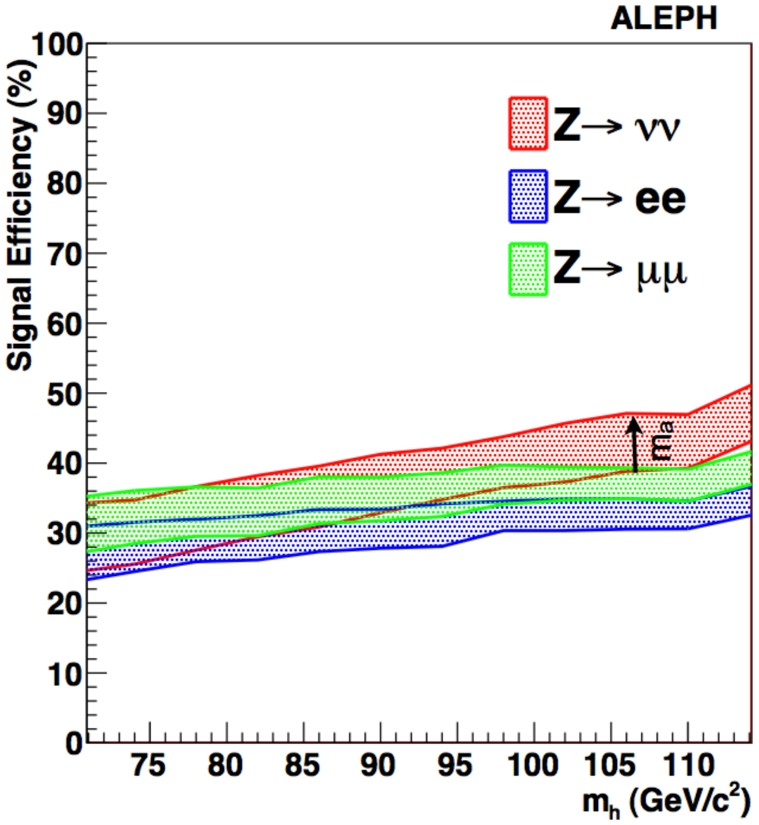

Figure 3.4: Signal efficiency as a function of m_h for the different Z decay channels. The bands represent moving from lower m_a (lower y-axis values) to higher m_a (higher y-axis values).

jet must contain either two or four tracks.

3.6 Results

Based upon these selection criteria, the signal efficiency ranged from ∼25% to ∼50%, depending on Z decay channel, Higgs mass, and a mass, as shown in Figure 3.4.

It was determined that, for the Z $\rightarrow l^+l^-$ channel, one should expect ∼3 signal events versus < 0.2 background events, and for the Z $\rightarrow \nu\bar{\nu}$ channel the expectation

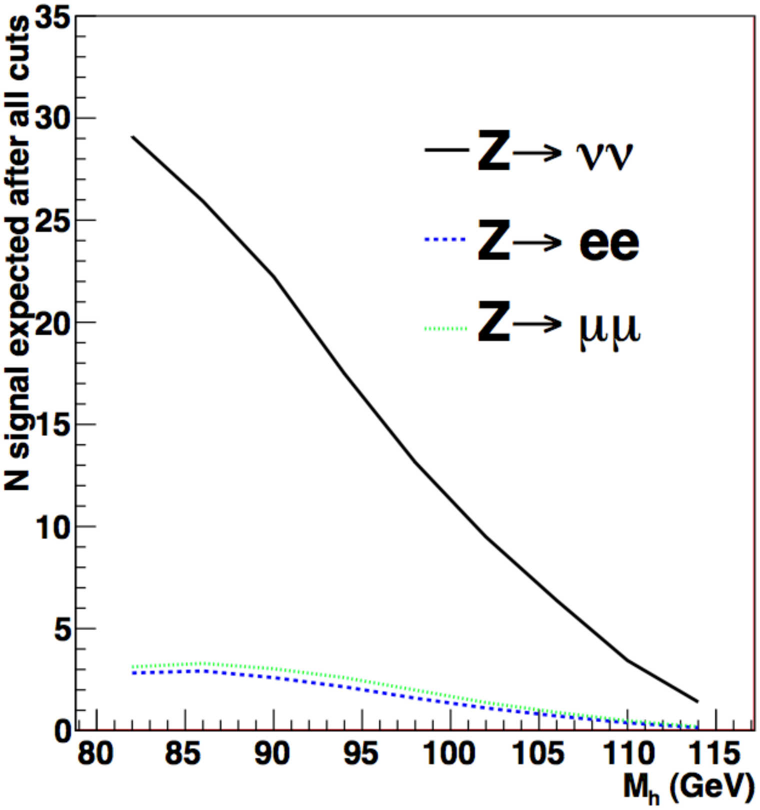

Figure 3.5: Expected number of signal events after final selection, as a function of m_h, for the different Z decay channels.

was ~11 signal events versus ~6 background events. The expected number of signal events after the final selection for the different Z decay channels is shown as a function of m_h in Figure 3.5.

Systematic uncertainties in the Monte Carlo simulation were estimated to be 5% for all signal and 10% for background in the Z $\to l^+l^-$ channel versus 30% for background in the Z $\to \nu\bar{\nu}$ channel. It was found that the background estimate and the number of events seen in data at the loose selection agreed within the systematic and statistical uncertainty for all Z channels. Distributions of reconstructed Z mass for the Z $\to l^+l^-$ channels at the loose selection point are shown in Figure 3.6.

For the Z $\to l^+l^-$ channels, zero events were observed after applying all se-

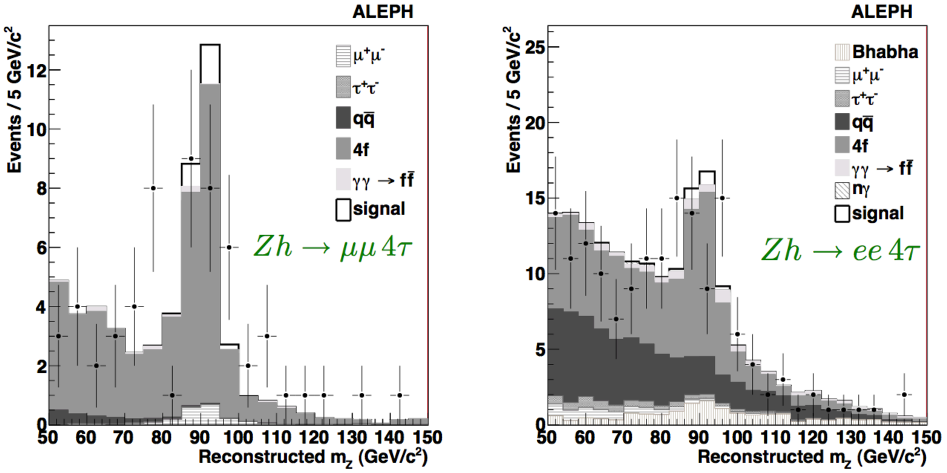

Figure 3.6: Distribution of reconstructed m_Z for the Z $\to l^+l^-$ channels, at the loose selection point defined in the text.

lection criteria, while for the Z $\to \nu\bar{\nu}$ channel two events were observed. These observations are consistent with background. The distribution of reconstructed m_Z for the Z $\to \mu^+\mu^-$ channel is shown in Figure 3.7 and the distribution of missing mass for the Z $\to \nu\bar{\nu}$ channel is shown in Figure 3.8.

Limits were placed on the cross section times branching ratio of the signal process with respect to the SM Higgsstrahlung production cross section, $\xi^2 = \frac{\sigma(e^+e^- \to Z+h)}{\sigma_{SM}(e^+e^- \to Z+h)} \times (h \to aa) \times (a \to \tau^+\tau^-)^2$. The limits are based upon event counts in three separate track multiplicity bins (corresponding to events with two jets where 1) each jet contains two tracks, 2) each jet contains four tracks, or 3) one jet contains two tracks while the other contains four tracks) times each of the three Z decay channels considered, resulting in nine categories. The resulting joint probability density for the event counts is then used to construct confidence intervals using a generalized version of the Feldman-Cousins technique [66], which incorporates systematic uncertainties in a frequentist way [67] [68].

Results are shown, for the 95% confidence level, as a function of m_h (for $m_a =$

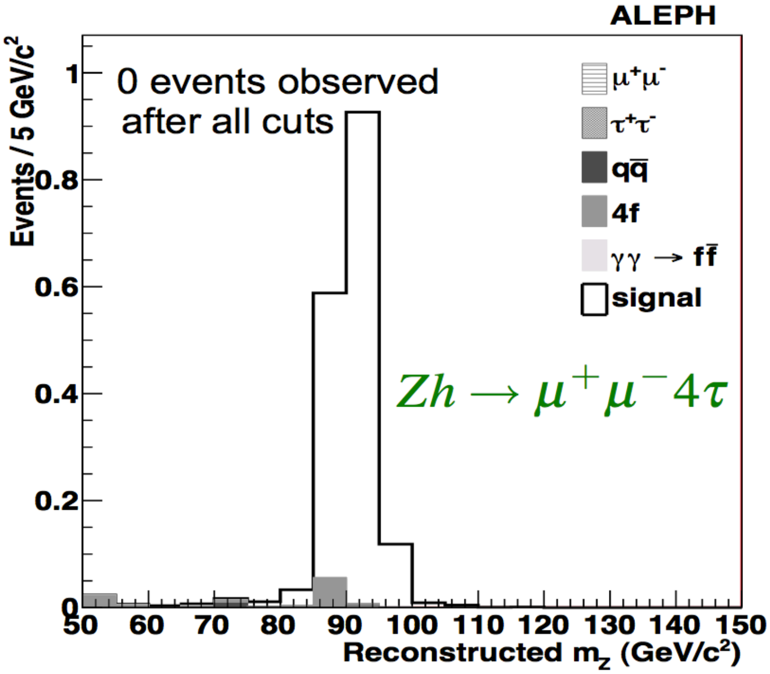

Figure 3.7: Distribution of reconstructed m_Z for the Z $\rightarrow \mu^+\mu^-$ channel.

10 GeV/c^2) on the left in Fig. 3.9. Note that the selection criteria do not depend on m_h or m_a, and thus our upper limits are fully correlated. The observed number of events is consistent with a downward fluctuation of the background and, as such, the limits on ξ^2 are stronger than expected.

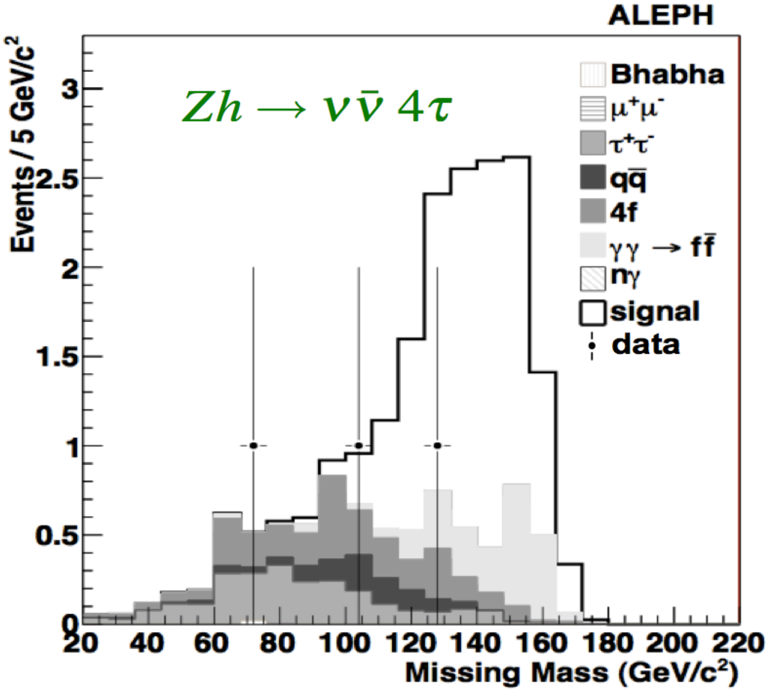

Figure 3.8: Marginal distribution for missing mass for the Z $\rightarrow \nu\bar{\nu}$ channel after all selection criteria. Two events were observed; the data point at ~ 71 GeV/c^2 is excluded after application of the missing mass cut. channel.

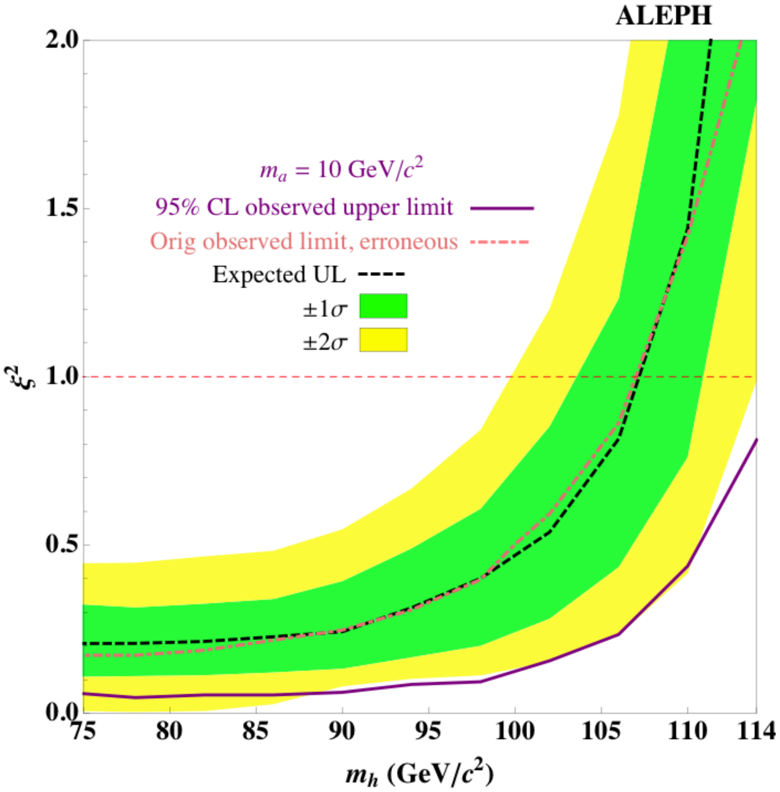

Figure 3.9: Observed and expected 95% CL limit on ξ^2 as a function of m_h for $m_a = 10$ GeV/c^2.

3.7 Conclusions

A search has been performed for a neutral scalar (h) decaying into four taus via Higgsstrahlung at LEP2, for the process $h \to 2a \to 4\tau$ and Z $\to e^+e^-$, $\mu^+\mu^-$, or $\nu\bar{\nu}$, using ALEPH data. No excess above background was observed, and for $m_h < 114$ GeV/c^2 and $m_a < 10$ GeV/c^2, $\xi^2 > 1$ can be excluded at the 95% CL, where $\xi^2 = \frac{\sigma(e^+e^- \to Z+h)}{\sigma_{SM}(e^+e^- \to Z+h)} \times (h \to aa) \times (a \to \tau^+\tau^-)^2$. This analysis covers a region of parameter space previously unexplored and further constrains models that feature light pseudoscalar Higgs particles and non-standard Higgs decays, such as the NMSSM.

Conclusions

The phenomenal success of the Standard Model (SM) and the experimental particle physics program over the course of the last several generations have come at a cost: The SM is extremely well established, but the experimental searches for new phenomena at the LHC, which might offer explanations for some of the problems unaddressed by the SM, have resulted in very strong limits on the parameters and production of these phenomena. This prompts a reevaluation of the directions and priorities of the particle physics community, and in particular motivates searching for new physics in as many experimental venues and energy realms as possible. Three searches related to this have been presented here: First, a search for events with at least three photons in the final state in proton-proton collisions with the ATLAS detector, at the LHC, sensitive to extensions of the SM Higgs sector that include new pseudoscalar a particles; second, a search for a new, low mass vector gauge boson, referred to as an A', in electron-nucleus fixed target collisions with the APEX experiment, at Jefferson Lab; and, third, a search for neutral scalar bosons decaying into four tau leptons via intermediate pseudoscalar a particles, with archival data collected by the ALEPH detector, at LEP. These searches encompass a wide variety of energy ranges and collider luminosities — from electron beam energies of $1 < E_{beam} < 6$ GeV at Jefferson Lab, to electron-positron collision center-of-mass energies of $\sim$200 GeV at LEP, to TeV-scale proton-proton collisions at the LHC – and novel methods by which to use existing data, consistent with the conclusions that new physics may be hiding in a large number of places, and that it is necessary for the physics community to perform searches in as many realms as possible.

Bibliography

[1] S. L. Glashow, *Partial Symmetries of Weak Interactions*, Nucl. Phys. **22** (1961) 579–588.

[2] S. Weinberg, *A Model of Leptons*, Phys. Rev. Lett. **19** (1967) 1264–1266.

[3] A. Salam, *in Elementary Particle Theory.* Almqvist and Wiksell, Stockholm, 1968.

[4] ATLAS Collaboration Collaboration, G. Aad et al., *Observation of a new particle in the search for the Standard Model Higgs boson with the ATLAS detector at the LHC*, Phys.Lett. **B716** (2012) 1–29, `arXiv:1207.7214 [hep-ex]`.

[5] CMS Collaboration Collaboration, S. Chatrchyan et al., *Observation of a new boson at a mass of 125 GeV with the CMS experiment at the LHC*, Phys.Lett. **B716** (2012) 30–61, `arXiv:1207.7235 [hep-ex]`.

[6] F. Englert and R. Brout, *Broken Symmetry and the Mass of Gauge Vector Mesons*, Phys.Rev.Lett. **13** (1964) 321–323.

[7] P. W. Higgs, *Broken symmetries, massless particles and gauge fields*, Phys.Lett. **12** (1964) 132–133.

[8] P. W. Higgs, *Broken Symmetries and the Masses of Gauge Bosons*, Phys.Rev.Lett. **13** (1964) 508–509.

[9] G. Guralnik, C. Hagen, and T. Kibble, *Global Conservation Laws and Massless Particles*, Phys.Rev.Lett. **13** (1964) 585–587.

[10] P. W. Higgs, *Spontaneous Symmetry Breakdown without Massless Bosons*, Phys.Rev. **145** (1966) 1156–1163.

[11] T. Kibble, *Symmetry breaking in nonAbelian gauge theories*, Phys.Rev. **155** (1967) 1554–1561.

[12] B. A. Dobrescu, G. L. Landsberg, and K. T. Matchev, *Higgs boson decays to CP odd scalars at the Tevatron and beyond*, Phys.Rev. **D63** (2001) 075003, `arXiv:hep-ph/0005308 [hep-ph]`.

[13] A. Pilaftsis and C. E. Wagner, *Higgs bosons in the minimal supersymmetric standard model with explicit CP violation*, Nucl.Phys. **B553** (1999) 3–42, `arXiv:hep-ph/9902371 [hep-ph]`.

[14] M. S. Carena, J. R. Ellis, A. Pilaftsis, and C. Wagner, *CP violating MSSM Higgs bosons in the light of LEP-2*, Phys.Lett. **B495** (2000) 155–163, `arXiv:hep-ph/0009212 [hep-ph]`.

[15] M. S. Carena, J. R. Ellis, S. Mrenna, A. Pilaftsis, and C. Wagner, *Collider probes of the MSSM Higgs sector with explicit CP violation*, Nucl.Phys. **B659** (2003) 145–178, `arXiv:hep-ph/0211467 [hep-ph]`.

[16] F. Larios, G. Tavares-Velasco, and C. Yuan, *Update on a very light CP odd scalar in the two Higgs doublet model*, Phys.Rev. **D66** (2002) 075006, `arXiv:hep-ph/0205204 [hep-ph]`.

[17] B. Holdom, *Two U(1)'s and Epsilon Charge Shifts*, Phys.Lett. **B166** (1986) 196.

[18] P. Galison and A. Manohar, *TWO Z's OR NOT TWO Z's?*, Phys.Lett. **B136** (1984) 279.

[19] M. J. Strassler and K. M. Zurek, *Echoes of a hidden valley at hadron colliders*, Phys.Lett. **B651** (2007) 374–379, `arXiv:hep-ph/0604261 [hep-ph]`.

[20] J. D. Bjorken, R. Essig, P. Schuster, and N. Toro, *New Fixed-Target Experiments to Search for Dark Gauge Forces*, Phys.Rev. **D80** (2009) 075018, `arXiv:0906.0580 [hep-ph]`.

[21] S. Chang, P. J. Fox, and N. Weiner, *Visible Cascade Higgs Decays to Four Photons at Hadron Colliders*, Phys.Rev.Lett. **98** (2007) 111802, `arXiv:hep-ph/0608310 [hep-ph]`.

[22] N. Toro and I. Yavin, *Multiphotons and photon jets from new heavy vector bosons*, Phys.Rev. **D86** (2012) 055005, `arXiv:1202.6377 [hep-ph]`.

[23] J. M. Cline, *130 GeV dark matter and the Fermi gamma-ray line*, Phys.Rev. **D86** (2012) 015016, `arXiv:1205.2688 [hep-ph]`.

[24] E. N. Glover and A. Morgan, *Z boson decay into photons*, Z.Phys. **C60** (1993) 175–180.

[25] L3 Collaboration Collaboration, M. Acciarri et al., *Search for anomalous Z* $\rightarrow \gamma\gamma\gamma$ *events at LEP*, Phys.Lett. **B345** (1995) 609–616.

[26] ATLAS Collaboration Collaboration, G. Aad et al., *The ATLAS Experiment at the CERN Large Hadron Collider*, JINST **3** (2008) S08003.

[27] *Expected photon performance in the ATLAS experiment*, Tech. Rep. ATL-PHYS-PUB-2011-007, CERN, Geneva, Apr, 2011.

[28] GEANT4 Collaboration, S. Agostinelli et al., *GEANT4: A Simulation toolkit*, Nucl.Instrum.Meth. **A506** (2003) 250–303.

[29] J. Alwall, M. Herquet, F. Maltoni, O. Mattelaer, and T. Stelzer, *MadGraph 5 : Going Beyond*, JHEP **1106** (2011) 128, `arXiv:1106.0522 [hep-ph]`.

[30] T. Sjostrand, S. Mrenna, and P. Z. Skands, *A Brief Introduction to PYTHIA 8.1*, Comput.Phys.Commun. **178** (2008) 852–867, `arXiv:0710.3820 [hep-ph]`.

[31] S. Alioli, P. Nason, C. Oleari, and E. Re, *NLO Higgs boson production via gluon fusion matched with shower in POWHEG*, JHEP **0904** (2009) 002, `arXiv:0812.0578 [hep-ph]`.

[32] T. Gleisberg, S. Hoeche, F. Krauss, M. Schonherr, S. Schumann, et al., *Event generation with SHERPA 1.1*, JHEP **0902** (2009) 007, `arXiv:0811.4622 [hep-ph]`.

[33] M. L. Mangano, M. Moretti, F. Piccinini, R. Pittau, and A. D. Polosa, *ALPGEN, a generator for hard multiparton processes in hadronic collisions*, JHEP **0307** (2003) 001, `arXiv:hep-ph/0206293 [hep-ph]`.

[34] G. Corcella, I. Knowles, G. Marchesini, S. Moretti, K. Odagiri, et al., *HERWIG 6: An Event generator for hadron emission reactions with interfering gluons (including supersymmetric processes)*, JHEP **0101** (2001) 010, `arXiv:hep-ph/0011363 [hep-ph]`.

[35] G. Corcella, I. Knowles, G. Marchesini, S. Moretti, K. Odagiri, et al., *HERWIG 6.5 release note*, `arXiv:hep-ph/0210213 [hep-ph]`.

[36] A. Alloul, N. D. Christensen, C. Degrande, C. Duhr, and B. Fuks, *FeynRules 2.0 - A complete toolbox for tree-level phenomenology*, `arXiv:1310.1921 [hep-ph]`.

[37] C. Degrande, C. Duhr, B. Fuks, D. Grellscheid, O. Mattelaer, et al., *UFO - The Universal FeynRules Output*, Comput.Phys.Commun. **183** (2012) 1201–1214, `arXiv:1108.2040 [hep-ph]`.

[38] J. Pumplin, D. Stump, J. Huston, H. Lai, P. M. Nadolsky, et al., *New generation of parton distributions with uncertainties from global QCD analysis*, JHEP **0207** (2002) 012, `arXiv:hep-ph/0201195 [hep-ph]`.

[39] H.-L. Lai, M. Guzzi, J. Huston, Z. Li, P. M. Nadolsky, J. Pumplin, and C.-P. Yuan, *New parton distributions for collider physics*, Phys. Rev. D **82** (2010) 074024. http://link.aps.org/doi/10.1103/PhysRevD.82.074024.

[40] ATLAS Collaboration, *Measurements of the photon identification efficiency with the ATLAS detector using 4.9 fb*$^{-1}$ *of pp collision data collected in 2011*, ATLAS-CONF-2012-123.

[41] M. Jimenez and K. Tackmann, *Photon identification efficiency extrapolated from electrons in $Z \to e^+e^-$ decays*, Tech. Rep. ATL-COM-PHYS-2012-241, CERN, Geneva, Mar, 2012.

[42] L. Carminati, M. Delmastro, M. Hance, M. Jimenez Belenguer, R. Ishmukhametov, Z. Liang, G. Marchiori, V. Perez Reale, D. Malinsky, M. Tripiana, and G. Unal, *Reconstruction and Identification Efficiency of Inclusive Isolated Photons*, Tech. Rep. ATL-PHYS-INT-2011-014, CERN, Geneva, Mar, 2011.

[43] ATLAS Collaboration, Aad, Georges and others, *Measurement of the isolated di-photon cross-section in pp collisions at $\sqrt{s} = 7$ TeV with the ATLAS detector*, Phys.Rev. **D85** (2012) 012003, `arXiv:1107.0581 [hep-ex]`.

[44] H. Abreu, M. Aurousseau, B. Brelier, Q. Buat, F. Bucci, L. Carminati, O. Davignon, R. Daya, S. De Cecco, M. Delmastro, J. De Vivie, M. Dova, M. Escalier, M. Fanti, M. Fayard, M. Hance, R. Ishmukhametov, M. Jimenez Belenguer, M. Kado, M. Kataoka, T. Koffas, I. Koletsou, M. Kuna, R. Lafaye, S. Laplace, G. Marchiori, K. Peters, F. Polci, L. Roos, J. Schaarschmidt, M. Stockton, H. Torres, M. Tripiana, R. Turra, G. Unal, H. Williams, and L. Yuan, *Measurement of isolated di-photon cross section in pp collision at $s = 7$ TeV with the ATLAS detector*, Tech. Rep. ATL-COM-PHYS-2011-301, CERN, Geneva, Mar, 2011. This is the supporting note for the 2010 SM diphoton cross section paper, approved by ATLAS and submitted for publication.

[45] https://twiki.cern.ch/twiki/bin/viewauth/AtlasProtected/Egamma2012Analyses.

[46] T. HSG1 Group, *Selection for H to gammagamma analysis supporting note, for Moriond 2013*, Tech. Rep. ATL-COM-PHYS-2013-093, CERN, Geneva, Jan, 2013.

[47] T. Luminosity Group, *Preliminary Luminosity Determination in pp Collisions at sqrt(s) = 8 TeV using the ATLAS Detector in 2012*, Tech. Rep. ATL-COM-LUM-2012-013, CERN, Geneva, Nov, 2012.

[48] G. Cowan, K. Cranmer, E. Gross, and O. Vitells, *Asymptotic formulae for likelihood-based tests of new physics*, Eur.Phys.J. **C71** (2011) 1554, `arXiv:1007.1727 [physics.data-an]`.

[49] M. Stohr and J. Horejsi, *Effective lagrangians for the Z boson decay into photons*, Phys.Rev. **D49** (1994) 3775–3778.

[50] A. Gutierrez-Rodriguez, C. Honorato, J. Montano, and M. Prez, *Limits on the quartic couplings* $Z\gamma\gamma\gamma$ *and* $ZZ\gamma\gamma$ *from* e^+e^- *colliders*, `arXiv:1304.7410 [hep-ph]`.

[51] APEX Collaboration Collaboration, S. Abrahamyan et al., *Search for a New Gauge Boson in Electron-Nucleus Fixed-Target Scattering by the APEX Experiment*, Phys.Rev.Lett. **107** (2011) 191804, `arXiv:1108.2750 [hep-ex]`.

[52] R. Essig, P. Schuster, and N. Toro, *Probing Dark Forces and Light Hidden Sectors at Low-Energy e+e- Colliders*, Phys.Rev. **D80** (2009) 015003, `arXiv:0903.3941 [hep-ph]`.

[53] P. Fayet, *Effects of the Spin 1 Partner of the Goldstino (Gravitino) on Neutral Current Phenomenology*, Phys.Lett. **B95** (1980) 285.

[54] P. Fayet, *A la recherche d'un nouveau boson de spin un*, Nuclear Physics B **187** no. 1, (1981) 184 – 204. http://www.sciencedirect.com/science/article/pii/055032138190122X.

[55] R. Essig, P. Schuster, N. Toro, and B. Wojtsekhowski, *An Electron Fixed Target Experiment to Search for a New Vector Boson A' Decaying to e+e-*, JHEP **1102** (2011) 009, `arXiv:1001.2557 [hep-ph]`.

[56] R. Essig, J. A. Jaros, W. Wester, P. H. Adrian, S. Andreas, et al., *Dark Sectors and New, Light, Weakly-Coupled Particles*, `arXiv:1311.0029 [hep-ph]`.

[57] M. Endo, K. Hamaguchi, and G. Mishima, *Constraints on Hidden Photon Models from Electron g-2 and Hydrogen Spectroscopy*, Phys.Rev. **D86** (2012) 095029, `arXiv:1209.2558 [hep-ph]`.

[58] G. Cowan, K. Cranmer, E. Gross, and O. Vitells, *Power-Constrained Limits*, `arXiv:1105.3166 [physics]`.

[59] APEX Collaboration Collaboration, S. Abrahamyan et al., *Data from Figure 3 from: Search for a New Gauge Boson in Electron-Nucleus Fixed-Target Scattering by the APEX Experiment*, Phys.Rev.Lett.**107** 191804.

[60] LEP Working Group for Higgs boson searches, ALEPH Collaboration, DELPHI Collaboration, L3 Collaboration, OPAL Collaboration Collaboration, R. Barate et al., *Search for the standard model Higgs boson at LEP*, Phys.Lett. **B565** (2003) 61–75, `arXiv:hep-ex/0306033 [hep-ex]`.

[61] R. Dermisek and J. F. Gunion, *Escaping the large fine tuning and little hierarchy problems in the next to minimal supersymmetric model and h to aa*

decays, Phys.Rev.Lett. **95** (2005) 041801, `arXiv:hep-ph/0502105 [hep-ph]`.

[62] ALEPH Collaboration, DELPHI Collaboration, L3 Collaboration, OPAL Collaboration, LEP Working Group for Higgs Boson Searches Collaboration, S. Schael et al., *Search for neutral MSSM Higgs bosons at LEP*, Eur.Phys.J. **C47** (2006) 547–587, `arXiv:hep-ex/0602042 [hep-ex]`.

[63] ALEPH Collaboration Collaboration, S. Schael et al., *Search for neutral Higgs bosons decaying into four taus at LEP2*, JHEP **1005** (2010) 049, `arXiv:1003.0705 [hep-ex]`.

[64] ALEPH Collaboration Collaboration, D. Decamp et al., *ALEPH: A detector for electron-positron annnihilations at LEP*, Nucl.Instrum.Meth. **A294** (1990) 121–178.

[65] ALEPH Collaboration Collaboration, D. Buskulic et al., *Performance of the ALEPH detector at LEP*, Nucl.Instrum.Meth. **A360** (1995) 481–506.

[66] G. J. Feldman and R. D. Cousins, *Unified approach to the classical statistical analysis of small signals*, Phys. Rev. D **57** (1998) 3873–3889. http://link.aps.org/doi/10.1103/PhysRevD.57.3873.

[67] C.-S. CHUANG and T. L. LAI, *Resampling methods for confidence intervals in group sequential trials*, Biometrika **85** no. 2, (1998) 317–332, `http://biomet.oxfordjournals.org/content/85/2/317.full.pdf+html`. http://biomet.oxfordjournals.org/content/85/2/317.abstract.

[68] K. Cranmer, *Statistical challenges for searches for new physics at the LHC*, `arXiv:physics/0511028`.